A scanning tunneling microscope for multi-probe experiments on the atomic scale

Dissertation

zur Erlangung des Doktorgrades

an der Fakultät für Mathematik, Informatik und Naturwissenschaften

im Fachbereich Physik

der Universität Hamburg

vorgelegt von

Jonas Matthias Jeremias Koch

Hamburg, 2024

Gutachter/innen der Dissertation:	Prof. Dr. Philip J. W. Moll Prof. Dr. Roland Wiesendanger
Zusammensetzung der Prüfungskommission:	PD Dr. Guido Meier Prof. Dr. Philip J. W. Moll Prof. Dr. Michael A. Rübhausen Prof. Dr. Michael Potthoff Prof. Dr. Roland Wiesendanger
Vorsitzender der Prüfungskommission:	Prof. Dr. Michael Potthoff
Datum der Disputation:	16.07.2024
Vorsitzender des Fach-Promotionsausschusses Physik:	Prof. Dr. Markus Drescher
Leiter des Fachbereichs Physik:	Prof. Dr. Wolfgang J. Parak
Dekan der Fakultät MIN:	Prof. Dr.-Ing. Norbert Ritter

Contents

1 Introduction **7**

1.1 Scanning tunnelling microscopy 10

1.2 Conventional STM design 14

2 The UHV chamber system **17**

3 The Multi-Probe STM setup **21**

3.1 The tunnelling probes 22

3.1.1 Tip geometry 22

3.1.2 Shielding and RF transmission 25

3.2 Scanning units 27

3.2.1 The centre tube scanner 27

3.2.2 The side tube scanners 29

3.3 Coarse Motion 35

3.3.1 Vertical coarse drive 36

3.3.2 Lateral coarse drive 37

3.4 The sample stage 42

3.5 Optical tip to tip approach 43

3.6 Cable management 48

3.7 Installation into the UHV chamber 52

4 MP-STM performance **57**

4.1 Calibration 58

4.2 Simultaneous operation 62

4.3 Overlapping scan area 63

5 Ultra-sharp single crystalline chromium tunnelling tips **67**
5.1 Electrochemical etching of ultra-sharp tunnelling tips 69
5.2 Spin-resolved imaging with an ultra-sharp single-crystalline Cr tip 72

6 Lateral current application **76**
6.1 Lateral current experiments 77
6.1.1 $NbSe_2$ 77
6.1.2 Ir(111) 84
6.2 Numerical simulations on 2-tip transport experiments 88
6.2.1 Current density distribution 90
6.2.2 The Hall effect 99
6.2.3 Joule heating 102

Conclusion and Outlook **110**

Reference List **115**

Danksagung / Acknowledgments **123**

Eidesstattliche Versicherung / Declaration on oath **124**

Abstract

Ongoing efforts to identify suitable non-volatile and energy-efficient alternatives to conventional principles in information technology for future data processing and storage are driving scientific research in the field of scanning tunnelling microscopy. In order to gain insight into dynamic processes and transport properties of promising candidates for novel technologies, such as the skyrmion racetrack and spin logic devices, advanced instruments capable of time-resolved methods and the deployment of multiple scanning probes in a nanometre scale range are sought after.

In this work, a home-built three-tip scanning tunnelling microscope designed to meet both requirements is presented. It is developed for the operation within an ultra-high vacuum chamber system, at temperatures ranging from 1.5 K to 100 K, and in an external magnetic field of up to 3 T. Three independent scanning units are capable of spin-polarised tunnelling with atomic spatial and picosecond time resolution. The ultra-sharp tunnelling tips can be brought into overlapping scan ranges, facilitating one of the microscope's potential applications: the localised generation of high-density surface currents at low total currents. This capability minimises detrimental effects such as Joule heating.

First proof-of-concept experiments involving a local surface current, along with respective numerical modelling of the electrical current on the sample surface, are shown. Additionally, a newly developed etching method for producing single-crystalline ultra-sharp chromium tips for spin-polarised scanning tunnelling microscopy in a three-tip configuration is introduced. Test measurements with a chromium tip prepared by this method are also presented.

Zusammenfassung

Fortlaufende Bemühungen nichtflüchtige und energieeffiziente Alternativen zu konventionellen Prinzipien der Informationstechnologie für zukünftige Speicherung und Verarbeitung von Daten treiben die Forschung im Bereich der Rastertunnelmikroskopie an. Für die Schaffung neuer Erkenntnisse in Bezug auf dynamische Prozesse und Transporteigenschaften von vielversprechenden Kandidaten für solche technologischen Alternativen, wie zum Beispiel dem Skyrmion-Racetrack-Memory und Spin-Logik-Bauelementen, ist ein Bedarf an fortschrittlichen Instrumenten entstanden, die zeitaufgelöste Messmethoden und den Einsatz von mehreren Rastersonden in einem Bereich in der Größenordnung von Nanometern ermöglichen.
In dieser Arbeit wird ein Rastertunnelmikroskop mit drei Spitzen präsentiert, das entwickelt wurde, um diesen Anforderungen gerecht zu werden. Es ist für den Betrieb in einem Ultra-Hochvakuum-Kammersystem, bei Temperaturen von 1,5 K bis 100 K und in einem externen Magnetfeld von bis zu 3 T konzipiert. Drei unabhängige Rastereinheiten ermöglichen das spinpolarisiertes Tunneln mit räumlicher Auflösung im atomaren Maßstab und zeitlicher Auflösung in der Größenordnung von Pikosekunden. Die ultrascharfen Tunnelspitzen können in überlappende Rasterbereiche gebracht werden, was die lokale Erzeugung von Oberflächenströmen hoher Stromdichte bei geringen Gesamtströmen ermöglicht. Diese Fähigkeit minimiert schädliche Effekte wie Joule-Erwärmung.
Es werden erste Experimente als Machbarkeitsnachweis der Erzeugung von lokalen Oberflächenströmen, zusammen mit entsprechender numerischer Modellierung des elektrischen Stroms auf der Probenoberfläche, gezeigt. Zusätzlich wird eine neu entwickelte Ätzmethode zur Herstellung einkristalliner ultrascharfer Chromspitzen für die spinpolarisierte Rastertunnelmikroskopie in Dreispitzen-Konfiguration vorgestellt. Testmessungen mit einer nach dieser Methode hergestellten Chromspitze werden ebenfalls präsentiert.

Chapter 1

Introduction

Our society is currently navigating an era of globalisation and increased interconnectedness. The exponential growth of globally transmitted information has led to an ever-increasing demand for data storage and processing at ever-decreasing spatial and temporal scales. While magnetic data storage devices, such as hard disc drives and complementary metal-oxide semiconductors (CMOS), have played pivotal roles in information technology development, they are anticipated to approach their performance limits. The challenges lie in further downsizing and enhancing computing power and energy efficiency, as the development of devices based on conventional principles is nearing a critical size beyond which information stored and processed becomes unstable. For instance, information stored in the magnetization of nano-scale ferromagnetic particles can be lost when the individual magnetic moments are interacting with their surroundings.

Scientists in the field of scanning probe microscopy, among many other scientific fields, are directing their efforts towards finding non-volatile alternatives for computation and memory devices that show more stable and more energy-efficient behaviour. For this purpose, the scanning tunnelling microscope (STM) has proven to be a powerful tool. Its spatial and energy resolution enables the study of atomic-scale structures and patterns on metallic surfaces, which is important for understanding thin film systems and exotic electronic states developing at metallic interfaces. Spin-polarised STM and scanning tunnelling spectroscopy allow for the study of the electronic and magnetic properties of such structures.

This technique is, however, limited in temporal resolution due to the use of a trans-impedance amplifier with bandwidths in the kHz range. Most processes on the atomic-scale are occurring on time scales that are too fast to be measurable with such a bandwidth. To increase

temporal resolution, measurement methods such as pump-probe spectroscopy and electron spin resonance (ESR) based on high-frequency voltage pulses have been adapted for STM applications. These adaptations require special cabling, which is optimised for the transmission of high-frequency (HF) voltage pulses, and waveform generators.

Furthermore, the use of a single tunnelling probe in conventional STM is limiting certain applications. The simultaneous contacting of structures by four probes and subsequent transport measurements on a microscopic scale are not feasible with a conventional STM setup. With multiple probes, transport measurements with high current density can be performed. The conductance of nano-scale structures can be electrically characterized and even manipulated locally.

In this thesis, a home-built multi-probe STM (MP-STM) will be presented that combines the high-frequency applications previously used in the RF-SP-STM with the deployment of three separately operating and separately moveable scanning probes. The probes can be approached in each other's close proximity, which enables the local application of high current densities with variable current direction. The microscope is designed for deployment in ultra-high vacuum (UHV), at low temperatures ranging from 1.5 K to 100 K, and in the presence of an external magnetic field of up to 3 T flux density.

The deployment of the MP-STM is opening new perspectives for exciting experiments. High-density current-induced transport measurements in nano-scale magnetic and non-magnetic structures become feasible. Furthermore, dynamic processes induced by surface currents can be investigated by time-resolved methods. An exciting application would be the study of atomic-scale magnetic skyrmions, which are stabilised by Dzyaloshinskii-Moriya interactions in magnetic thin film systems grown by epitaxial growth on Ir(111) substrates [1, 2, 3, 4, 5, 6]. Unravelling the properties of skyrmion motion would be an important step towards the realisation of a skyrmion racetrack device, based on the proposal of Stuart Parkin [7, 8], or skyrmion-based spintronic devices, which would provide an alternative to conventional information technology. To this end, two of the three tunnelling probes can be used as source and drain for lateral currents to study the mobility of skyrmions and their interaction with in-plane currents.
Current-driven motion of skyrmions of the size of about 100 nm in Pt/Co/Ta stacks was reported previously by Woo *et al.* [9]. They found a necessary critical current density on the order of $10^{11}\,\frac{\mathrm{A}}{\mathrm{m}^2}$, which has been confirmed for other thin film systems in more recent studies [10, 11]. For atomic-scale skyrmions a critical current density of $10^{10}\,\frac{\mathrm{A}}{\mathrm{m}^2}$ was theor-

etically predicted [12]. This is considerably smaller in comparison to the current density of $3 \cdot 10^{12} \frac{\mathrm{A}}{\mathrm{m}^2}$ needed for inducing the motion of domain walls, which was initially proposed as principle for the racetrack memory [7]. With two tunnelling probes in close proximity to each other, used as source and drain for a lateral current, the application of such high current densities without harming side effects like Joule heating becomes feasible. In combination with time-resolved measurement methods, the skyrmion mobility can not only be studied in real-space but also in the time domain. The latter becomes especially relevant when considering that a speed of more than 100 $\frac{m}{s}$ was observed for skyrmions of the size of 100 nm [9].

First, the UHV chamber system and cryostat for the MP-STM will be presented in chapter 2. Subsequently, the design of the MP-STM and a method of optically approaching the tunnelling tips to each other will be presented in chapter 3. Starting from the geometry of the tunnelling tips, the design considerations necessary to fulfil the microscope's ambitious requirements will be described in detail.
The functionality of the MP-STM was tested by performance measurements which will be discussed in chapter 4. These include the calibration of the three scanning units on highly oriented pyrolytic graphite (HOPG) and Au(111), the simultaneous multi-tip measurements, and the scanning with overlapping scan ranges on HOPG.
In chapter 5, the development of an etching method for ultra-sharp single-crystalline chromium tunnelling tips will be described, and test measurements will be discussed. The chromium tips produced this way are used for SP-STM. For testing the tip's functionality, spin spirals were observed on Fe bilayers on Ir(111).
Finally, in chapter 6, the feasibility of locally applying lateral currents with high current densities will be discussed. To this end, the application of lateral currents by two tunnelling tips as contact electrodes was simulated with the software COMSOL Multiphysics®, which utilises the finite element method (FEM), and compared with lateral current experiments were done. Three individual simulations will be shown. The first is focused on the relation of the applied current density of the lateral current with geometric parameters of the configuration of contact tips and sample. The second is focused on the interaction of the lateral current with an out-of-plane external magnetic field, and the third is focused on the effects of Joule heating caused by lateral currents. The experiments were done on $NbSe_2$ and Ir(111). The results, including the effects of lateral currents on both of these substrates, will be discussed in section 6.1.

In the following sections, the fundamental principles of scanning tunnelling microscopy and the conventional design of scanning tunnelling microscopes will be briefly introduced. This aims to provide the reader with a basic understanding of the methods upon which the design of the MP-STM is founded.

1.1 Scanning tunnelling microscopy

In scanning tunnelling microscopy, a tip is approached at a close distance from a metallic sample. At distances of a few Ångströms, electrons can cross the gap between the two conductors due to their wave-like properties. This is called electron tunnelling. It can be described by the time-independent Schrödinger equation with $\Psi(z)$, the location-dependent one-dimensional wave function of the electron, E, the electron's energy, $V(z)$, the location-dependent potential barrier, $\hbar$, the Planck's constant, and m, the electron mass:

$$(V(z) - \frac{\hbar}{2m}\frac{d^2}{dz^2})\psi(z) = E\psi(z) \tag{1.1}$$

The square of the absolute value of the wave function $|\psi(z)|^2$ is describing the probability of the presence of the electron. Thus, a finite value of $\psi(z)$ at the position z indicates a finite probability of the electron being at z. The comparison between the reflection of an electron on a potential barrier in classical mechanics and the tunnelling of an electron through a potential barrier with a height of V_0 is shown in figure 1.1:

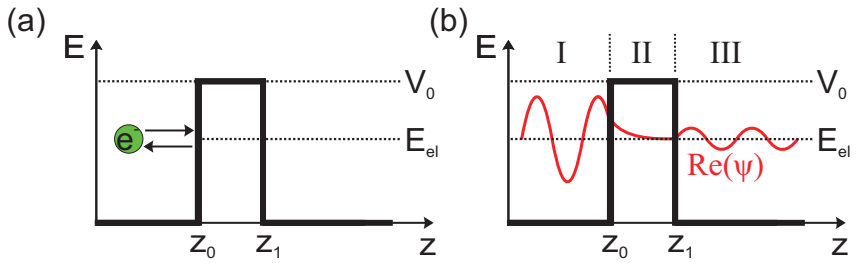

Figure 1.1: One-dimensional energy to distance diagrams, showing in **(a)** the reflection of an electron (indicated in green) with the energy $E_{el} < V_0$ on a potential barrier of height V_0, and showing in **(b)** the tunnelling of an electron with the same energy and wave-like properties through the potential barrier due to the tunnel effect. The black lines indicate the potential with a barrier between z_0 and z_1. The diagram **(b)** can be split into three regions I, II, and III. The red line indicates the real part of the electron's wave function and illustrates its behaviour in the three regions.

The electron wave can be described in the three regions as follows:
For the regions I and III ψ_1 and ψ_3 are determined:

$$\begin{aligned} -\frac{\hbar^2}{2m}\frac{d^2\psi_1}{dz^2} &= E_{\mathrm{el}}\psi_1 \\ \psi_1 &= Ae^{ikz} + Be^{-ikz}, \\ -\frac{\hbar^2}{2m}\frac{d^2\psi_3}{dz^2} &= E_{\mathrm{el}}\psi_3 \\ \psi_3 &= Ce^{ikz}, \\ \text{with: } k &= \sqrt{\frac{2mE_{\mathrm{el}}}{\hbar^2}}. \end{aligned} \tag{1.2}$$

A and C are the coefficients of the wave function in regions I and III in positive z-direction, and B being the coefficient of the reflected part of the wave function in region I in negative z-direction. For region II ψ_2 is determined:

$$\begin{aligned} -\frac{\hbar^2}{2m}\frac{d^2\psi_2}{dz^2} + V_0\psi_2 &= E_{\mathrm{el}}\psi_2 \\ \psi_2 &= Fe^{ik'z} + Ge^{-ik'z}, \\ \text{with: } k' &= \sqrt{\frac{2m(E_{\mathrm{el}} - V_0)}{\hbar^2}}. \end{aligned} \tag{1.3}$$

F and G are the coefficients of the wave function in region II in positive and negative z-direction.
Here, k' is complex since $E_{\mathrm{el}} < V_0$ in region II, resulting in an exponential decay, with $\kappa = ik'$ and $\kappa^2 = \frac{2m(V_0 - E_{\mathrm{el}})}{\hbar^2}$. The exponential decay of the wave function leads to a lower amplitude for ψ_3 in region III and in consequence a lower $|\psi(z)|^2$, which relates to a lower probability of presence in region III. The wave function's coefficients can be determined by the continuous differentiability at x_0 and x_1, and the probability of tunnelling can be determined by the transmission coefficient $T = |\frac{A}{C}|^2$:

$$T \approx \frac{16k^2\kappa^2}{(k^2 + \kappa^2)^2} \cdot e^{-2\kappa(z_1 - z_0)} \tag{1.4}$$

It is exponentially dependent on the width of the potential barrier $z_1 - z_0$ and κ, the latter being dependent on $\sqrt{V_0 - E_{\mathrm{el}}}$.
In a theoretical approach, J. Tersoff and D. R. Hamann investigated electron tunnelling in an STM configuration based on the first-order time-dependent perturbation theory by J. Bardeen [13, 14]. They approximated a spherical tunnelling tip and s-type tip electron wave

functions at low temperatures T and a low bias voltage U between the tip and sample. Figure 1.2(a) shows a sketch of this geometry.
The tunnelling current I can be described as:

$$\begin{aligned} I &\propto U \cdot \rho_{\mathrm{t}}(E_{\mathrm{F}}) \cdot \rho_{\mathrm{s}}(E_{\mathrm{F}}, \vec{r}_0) \cdot e^{2kR}, \\ \text{with: } \rho_{\mathrm{s}}(\vec{r}_0, E_{\mathrm{F}}) &= \sum_{\nu} |\psi_\nu(\vec{r}_0)|^2 \cdot \delta(E_\nu - E_{\mathrm{F}}) \\ \text{and: } \kappa_{\mathrm{TH}} &= \frac{\sqrt{2m\phi_{\mathrm{eff}}}}{\hbar}. \end{aligned} \tag{1.5}$$

Where ρ_{s} is the density of electron states in the sample, ρ_{t} is the density of electron states in the tip, E_{F} is the Fermi energy, $\vec{r}_0$ is the centre of the spherical tip, and R is the tip's radius. The density of states in the sample, ρ_{s}, is the sum over the sample's wave functions of discrete electronic states E_ν. The decay constant κ_{TH} (the index 'TH' indicating the Tersoff-Hamann model) can be compared to the decay constant κ of ψ_2 in the model of one-dimensional electron tunnelling since ϕ_{eff} is related to the energy difference of the tunnelling electrons and vacuum potential barrier in the STM configuration, which is in the model of one-dimensional electron tunnelling given by $V_0 - E_{\mathrm{el}}$. In approximation ϕ_{eff} is equal to the average surface work functions of tip and sample ϕ_{t} and ϕ_{s}.
The wave functions decay exponentially into the vacuum. This results in an exponential dependency of the tunnelling current on the distance d between the tip and sample:

$$I \propto e^{-2kd} \tag{1.6}$$

Within a more generalised model for finite bias voltages, the tunnelling current can be described by a convolution of the respective local density of states (LDOS) of tip and sample in a weighted integral over the range of energies [15]:

$$I \propto \int_0^{eU_{\mathrm{bias}}} \rho_{\mathrm{t}}(E, eU_{\mathrm{bias}}) \cdot \rho_{\mathrm{s}}(E) \cdot T(E, eU_{\mathrm{bias}}, d)\, dE, \tag{1.7}$$

with e, the elemental charge, and the transmission factor:

$$T(E, eU_{\mathrm{bias}}) = exp[-d \cdot \sqrt{\frac{4m}{\hbar^2}(\phi_{\mathrm{t}} + \phi_{\mathrm{t}} + eU_{\mathrm{bias}} - 2E)}]. \tag{1.8}$$

In particular, electrons can tunnel from occupied states of one metal into unoccupied states of the other metal. If the energy of the tunnelling electrons is conserved, as indicated in figure 1.2(b), we are dealing with elastic electron tunnelling. The effective vacuum barrier is the average of the surface work functions of tip and sample, ϕ_{t} and ϕ_{s}. When applying

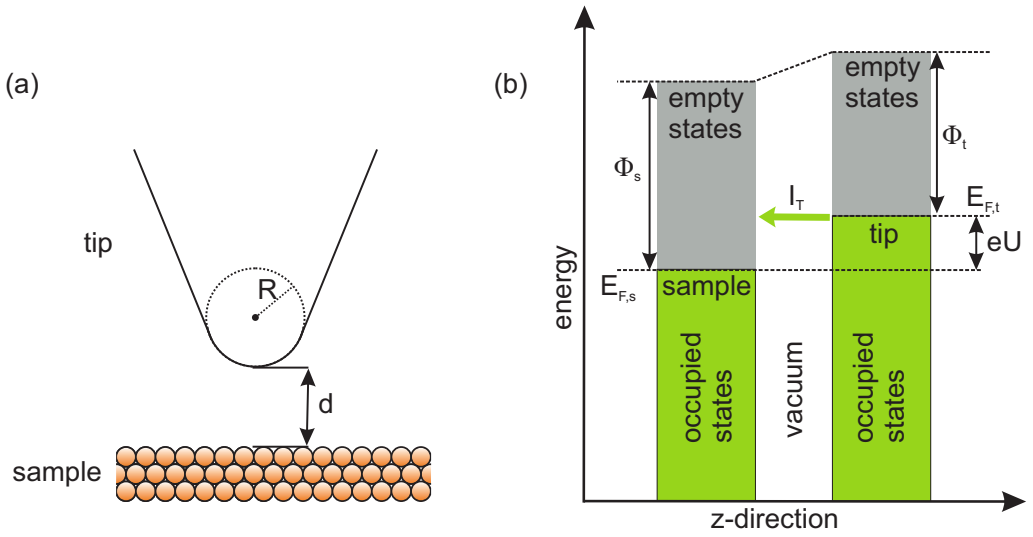

Figure 1.2: **(a):** Sketch of the model for tunnelling between a tip of radius R and a sample at a distance of d as introduced by J. Tersoff and D. R. Hamann. **(b):** Illustration of the electronic states of the tip and sample in close proximity with a bias voltage U_{bias} applied. The occupied electronic states of the tip and sample are indicated in green, which reach up to the material's Fermi energies $E_{\mathrm{F,s}}$ and $E_{\mathrm{F,t}}$. The unoccupied states are indicated in grey. ϕ_{s} and ϕ_{t} are the surface work functions of each material. The Fermi level of the STM tip is shifted by eU_{bias} due to the applied bias voltage. The tunnelling of the electrons from occupied states at the Fermi level in the tip into unoccupied states of the sample is resulting in the tunnelling current I_{T} as indicated by the green arrow.

U_{bias} to the tip, the Fermi level $\mathrm{E_F}$ is shifted by $\mathrm{e \cdot U_{bias}}$, so that electrons from the occupied states of the tip can tunnel into unoccupied states of the sample. Thus, a voltage-dependent tunnelling current is measurable.

By utilising a magnetic STM tip, the tunnel magneto-resistance (TMR) is affecting the tunnelling current [16]. The electronic states of the tip are split by their spin direction into a majority band with spins being parallel to the tip's magnetization and a minority band with spins being anti-parallel to the tip's magnetization. The tip is spin-polarised. This way, the tunnelling current becomes dependent on the spin-polarisation of the sample's unoccupied states, which are dependent on the local magnetization. In the approximation of small U_{bias}, the spin-polarised tunnelling current I_{sp} can be described by [17]:

$$I_{\mathrm{sp}} = I_0(1 + P_1 \cdot P_2 \cdot cos(\angle(\vec{m}_1, \vec{m}_2)) \tag{1.9}$$

where I_0 is the spin-averaged current, and $P_i = \frac{\Omega_{i,\uparrow} - \Omega_{i,\downarrow}}{\Omega_{i,\uparrow} + \Omega_{i,\downarrow}}$ is the spin polarisation of sample and tip, respectively ($\Omega_{i,\uparrow}$ and $\Omega_{i,\downarrow}$ denote the spin up and spin down density of states in electrode i). This so-called spin-polarised STM (SP-STM) was first demonstrated in 1990 by Wiesendanger *et al.* [18].

1.2 Conventional STM design

Due to the exponential dependency of the tunnelling current on the tip-to-sample distance, mainly the few atoms of the tip closest to the sample are contributing to the total tunnelling current. This way, by scanning the tip over a sample, a map with atomic-scale precision can be measured. The motion of the tip is controlled by a piezoelectric tube scanner, which can be deformed by the inverse piezoelectric effect.

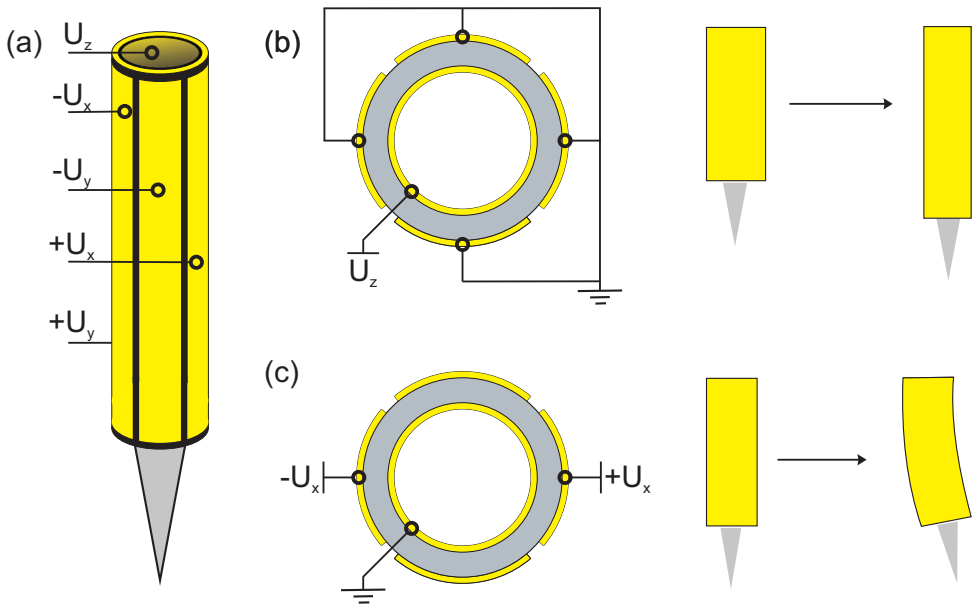

Figure 1.3: Sketch of the tube scanner. **(a):** Electrical contacts of the five electrodes illustrated in yellow, which are used to induce lateral and vertical motion. **(b):** Top view of the tube scanner's electrodes during a vertical displacement. The outer electrodes are connected to a common ground, while a voltage U_z is applied to the z-electrode. **(c):** Top view of the tube scanner's electrodes during a lateral displacement in x-direction. Voltages $-U_x$ and $+U_x$ are applied to the x-electrodes, while the z-electrode is on ground. To the right of the images **(b)** and **(c)** sketches show an exaggerated resulting deformation of the tube scanner.

The piezoelectric effect is the change of electrical polarisation and the creation of a net voltage by mechanically deforming specific types of solid materials like lead zirconate titanate (PZT). The inverse piezoelectric effect is the deformation of such piezoelectric materials by applying an electric field. This deformation can be used to induce a precise motion in a component made of piezoelectric material. In STM applications, tubes made of piezoelectric materials are used to scan the STM tip over the sample with atomic-scale precision.
The so-called tube scanner comprises four segmented electrodes on the outside and one electrode on the inside. Figure 1.3 shows sketches of a tube scanner with its electrodes. By applying voltage to the inside electrode and putting the outer electrodes on ground, the tube

can be deformed vertically in z-direction (figure 1.3(b)). This inner electrode is therefore the so-called z-electrode. A lateral motion of the tip can be induced by applying voltages of opposite signs to opposing outer electrodes while the inner electrode is on ground. This expands one side of the tube while it contracts the other, resulting in the tube bending (figure 1.3(c)). An STM tip attached to the tube's end face will thereby move laterally. Voltages of up to 200 V are used to induce a considerable displacement by the tube scanner in a μm range.

The absolute distance of motion the tube is inducing on a STM tip is not known since the tip's absolute position cannot be measured. Therefore, tube scanners are calibrated by imaging structures of known dimensions.

During an STM experiment, an electronic feedback unit provides a constant tip-to-sample distance. Here, a constant tunnelling current is maintained by applying voltages between the inner and outer electrodes of the tube scanner, thereby controlling the scanner's vertical displacement. The principle of this design is illustrated in figure 1.4.

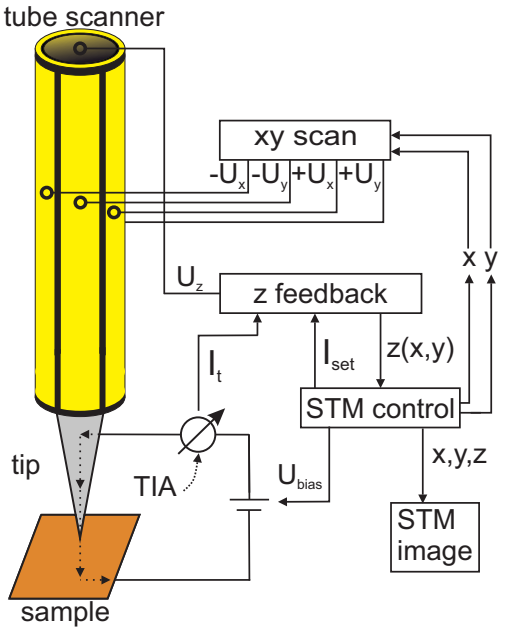

Figure 1.4: Flow chart of a conventional STM operating in constant current mode. The STM control unit is commanding the xy scan unit to apply the appropriate voltages ($\pm U_x$,$\pm U_y$) to the tube scanner to realise the tip's lateral motion. The STM control also sets the bias voltage U_{bias}, which is applied between tip and sample, and a set value for the tunnelling current I_{set}. The current tunnelling from the sample to the tip I_{t} is measured by the trans-impedance amplifier (TIA). If $I_{\mathrm{t}} \neq I_{\mathrm{set}}$, the z feedback unit applies the appropriate voltage U_{z} to stabilise the tip-to-sample distance. With this, U_{z} is adjusted for $I_{\mathrm{t}} = I_{\mathrm{set}}$ and $z(x, y)$ is reconstructed from this adjustment, creating a topographic map.

The bias voltage U_{bias} between tip and sample as well as the tunnelling current setpoint are set in the STM control electronics. The tunnelling current between tip and sample I_t is measured using a trans-impedance amplifier (TIA). This signal is compared by the feedback unit to I_{set}. If the tip-to-sample distance is changing, so is the tunnelling current. A control voltage U_z drives the tube scanner's vertical displacement and adjusts the tip-to-sample distance for $I_t = I_{set}$. While the tip is scanning over the sample, U_z is converted into the vertical displacement of the scanner and is used to reconstruct a map $z(x, y)$ that represents the topography of the sample, named as constant-current STM image.
Alternatively, the STM tip can be set at a constant height, and the change in the tunnelling current can be recorded while the tip is scanning over a surface. This way, no feedback unit is needed which results in a quicker acquisition of data. The resulting tunnel current $I(x, y)$ is then converted into the topographic image by appropriate post-processing. However, since the tip-to-sample distance is not controlled, the risk of tip-sample collisions is increased in this mode of STM operation.
Due to the high sensitivity of I_t to changes in the sample-to-tip distance, STM has a high spatial resolution. As the tunnelling current is exponentially dependent on the tip-to-sample distance, a variation by 1 Å in distance typically results in a variation of I_t by a factor of ten. Likewise, minimal mechanical vibrations between the tip and sample can lead to considerable noise. Furthermore, since I_t is typically set to $\leq 1\,\mathrm{nA}$ and is amplified by up to nine orders of magnitude by the TIA, minimal interfering electrical signals in the tunnelling current can lead to significant noise. To counter and avoid these noise sources, great effort is directed at decoupling STMs from mechanical and electrical disturbance.

Chapter 2

The UHV chamber system

The MP-STM was developed for experimental applications in UHV, at ultra-low temperatures and in the presence of an external magnetic field. To meet the requirements for the experimental setup, an ultra-high vacuum (UHV) system was constructed. In this chapter, the chamber system will be described, which was designed and built by J. Friedlein and J. Harm *et al.* [1, 19, 20]. In figure 2.1, a schematic is shown. To decouple the system from mechanical vibration, it is built on a table made of aluminium profiles, which rests on passive pneumatic damping legs with a resonance frequency of 1 Hz. The profiles are filled with sand to dampen acoustic modes.

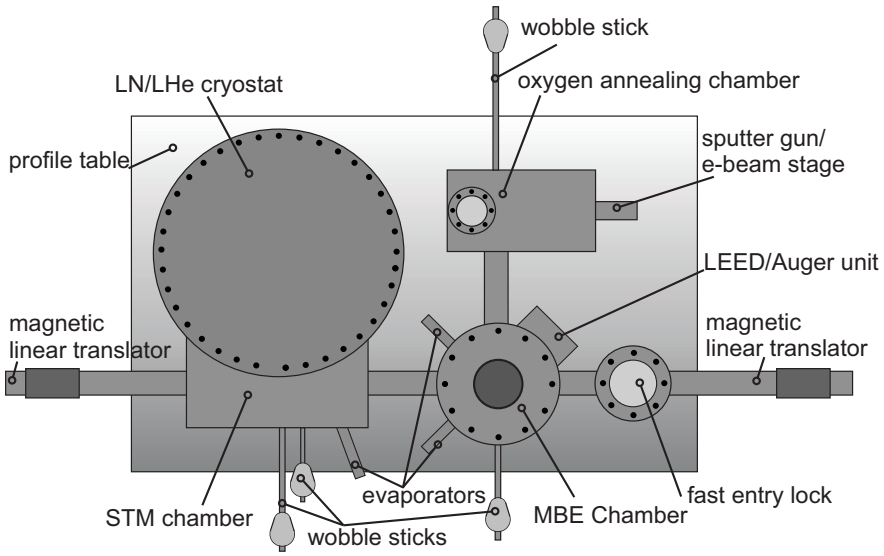

Figure 2.1: A schematic representation of the top view of the UHV chamber system housing the MP-STM. The image is adapted with permission from [21].

The chamber system comprises three separable UHV chambers and a fast entry lock. The latter was designed to facilitate the quick insertion of new samples or scanning probes. It is connected to the molecular beam epitaxy (MBE) chamber. With a magnetic linear translator and a wobble stick, a freshly introduced sample can be transferred from the fast entry lock into the preparation chamber. There, contamination on samples can be removed, and the sample's surface can be annealed. Contaminants are removed by sputtering the sample with Ar^+ ions utilising a sputter gun while heating it by a resistance heating stage. Afterwards, the samples are annealed by utilising an electron beam stage, which can be done in UHV or in an oxygen atmosphere.
For growing metallic thin films, the samples can be transferred subsequently to the MBE chamber again, where the films are grown by evaporating a particle flux onto the freshly prepared substrate surface. The evaporation rate can be calibrated using a quartz crystal micro-balance, which measures the amount of deposited material on samples, and a combined low-energy-electron-diffraction (LEED)/Auger unit for surface analysis.
After surface preparation, the samples are transferred by a magnetic linear translator into the STM chamber. It is the largest chamber and the heart of the entire UHV chamber system, designed for achieving minimum temperatures of 1.5 K and a strong magnetic field with magnetic flux densities of up to ± 3 T in the z-direction ($\pm 0.5\%$ homogeneity deviation in 1 cm^3) at the centre of the MP-STM.
The STM chamber comprises a helium- and a nitrogen-bath cryostat, which are shielded by three thermal shields. In figure 2.2, a sectional side view of the chamber is illustrated. In the centre of the helium bath, the MP-STM is mounted inside a tube. Around the tube inside the helium bath, a superconducting split-pair magnet is installed, enclosing the microscope. The magnet is imposing a geometric limitation on the MP-STM due to its structure, limiting the tube's diameter to 70 mm. Below the MP-STM, and strongly thermally coupled to it, is the coldest point of the setup. There, a small vessel is connected via valves to the helium bath and a vacuum pump outside of the chamber. By opening the valve to the bath, the vessel can be filled with liquid helium, and by opening the valve to the vacuum pump, the pressure in the vessel can be reduced. By reducing the vessel's pressure with the pump, the helium boiling point is reduced, which causes the vessel to be cooled down below the 4.2 K boiling point of helium at ambient pressure. The lowest recorded temperature reached in the vessel is 1.05 K; hence, it is called 1 K-pot. Utilising the 1 K-pot, temperatures as low as 1.5 K at the microscope can be reached in equilibrium. With a 5 W electrical heater installed inside the 1 K-pot, a stable and safe operation in the presence of the maximum magnetic field at temperatures up to about 100 K can be reached [21]. In principle, even higher temperatures are accessible, but this has not been tried before because the microscope

is weakly thermally coupled to the helium bath by cabling and the frame of the 1 K-pot, and can radiate heat to its surroundings. Therefore, it transmits small amounts of heat to the bath cryostat, which houses the superconducting magnet. If the magnet's temperature is increased above the helium boiling point, gaseous bubbles may hinder efficient local cooling on the superconductor. This can result in a temperature increase above the transition temperature of niobium, leading to quenching. Therefore, increasing the temperature of the microscope must be done cautiously to prevent damage to the UHV chamber system and secure the safety of the operating personnel.

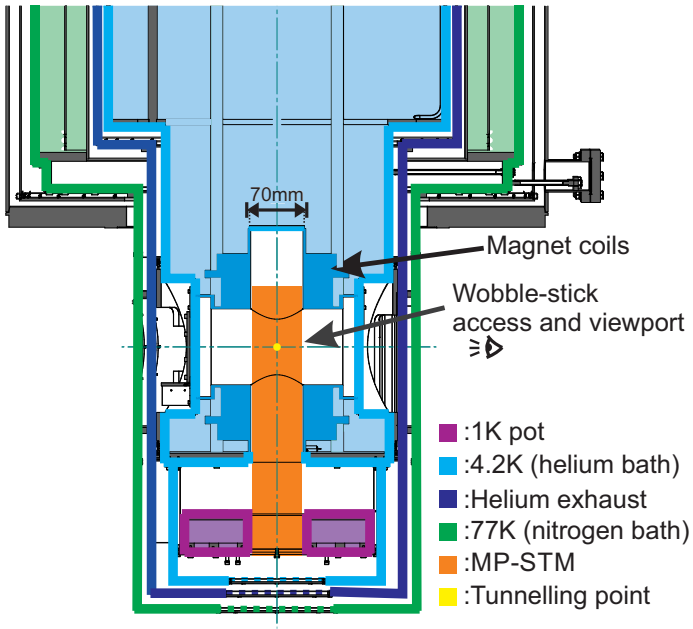

Figure 2.2: Sectional side view of the bath cryostat installed in the STM chamber. In the central tube, the position of the STM inside the cryostat and the centre point are outlined. The STM is mounted onto the 1 K-pot right below, marked in purple. Surrounding the STM tube is the 4.2 K shield connected to a liquid helium bath, marked in light blue, and the helium exhaust gas shield, marked in dark blue. The outermost shielding is the 77 K shield that is connected to the liquid nitrogen bath, marked in green. The STM is visually accessible and reachable with a wobble stick through rotatable doors of the thermal shielding on the STM chamber's front, which is to the right in this cross section.

The 1 K-pot is surrounded by the 4.2 K thermal shielding, which shields the 1 K-pot from thermal radiation of the surrounding environment. The 4.2 K thermal shielding is connected to the liquid helium reservoir of the cryostat and is cooled by it to the boiling point of liquid helium at 4.2 K [22].

The 4.2 K thermal shield is surrounded by an exhaust gas shield, which is connected to and cooled by the exhaust gas line of the helium bath, reaching temperatures of 40 to 50 K. Surrounding the exhaust gas shield is the outermost thermal shield, forming a boundary to

the UHV chamber walls at room temperature. This outermost shield is the 77.4 K thermal shield, which is cooled by a liquid nitrogen bath to the nitrogen boiling point of 77.4 K [22]. The nitrogen bath is surrounding the helium bath and shielding it from the chamber walls, which are at room temperature. Thus, it is prolonging the time it takes for the helium to evaporate. Therefore, the helium- and the nitrogen baths need to be refilled only about once a week, depending on the temperature the MP-STM is operated at in this configuration.
To insert a sample or a tunnelling probe into the microscope, rotatable doors of the various thermal shieldings can be opened, thereby providing access to a wobble stick mounted on the STM chamber's front, which is shown in figure 2.1. On the STM chamber's front is a large viewport giving visible access to the microscope, as indicated by the eye symbol in figure 2.2. This way, the UHV chamber system provides the means to cool down the MP-STM to temperatures below the boiling point of helium. It is not necessary to remove the microscope from the cryostat to insert samples, as is done in other cryostat systems. The microscope can be heated up to at least 100 K while maintaining an external magnetic field.

Chapter 3

The Multi-Probe STM setup

With its ability for high-frequency applications and its compatibility with magnetic fields and low temperatures, the MP-STM presented in the following is a novelty in multi-probe scanning tunnelling microscopy. It extends the possibilities of traditional scanning probe microscopy by introducing the simultaneous application of three separately functioning scanning units to investigate atomic structures in close proximity to each other. This opens opportunities for various exciting transport and manipulation experiments of exotic electronic and magnetic structures, but also requires a complex design that overcomes the many challenges that are accompanied by this endeavour. These start with the geometric requirements for the tunnelling tips to be in their ultimate proximity at a distance in the nanometre range. Another requirement is the transmission of high-frequency signals to the junctions while preventing their interference with each other to investigate dynamic properties with high temporal resolution. Each of the tunnelling probes must be positionable above a sample's surface with a precise microscopic motion that grants spatial resolution in the picometre range to image structures on the atomic scale. Also, a macroscopic motion is necessary in order to allow the exchange of samples and tunnelling probes *in situ*, and at a safe distance to each other, while also allowing to position all three tips in close proximity to each other again afterwards. To remove the probes from each other, the scanning units must be moveable not only in vertical direction, which is sufficient in the traditional STM setup, but also in lateral directions, requiring at least two units to be macroscopically moveable in three dimensions. Thus, a considerable number of electrical components and electrical connections are required.
Since experiments utilising the MP-STM are to be conducted in an ultra-high vacuum (UHV) environment, at cryogenic temperatures, and in the presence of a strong magnetic field in z-direction, stringent prerequisites for the microscope's design are demanded. Operation at cryogenic temperatures ensures thermal stability and gives access to electric and magnetic

phenomena, but at the same time, a considerable thermal stress is exerted on the microscope's components as they are contracting with different thermal expansion coefficients. Furthermore, all the components have to be UHV compatible and non-magnetic, which limits the choice of usable materials. Finally, the split-pair/Helmholtz magnet is limiting the space inside the UHV chamber; therefore, the MP-STM has to fit into a cylindrical volume with a diameter of 70 mm.
In the following, the design solutions for the imposed prerequisites will be presented, starting with the microscope's centre and zooming out to the surrounding components. Thus, the tip geometry, the tip receptacles, and their RF transmission lines will be described first before paying attention to the scanner units' fine and coarse motion devices and ending with the sample stage and the cabling of the microscope's electrical components.

3.1 The tunnelling probes

3.1.1 Tip geometry

Since the MP-STM is used for the investigation of structures on the atomic scale, the three tunnelling tips need to be approached towards each other at distances that are similar to the surface structures of interest. When inducing lateral currents or manipulating the structures with voltage pulses, the tips must be as close as possible, as the applicable lateral current density depends on the minimal distance between them. Also, the current should be applied as directly as possible to the structure of interest, for example, a thin film system, to prevent parasitic effects in areas with different electronic structure. Furthermore, the tips must be at a sufficient distance in order to prevent electron tunnelling between them.
The most basic prerequisite for the tunnelling tips to be in microscopic proximity to each other is their shape. In figure 3.1 a sketch of the microscopic tip apices in close proximity is shown. For the apex form, a half-sphere with radius r was assumed. The tunnelling junction of each tip is at the lowest point of the sphere, which is indicated in figure 3.1 as red dotted line. Therefore, the minimal distance D is larger than $2r$, since the tips are in contact at smaller distances. The angle α is the angle between neighbouring tips, and ϕ is the opening angle of each tip. The angles are determining where the tips are closest to each other. If α is too small or ϕ is too big, the tips are getting in contact with each other at a position higher up on the tips' shafts. When α is at 45°, the opening angle of each tip can be as large as about 45° before they can get into contact. This is why the determining geometric parameters for the tip-to-tip distance are the angles α and ϕ as well as the apex radius r of each tip.

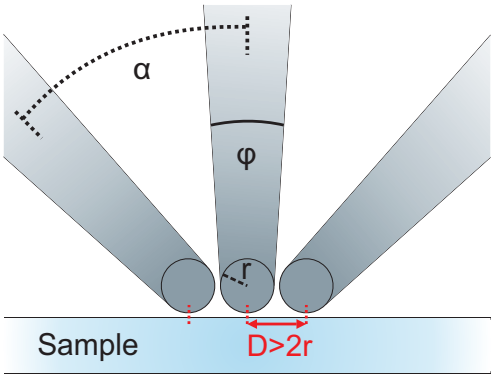

Figure 3.1: Sketch of three tips in microscopic proximity to each other while each is in tunnelling contact to the sample. Here, it was assumed that the tip apices are spherical with radius r. Thus, the tunnelling junction is at the sphere's lowest point (red dotted line), with the distance D between the tunnelling junctions. The angle α between the tips and the opening angle ϕ of each tip are determining the position of the closest distance between neighbouring tips. Thus, α, ϕ, and r are the limiting parameters to the distance D.

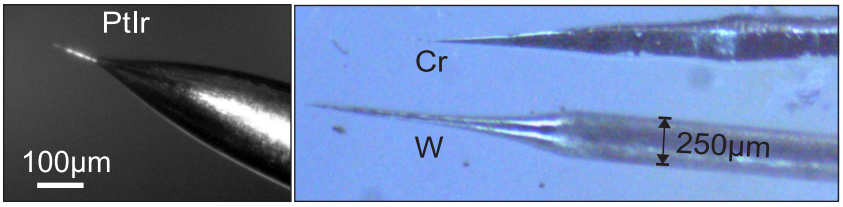

Figure 3.2: Images of the ultra-sharp STM tips taken with an optical microscope. The tip in the left image is a purchased PtIr tip from NaugaNeedles LLC, and in the right image, two home-made tips of tungsten (W) and chromium (Cr) are shown. The microscopic tips' radii are smaller than the microscope's optical resolution. Due to their small opening angle, they are broadening slowly to the tip shaft's diameter, which is 250 μm for the W tip.

So-called ultra-sharp tips feature apex radii r of 10 nm - 30 nm and opening angles ϕ of 10 ° - 25 °. They fulfil the geometric requirements to be positioned at nano-scale distances from each other and are therefore utilised for the MP-STM. The ultra-sharp tips can either be purchased by companies such as NaugaNeedles LLC or produced by a home-built setup for electrochemical etching [23, 24]. For the MP-STM experiments, purchased ultra-sharp tips made of tungsten or an alloy of platinum and iridium (PtIr tips), as well as home-made ultra-sharp tungsten or single crystalline chromium tips were used. For this application, the method of etching ultra-sharp chromium bulk tips with a small opening angle $\phi = (18 \pm 3)$ ° and apex radii $r = (11 \pm 5)$ nm was improved. These chromium tips allow for spin-polarised STM experiments using the tunnelling magneto-resistance (TMR) effect [25, 16]. While magnetic structures can also be imaged when using a non-magnetic tunnelling tip utilising the non-collinear magneto-resistance (NCMR) [26] or the tunnelling anisotropic magneto-resistance

(TAMR) [27], the TMR exhibits in many systems a stronger signal. It is also sensitive to collinear magnetic moments as in ferromagnetic metal layers, in contrast to the NCMR.
The method and the characterisation of a chromium bulk tip produced this way are described in chapter 5. In figure 3.2, images of ultra-sharp tips are shown, as used in the MP-STM setup. The images are taken with an optical microscope. Depicted on the left image is a purchased PtIr tip, while the right image shows two home-made tips of tungsten and chromium. The small opening angle ϕ can be perceived, but the radii of the apices are too small for the microscope's optical resolution to be visible. These tunnelling tips fulfil the geometric prerequisites to approach them in close proximity to each other. The chromium tip's sensitivity to magnetic structures was successfully tested on the double layer (DL) Fe on Ir(111) system, which features dislocation lines that pin spin spirals. This is presented and discussed in chapter 5 as well.

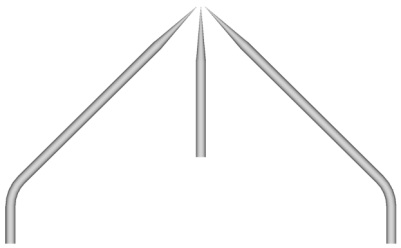

Figure 3.3: Sketch of the three tips in a macroscopic view. While the centre tip's geometry is simple, the side tips must be positioned at a 45° angle to the centre one. With the devices for fine- and coarse motion parallel to the sample, the simplest geometry is implemented by a 45° bend of the side tips. Thereby, the side tips need to be far off-centre with respect to their motion devices due to space limitations.

For the implementation of fine motion, each tunnelling tip is mounted onto a piezoelectric tube scanner. Were the tube scanners of the side tips also positioned at a 45° angle relative to the centre tip, the probe would be scanned in 45° tilted plane and not parallel to the sample's surface. Therefore, a 45° bend is introduced to the side tips' shafts. Figure 3.3 depicts the macroscopic geometry of the three tips, showing the bend in the tips. Furthermore, the tube scanners and the lateral coarse drive motors of the side tips take up space, so that the side tips cannot be positioned next to the center tip but need to be elongated laterally to reach the center tip.

3.1.2 Shielding and RF transmission

While the geometric prerequisites are fulfilled, the tips will emit electromagnetic radiation when applying RF signals to them due to their shape as elongated conducting rods, which is necessary to approach them into each other's proximity. When transmitting RF signals to the tunnelling junctions, the induced oscillations of the electrons inside the tip behave as Hertzian dipoles and are emitting the RF signals as electromagnetic waves into the surroundings with the power $P \propto \omega^4$ (ω: frequency) [28]. This leads to losses in the RF signal, resulting in a non-constant tunnel voltage amplitude and cross-talk since the other tips are picking up the signal, which is distorting the signals transmitted through them. In order to reach the centre tip, the side tips need to have a lateral length of about 15 mm. This makes them susceptible to vibrational excitation, which would lead to the coupling of mechanical vibration into the tunnelling junctions.

A good way to shield an electric conductor from cross-talk and radiation loss is to use a coaxial cable. With the outer conductor being on ground potential, a coaxial cable serves as a cylindrical wave guide. There, electromagnetic waves, which are emitted by the wire in the centre, are reflected by the outer conductor, and standing waves are created. With the grounding of the outer conductor, the electrical field is oriented radially and the magnetic field is oriented circularly around the inner conductor. The power of an RF signal propagates perpendicular to the electric and magnetic fields, following the cable's direction parallel to the Poynting vector [28] and is not radiated off. Thus, by introducing the side tip as inner conductor into a semi-rigid coaxial cable, it is electromagnetically shielded. Additionally, the outer conductor, together with the cable's dielectric, is stabilising the tip mechanically, thereby reducing the risk of vibrational excitations.

In figure 3.4, a model of the shielded tip is shown in (a), and a cross section of the cable shielding the tip is shown in (b). The cable is a semi-rigid coaxial cable made of beryllium copper (BeCu; SC-119/50-SB-B - COAX CO, LTD). To introduce the tip into the cable, first the inner conductor is removed by simply pulling it out with pincers. Then the tip's shaft, which has a diameter of 250 μm similar to the cable's inner conductor, is cautiously inserted into the cable. Subsequently, the 45° bend is done with a pincer that has round claws, and the cable is mounted onto a SMPS coaxial connector (SMPS male smooth bore ⌀ .047 SEMI-RIGID CABLE, SV Microwave Inc.). The tip's shaft is inserted into the hollow inner conductor of the connector, which consists of a tube with a pair of leaf springs at the end that pinch and hold the tip's shaft in place. The outer conductors of the cable and the connector are then glued together with conductive EJ2189-LV epoxy resin, which was manufactured by EPO-TEK® [29].

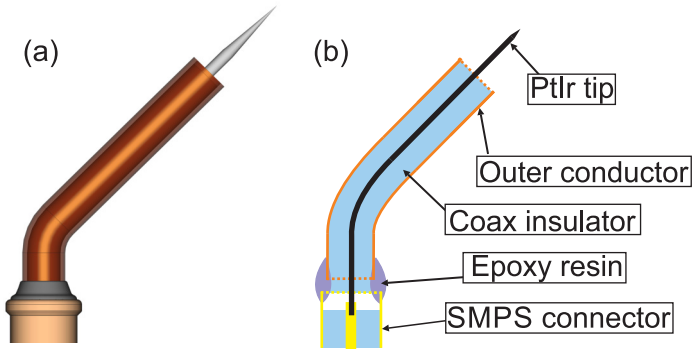

Figure 3.4: **(a)**: Model of the shielded side tip mounted on an SMPS coaxial connector. **(b)**: Cross section of the BeCu coaxial shielding, showing that the side tip is introduced into the coaxial cable, replacing the inner conductor that was removed before. The shielded tip is connected to the SMPS coaxial connector by connecting the tip to its inner conductor and glueing the outer conductor of the cable and the connector together using conductive epoxy resin.

The semi-rigid coaxial cable and the SMPS connector are both rated for the transmission of RF signals, lowering the potential RF signal loss. However, the tips cannot be shielded all the way to the tunnelling junction in order to reach the centre tip geometrically. In figure 3.5 the case of the coaxial shielding blocking the way to the centre tip is shown. The unshielded part of the tips could still radiate off the RF signal.

In the framework of his thesis, J. Friedlein did a simulation of the tip's antenna effect using the RF module of the *COMSOL Multiphysics* simulation programme [19]. According to this simulation, the antenna effect is greatly reduced if the tip length outside the coaxial shielding is not greater than one millimetre. This leads to a simulated reflected RF signal (reflection parameter S11) of about -0.4 dB at 20 GHz in comparison to -4 dB at 20 GHz for a 3 mm tip length. The signal loss is lower for shorter cable lengths outside of the shielding, but one millimetre poses a necessary compromise.

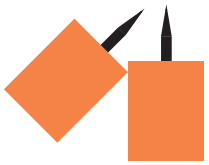

Figure 3.5: Sketch of the coaxial shielding hindering two tips from reaching each other.

Similar to the side tips, the centre tip is also mounted into an SMPS connector to maintain the RF transmission line. However, since the tip length can be limited to one millimetre without limiting the access of the side tips to microscopic proximity to the centre tip, it does not need to be introduced into a semi-rigid coaxial cable. In the MP-STM setup, the SMPS connectors are also functioning as tip sockets that can be installed by connecting them to their counterpart connectors that are installed in the microscopes. The relative positions of the tips and the way they would be implemented in the MP-STM are shown in the model in figure 3.6. There, aluminium rings can be seen that are enclosing the

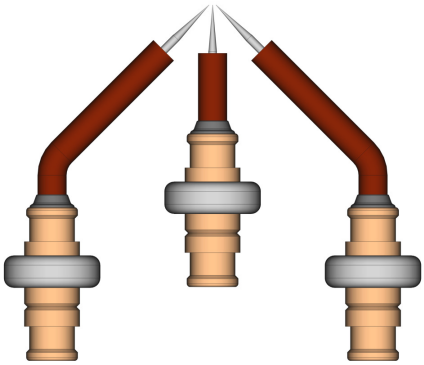

Figure 3.6: All three tips connected to their SMPS connectors which serve as tip sockets. The connectors can be mounted to the MP-STM by connecting them to their counterpart connectors installed in the microscope.

SMPS connectors. These are used to grab them with wobble-sticks used in the UHV setup mentioned in chapter 2. This way, the tips can easily be mounted *in situ* in the MP-STM and be exchanged quickly with spare tips stored in racks in the STM chamber. For readjustment of the angle α of the side tips, they can be tilted within their connectors by a small angle backlash.

3.2 Scanning units

3.2.1 The centre tube scanner

The three-dimensional fine motion of the MP-STM's scanning probes is implemented by using tubes made of modified PZT, a piezoelectric ceramic also called PIC181, which were purchased from PI ceramic GmbH [30]. Since their introduction by Binnig and Smith in 1986 [31], these so-called tube scanners are a well-established tool in scanning probe microscopy. They are hollow cylinders with four segmented electrodes coating the piezoelectric on the outside and one electrode coating it on the inside (see figure 3.7a).
In order to displace the scanner in lateral direction, for example, in $x+$, a voltage U is applied to the corresponding outer electrode, and a voltage of the opposite sign is applied to the opposite electrode (in this case, $x-$). Meanwhile, the inner electrode is connected to the electrical ground. Depending on its polarisation and the direction of the electric field, the piezoelectric is expanding perpendicular to the field. This creates a stress σ in the z direction $\sigma = Y d_{31} \frac{U}{t}$, where Y is Young's modulus, d_{31} is the piezo constant, and t is the thickness of the tube's walls [32]. The contrary stresses are creating a torque that causes the tube to bend perpendicular to its axis.

To displace the scanner vertically, a voltage U is applied to the inner electrode, the z-electrode, which causes a uniform expansion of the tube. The lateral and vertical motion can be operated simultaneously, allowing a stable and precise motion in three dimensions. As shown in figure 3.7(b), the tube scanner is installed into the MP-STM by gluing it into a ring cut out on a macor plate, which is bolted to the MP-STM's body. The tunnelling probe described in section 3.1 is mounted onto its counterpart connector, which is glued into a macor ring on top of the tube scanner. The ring is glued to the scanner's end face. For all glued connections, the epoxy resin EPO-TEK® H77 was used (manual : [33]).

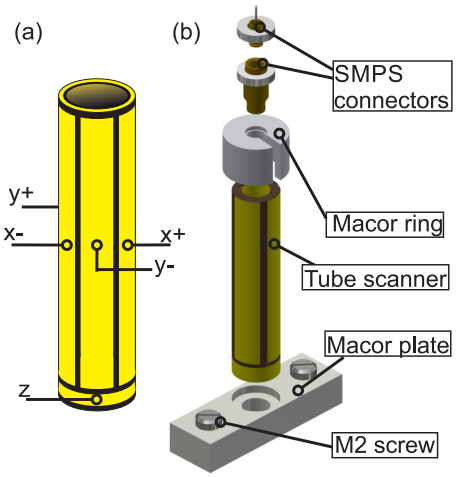

Figure 3.7: The centre tube scanner.**(a):** Sketch of a conventional tube scanner. **(b):** 3D explosion model of the centre scanning unit.

In order to match the expansion coefficients of the used components and reduce thermal stress, which may occur when cooling to a minimal temperature of 1.5 K, macor was chosen as the connecting material. According to [34], its expansion coefficient is close to that of modified lead zirconate titanate, which the tube scanners are made of (PIC181,[30]), for 192 K, 77 K, and 4.2 K. The expansion coefficients of $15(\pm 3)\cdot 10^{-6}\mathrm{K}^{-1}$ for modified lead zirconate titanate and $13(\pm 0.5)\cdot 10^{-6}\mathrm{K}^{-1}$ for macor at 4.2 K are close to the coefficients of H77 with $33\cdot 10^{-6}\mathrm{K}^{-1}$ and EJ2189 with $52\cdot 10^{-6}\mathrm{K}^{-1}$ (used in the probe's SMPS connector)[33, 29]. Additionally, to further reduce the occurrence of thermal stress, a segment was cut out of the macor ring, as seen in figure 3.7(b). This way, stress can be compensated by giving the ring more room to contract and expand. The SMPS connectors are connecting to a flexible coaxial cable made of silver-plated copper (manual:[35]) that is continuing the RF transmission line through and out of the microscope's body. It is guided by the tube scanner, exiting the scanning unit below the macor plate, where it is implemented into the body.

3.2.2 The side tube scanners

When a conventional tube scanner should be displaced laterally, say in x-direction by the amount δx, it needs to be bent, creating a tilt angle α (see 3.8(a) and (b) for simplification). Therefore, a probe tip on the tube's end face is, in addition to its lateral displacement, also displaced vertically by the amount δz due to the tube's geometry.

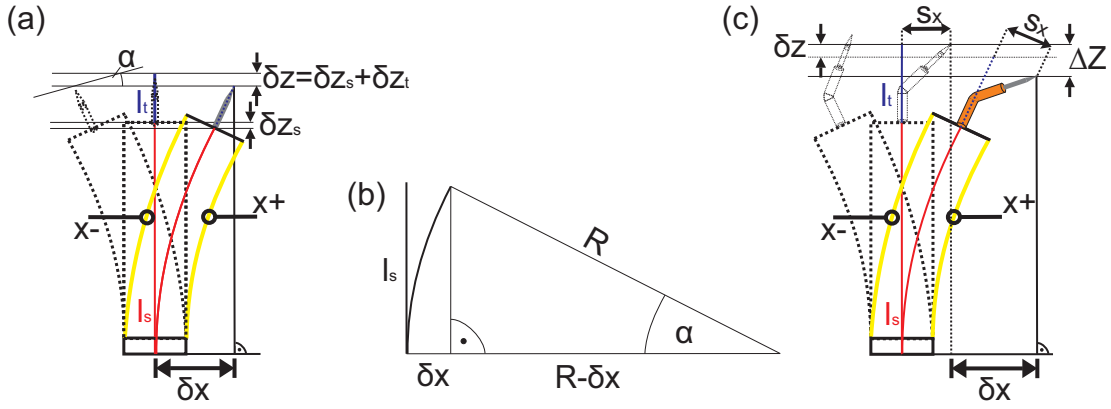

Figure 3.8: Vertical displacement due to bending. **(a)**: Sketch of a conventional tube scanner with lateral displacement δx by bending it by an angle of α. Due to the tube's geometry, an additional vertical displacement at its end face occurs (δz_s), which is amplified at the tunnelling junction by the length of the tunnelling tip l_t, resulting in $\delta z_\mathrm{s} + \delta z_\mathrm{t}$. **(b)**: Simplification of the bending tube defining α and the curvature radius R. **(c)**: Similar sketch to (a) but with a side tunnelling tip (described in 3.1) mounted on the tube scanner. The tunnelling junction is shifted by a distance s_x from the tube's centre axis. This results in a larger vertical displacement ΔZ.

Based on the findings of Chen and Locatelli et al. [32, 36], this geometric characteristic of tube scanners was discussed by Hannss et al. [37] and by C. Oldorf [38]. According to their studies, this vertical displacement can be approximated by:

$$\delta z_\mathrm{s} = \frac{16 l_\mathrm{s}^3}{3\pi^2 r^2 t^2} d_{31}^2 U_x^2, \tag{3.1}$$

where l_s is the length, r is the radius, t is the wall thickness, d_{31} is the piezo constant of the tube scanner, and U_x is the applied voltage. Thus, when the voltage U_x is applied to induce a displacement in x-direction, the tunnelling probe is de facto projecting a parabolic surface (due to $\delta z_\mathrm{s} \propto U_x^2$) with the edges of the lateral scanning range appearing bent in z-direction. This can lead to distortions in imaged structures. Furthermore, the tunnelling probe is elongating the bend cylinder, which is the tube scanner, and adding to the vertical displacement with δz_t. This geometric relation can be written as:

$$\delta z_\mathrm{t} = \delta z_\mathrm{s} \frac{6 l_\mathrm{t}}{l_\mathrm{s}}, \tag{3.2}$$

where l_t is the length from the tube's end face to the tunnelling junction at the tip apex. This behaviour is known in the scanning probe community and is small enough that it does not pose a problem for most conventional STM applications. In table *i*, the geometric parameters for the conventional tube scanner used for the centre scanning unit and the experimental parameters for a lateral displacement of $\delta x = 3\mu$m by applying U_x=147 V are listed. The parameters listed in table *i* and the following table *ii* are extracted from the manufacturer's data and calibration at room temperature. For simplicity, deviations in parameters have been ignored since they do not alter the qualitative result of the calculation. When filling the parameters of table i into the equations 3.1 and 3.2, the total vertical displacement $\delta z = \delta z_s + \delta z_t$ is calculated to be $\delta z = 0.37$ nm.

l_s	l_t	U_x	d_{31}	r	t	δz_s	δz_t
25 mm	10.5 mm	147 V	-120 $\frac{pm}{V}$	2.5 mm	1 mm	0.105 nm	0.265 nm

Table i: Parameters of the conventional centre tube scanner for a lateral displacement δx of 3 μm. d_{31} refers to the material PIC181 (modified lead zirconate titanate) [30]. The tube is vertically displaced by the sum of δz_s and δz_t.

In comparison to the corrugations of atomic lattices that are on the order of picometres, the vertical displacement seems to be large. However, it should be noted that the vertical displacement occurs at a lateral displacement of 3 μm in quadratic dependence on the applied voltage. Therefore, the effect is negligible when scanning at comparably small vertical displacement ($< 1\mu$m), which is sufficient in most applications when investigating small structures, such as atomic lattices. Even when scanning at larger lateral displacement, the occurring bending in z-direction can be corrected by calculating the vertical displacement with the equations 3.1 and 3.2 and subtracting it from the data so that the sample is projected on a flat 2D plane. Due to the design of the side scanning unit's vertical coarse drive, which is described in more detail in section 3.3, the side tube scanner's geometric dimensions deviate from the ones of the centre tube scanner, which are shown in table *ii*.

l_s	l_t	U_x	d_{31}	r	t
20 mm	15 mm	147 V	-120 $\frac{pm}{V}$	1.6 mm	0.5 mm

Table ii: Parameters of the side unit's tube scanner for calculating δz for a lateral displacement δx of 2.6μm. d_{31} refers to the material PIC181 (modified PZT) [30].

When inserted into equations 3.1 and 3.2, a vertical displacement of $\delta z = 2.9$ nm is calculated for the same applied voltage of U_x=147 V and a lateral displacement of about $\delta x = 2.6\mu$m. However, the tunnelling junction is not on the central axis of the tube scanner. Due to its distance to the centre scanner, the side tips need to be elongated towards the centre probe

by about 15 mm to be capable of reaching its close proximity. When the tunnelling junction is far away from the tube's central axis, the vertical displacement is drastically increased by a factor of $s_x \cdot \sin(\alpha)$, with s_x being the 15 mm distance of the tunnelling junction from the tube's central axis [37]. The term can be approximated by $s_x\alpha$ since the tilt of the tube and thereby the angle α are small ($\ll 1\,°$). The total vertical displacement ΔZ can be calculated by:

$$\Delta Z = s_x \cdot \alpha + \delta z. \tag{3.3}$$

Thereby, the angle α can be calculated according to C. J. Chen [32] with the tube's length and the curvature radius R of the bend by [32]:

$$\alpha = \frac{l_\mathrm{s}}{R}, \text{ with } R = \frac{\pi r t}{2\sqrt{2} d_{31} U_x}. \tag{3.4}$$

A geometric sketch can be seen in figure 3.8(c), where a conventional tube scanner in lateral displacement is shown, with one of the side tips mounted on its end face. In the picture, the vertical displacement $\delta z = \delta z_\mathrm{s} + \delta z_\mathrm{t}$ and the larger vertical displacement ΔZ from equation 3.3 are indicated.
By inserting the values of table ii and the δz calculated above into the equations 3.3 and 3.4, a total vertical displacement of $\Delta Z = 5955.6\,\mathrm{nm} + 2.6\,\mathrm{nm}$ is calculated for an applied voltage of 147 V, which corresponds to a lateral displacement of $\delta x = 2.6\,\mu\mathrm{m}$. This is exceeding the side tube's vertical scan range of ± 500 nm by far. It is limiting the lateral scan range. Therefore, precise and uninterrupted imaging over larger scan frames is not feasible with the conventional tube scanner design in combination with the side probes.
In figure 3.9(b), a 300 nm x 300 nm scan is shown that was measured with one of the side scanning units on highly oriented pyrolytic graphite (HOPG). Depending on the quality of the HOPG sample, mono-atomic terraces are typically quite large, with lateral dimensions ranging from hundreds of nm to several microns [39]. The image was measured utilizing a tube scanner in conventional fashion with geometric parameters as listed in table *ii*. The image shows a steep incline of the sample, which is indicated by the color scale to the right of the image. The incline is ranging from -47 nm to 47 nm. A similar tilt can be seen in the blue line in figure 3.9 (a), which shows an average of ten neighboured line scans in the image's centre from left to right (indicated by the blue line in (b)).

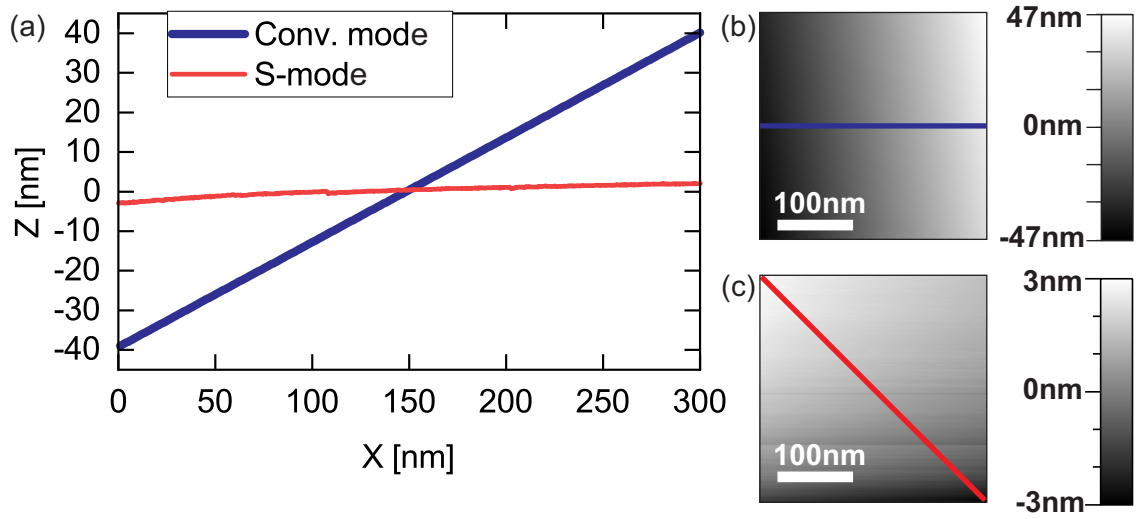

Figure 3.9: Images measured on HOPG comparing the effect of the vertical displacement on the right side unit's scanner in conventional design and in s-mode design. **(a):** Line scans of the red lines in the images (b) and (c). Blue (conventional mode) is referring to the image **(b)** measured with the scanner in conventional design. Red (S-mode) is referring to the image **(c)** measured with the scanner in the S-scanner design. Both images were measured utilising a Pt/Ir ultra-sharp tip. **(b)**: U_{bias}=30 mV, I_{T}= 6 nA, ambient conditions. **(c)**: U_{bias}=700 mV, I_{T}= 3 nA, ambient conditions.

There, the drastic effect of the side probe's vertical displacement ΔZ while scanning is observable, resulting in a 27% slope. On a surface that is expected to be atomically flat and parallel to the lateral motion of the tips, this large tilt is not explainable by a macroscopic angle between the probe and the sample but must occur due to the vertical displacement amplified by the tunnelling junction's distance to the tube scanner's central axis, as discussed above. Such a large tilt must result in strong distortions of investigated nano-scale features such as the imaged angle of mono-atomic step edges, which is mainly an artefact due to the tip's apex geometry only [37]. Furthermore, the vertical displacement needs to be constantly compensated by the tube scanner, leading to creep effects, and in larger scans, an additional compensation with z coarse steps is necessary to prevent the tip from either crashing into the sample or drifting out of tunnelling contact.

A solution to this problem was introduced by M. Hannss *et al.*[37]. They proposed to use the so-called S-scanner, a tube scanner design that bends in an S-like motion, compensating for the scanner's tilt and thereby the lateral displacement of the tunnelling probe. In this design, the outer electrodes for lateral motion are divided into two segments of equal size. The lower four electrodes are then connected according to the conventional design, and the upper electrodes are connected with the same voltages but with the opposite sign to the lower part, as shown in figure 3.10(a).

By applying the same voltage as as in the case of a conventional tube scanner, the upper half

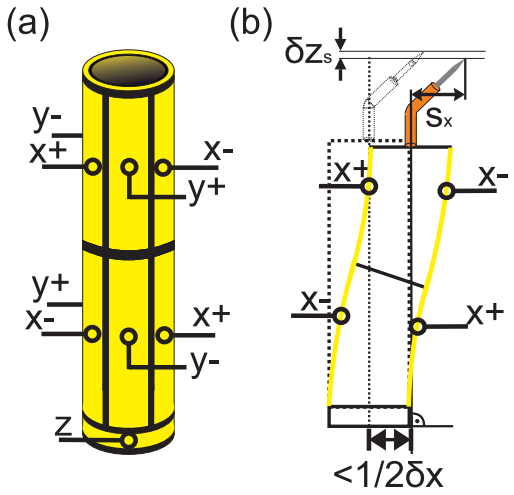

Figure 3.10: **(a)**: Sketch of the S-scanner model. **(b)**: Sketch of the S-scanner being laterally displaced. Due to the top half of the scanner bending in the opposite direction and compensating the tube's tilt, the vertical displacement is confined to the displacement δz_s. With the same voltage used as in (a) only less than half of the lateral displacement is achieved.

is compensating for the tilting angle of the lower half by bending in the opposite direction. Thus, the tube's end face and the tunnelling probe are not tilting, resulting in a tilt angle of $\alpha = 0$. Thereby, the vertical displacement in figure 3.10(b) only consists of the easily correctable δz_s of the tube scanner's bending at half of its height, where the back bending of the upper half is not correcting the tilt. This is according to equation 3.1 at 0.53 nm, when applying the voltage U_x=147 V.

Less than half of the lateral displacement δx of a conventional tube scanner driven with the same voltage is achieved, though, since the upper half is bending in the opposite direction. However, the scan range is effectively larger since δz_s can now be compensated for the whole lateral scan range on a flat surface because it does not exceed the vertical scan range.

In our setup, the polarity of the electric contacts of the S-scanner can be switched so that it can be used as a conventional tube scanner as well. Thus, the effect of the two designs on the scanner's vertical displacement during lateral motion can be compared. As described above, the conventional mode was tested on HOPG (figure 3.10(b)), as well as the S-mode (figure 3.10(c)). Figure 3.9(c) shows the HOPG surface, measured with the right tip's tube scanner in S-mode. By comparing it to the height scale on the right of the image, one finds the tilting effect to be considerably smaller.

Moreover, while the main features in the image measured in conventional mode in figure 3.9(b) are superimposed by the strong tilting, the image in (c) exhibits artefacts like tip changes, and the ad- and desorption events can be identified by the stripes visible in the image. In figure 3.9(a), a line scan is pictured that shows the largest height difference in (c), ranging from -3 nm to 3 nm (marked by the red line in (c)). This height difference does not resemble the atomically flat HOPG surface either, but is rather caused by thermal drifting of the sample relative to the right probe and a creep effect in the lower part of the image that occurred while starting the scan. Even though image (c) was not measured under ideal scanning conditions, considering the creep, thermal drift, and unstable tip, small-scale effects can be identified. This is demonstrating the obstructive effect of the larger vertical displacement occurring when operating the side tube scanners in a conventional fashion and shows the effectiveness of the S-scanner design in negating the tube's tilting.
The side scanning units are assembled similar to the centre unit, with the probes mounted on their counterpart SMPS connectors, which are glued to a macor ring and the tube scanner below that, as depicted in figure 3.11. In contrast to the previous case, the scanners are mounted on macor pedestals instead of plates, since they are implemented into the coarse approach motors described in the following section 3.3.

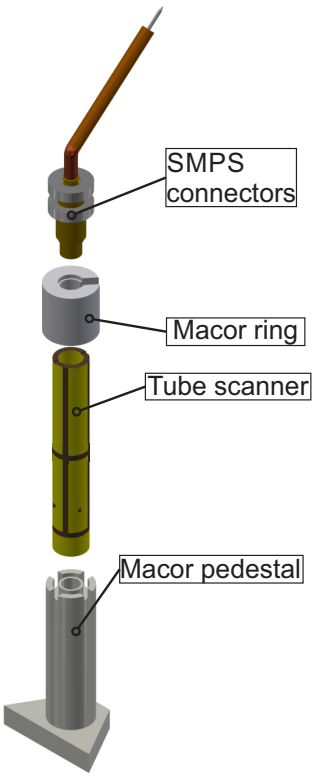

Figure 3.11: 3D explosion model of the assembly of a side scanning unit consisting of a side probe described in section 3.1 and the S-scanner mounted onto a macor pedestal.

3.3 Coarse Motion

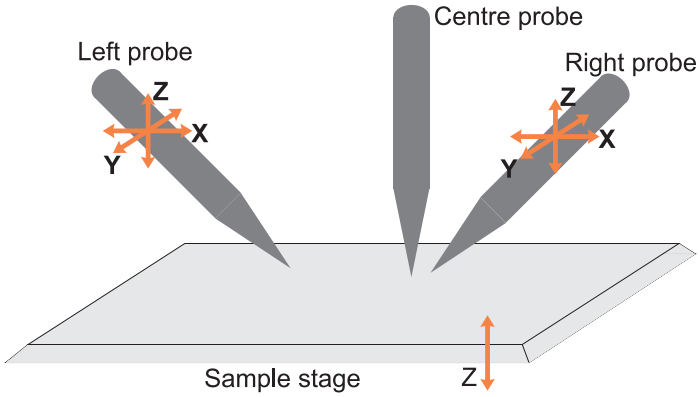

Figure 3.12: Directions of motion.

The tube scanners can induce fine motion only within a range of a few micrometres laterally and less than 500 nm in the vertical direction. However, for the exchange of samples and tunnelling probes, the probes installed in the MP-STM must be positioned at a greater distance from the sample. For exchanging the tunnelling probes, the sample stage and the side tips can be retracted each by a coarse drive motor one centimetre in z-direction from tunnelling contact. Additionally, the side scanning units can be retracted laterally by two centimetres. This way, the user can safely remove or insert a tunnelling probe from the scanning unit without the risk of crashing it into another probe or the sample. The coarse motors have to be sufficiently precise to approach the tunnelling tips stepwise to the sample surface and relative to each other when starting a new experiment, so that the tunnelling contact can be reached within the tube scanner's range. Meaning the step size of the coarse motors has to be smaller than the tube scanner's range and be reliably reproducible. As shown in the diagram in figure 3.12, the MP-STM's units have the following coarse drive motion parameters. Each of the side scanning units, consisting of the tunnelling probes (shown in dark grey) and the tube scanners, can approach the sample and be retracted from it independently in vertical direction. To reach any desired position relative to the centre probe, they can be moved laterally in a scan range of two centimetres in x- and 2.4 cm in y-direction. Furthermore, the sample stage can be moved in vertical direction to and away from the centre scanning unit with a coarse motor in z-direction.

In the following, the principle of the coarse drive mechanism and the different designs of lateral and vertical coarse drives will be introduced.

The coarse motion is realized by using slip-stick motors. These consist of so-called piezoelec-

tric (in short: piezo) stacks, or shear piezos, that are glued to the MP-STM's body using epoxy resin of the type EPO-TEK® H77 [33] and a sapphire prism that is to be moved (see figure 3.13(a)). The shear piezos act like the piezoelectric material in the tube scanners as capacitors. In this case, the ceramic PIC255, which consists of modified lead zirconium titanate [30], is used as an insulator. In contrast to PIC181 used in the tube scanners, PIC255 is not expanding perpendicular to an applied electric field but is expanding diagonally in a shear movement due to the inverse piezoelectric effect (see figure 3.13(b)). At the endings the piezo stack is covered with insulating Al_2O_3. Due to static friction, the sapphire is pushed aside while the piezo stack expands diagonally. Then, by dropping the capacitor's voltage quickly, the piezo ceramic relaxes quickly into its initial form, and the sapphire remains in its position due to its inertia, or is dragged back only a little. By applying a saw-tooth voltage, the sapphire can thereby be driven stepwise in the direction of diagonal expansion along the stack's surface, with a step size depending on the stack's expansion that is influenced by its size and the applied voltage.

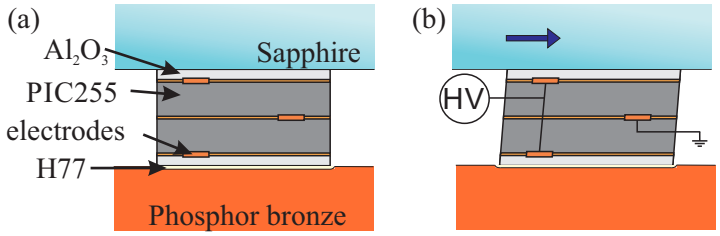

Figure 3.13: **(a)**: Sketch of a piezo stack glued on a frame of phosphor bronze and pressed against a sapphire surface. **(b)**: By applying a voltage, the piezo stack is expanded, leading to diagonal stretching.

3.3.1 Vertical coarse drive

For the coarse approach in z-direction, the well-established design by Pan *et al.* is utilised [40]. It features six piezo stacks positioned in sets of two at the sides of a triangular prism. From one direction, pressure is applied to one pair of stacks by a ruby ball tensioned by a leaf spring. The force applied to the stacks is then distributed via the sapphire prism to the other stacks. In figure 3.14(a), the design can be seen as it is implemented into the z coarse drive of the side scanning units. There, the scanner, which is mounted on its macor pedestal, is implemented in the triangular sapphire prism through a cylindrical hole in the prism's centre. One edge of the triangular prism is cut to shorten the distance between the side unit's S-scanner and the centre scanner. The three pairs of piezo stacks, shown in red, are pressed to the prism from either side. In the front, the leaf spring can be seen, which is tensioned by the four M2 adjustment screws around it. By applying pressure to the two

stacks in the front plane of the prism via the red ruby ball, the pressure is distributed via the prism equally to the other two sets of stacks. Then, the prism can be moved vertically by applying a saw-tooth voltage to the set of piezo stacks.

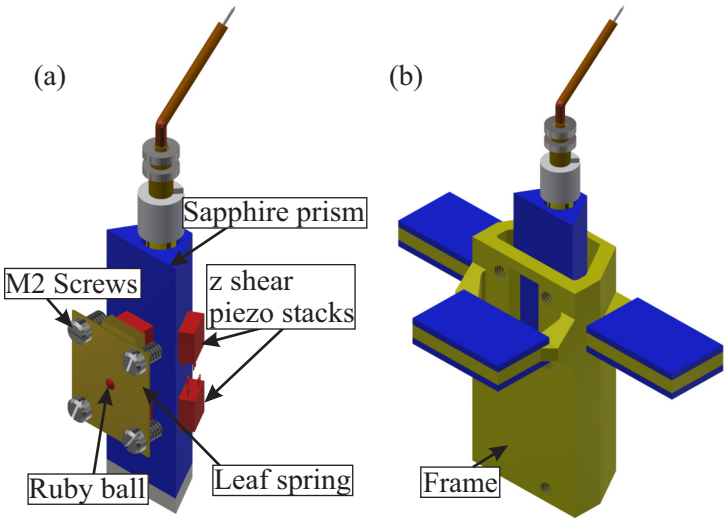

Figure 3.14: *Z* coarse slip stick motor, as it is utilised for the side scanning units in the MP-STM. It is based on the design by Pan *et al.* [40]. **(a):** 3D model of the implementation in the MP-STM. **(b):** The frame around the *z*-coarse motor as 3D model.

The *z* coarse motor stacks are glued to a frame made of phosphor bronze with H77 epoxy resin (the frame is transparent in figure 3.14(b)), and their contacts are connected to a board on the low end of the frame (not shown in the picture).

3.3.2 Lateral coarse drive

The frame that is depicted in figure 3.14(b) can be perceived better in figure 3.15(b). An old design for the lateral coarse motor to the left is compared to the new design, which is implemented now in the MP-STM. Both designs have the same basic principle. The frame that houses the scanning unit and the *z* coarse motor features three wing-like extensions, with sapphire plates glued to the top and bottom sides. The wings and, therefore, the sapphire plates are pressed from below onto a piezo stack each.
The stacks, which are shown in more detail in figure 3.15(a), are separated into two sections on top of each other, and the piezo ceramics of each section are rotated by 90° to the other. The stack can induce motion in *x*-direction with the lower half (blue) and in y-direction with the upper half (red). With pressure being applied between the sapphire plates and the stacks,

the load of the frame can then be driven laterally.

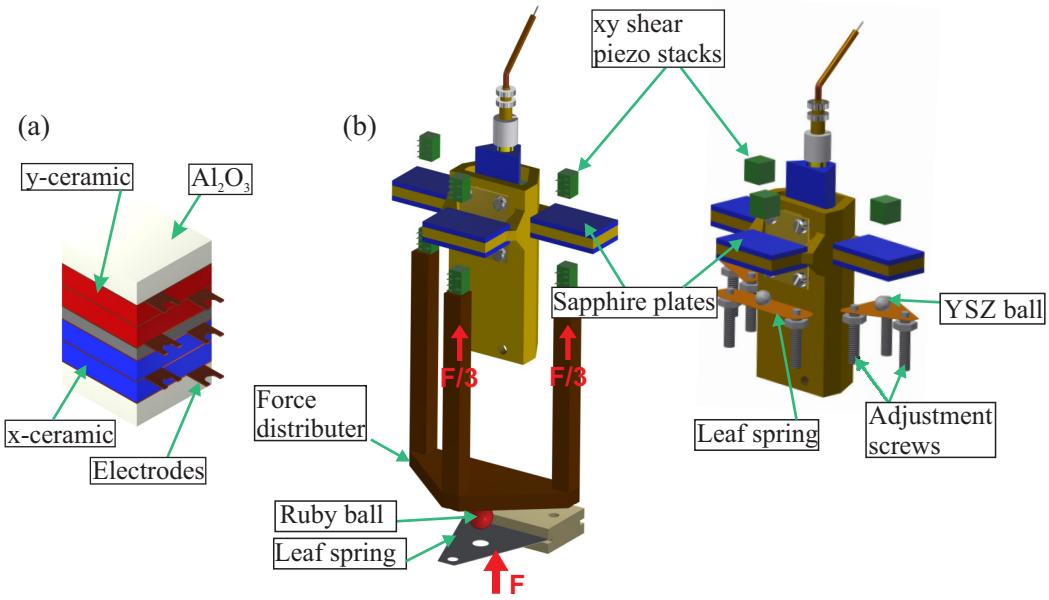

Figure 3.15: **(a)**: detailed view on the 3D model of the x-/y-stacks. They are built as slip-stick motors according to the principle shown in figure 3.13, but with two sections of ceramics that are rotated by 90° to each other. This way, the lower half can expand diagonally in x-direction and the upper half in y-direction. **(b)**: The old design (left) and the new design (right) of the lateral coarse motor. The force distributer, which forwards the pressure of one leaf spring to all three pairs of stacks, is replaced by a separate spring for each stack. Thereby, the amount of stacks is halved, which simplifies the problem with plane parallelism between the surfaces of the stacks and the sapphire plates.

In its previous design by Jonas Harm, the pressure between the piezo stack surfaces and the sapphire plates was applied by a large BeCu spring in the lower part of the MP-STM's body, as depicted in figure 3.15(b left) [20]. The spring was tensioning a ruby ball to a plate with three pillars that distribute the spring's force to the three stacks attached to the pillar's tops (the construction was therefore named force distributer). Thereby, the scanner unit's wings were sandwiched by two sets of piezo stacks.

Unfortunately, the design was not performing well and tended to malfunction at low temperatures. The investigation of the malfunctions led to the assumption of three main causes: First, the surface of the sapphire plates and the piezo stacks were not perfectly plane parallel to each other due to geometric imperfections, which led to uneven driving and the scanner unit getting stuck. Second, the force distributer was in light contact with its guideline through the microscope's body. This resulted in the pillars getting stuck or even cold-welding to the body surface since both had been gilded. Third, during the testing phase at temperatures as low as 9.4 K the adhesion bonds of the sapphire plates to the scanner unit's frames did not

endure the thermal stress arising due to intense cooling and the different thermal expansion coefficients of the materials, leading to the glued bond between the sapphire and the wings to breaking.
The surfaces of the piezo stack endings and the sapphire plates need to be as parallel as possible, as geometric deviations may lead to variations in the applied pressure between the stack and sapphire depending on the coarse drive's position or even to a partial loss of contact. As the static friction of individual stacks to their sapphire plates may be changed, they perform less, and the coarse drive can get stuck or be rotated in the x/y plane. Such a potential rotation is depicted in the sketch of figure 3.16.

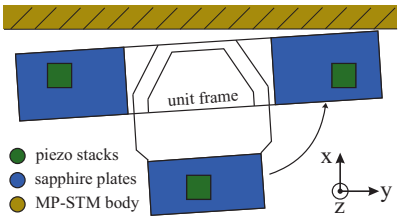

Figure 3.16: Sketch of the coarse drive frame rotating in the x/y plane due to one or more piezo stacks operating less (or more) efficiently than the others.

The old design relied heavily on the geometric accuracy of its components, which could not be achieved by the means of its construction. A new design was aimed at solving these issues by replacing the lower shear piezos and the force distributer entirely. Individual BeCu leaf springs for each of the remaining three stacks were installed. These are strained by adjustable titanium elevation screws introduced in the MP-STM's body (see fig. 3.15(b) on the right side). Each leaf spring is pressing a ball made of yttria-stabilized zirconia (YSZ) onto the sapphire plate above. By replacing the lower set of piezo stacks with balls, the total area of surface contacts that has the potential to be non-parallel is minimised, and the application of individual pressure forces for each remaining piezo stack simplifies the compensation of remaining geometric deviations.
With this new design, the scanning units reach a sufficient distance from the other probes and the sample stage, making an *in situ* tip exchange possible. The probes can be driven reliably to any point inside the coarse driving range.
Additionally, the new coarse motor design shows robust endurance to thermal stress, which is largely accomplished due to a new glueing method used for the adhesion of the sapphire plates to the scanning unit frames.
In the coarse drive's original design, a glueing technique was utilised that is well established for adhering small surfaces. The epoxy resin is applied in three to five dots in a symmetric pattern on the gilded phosphor bronze, which is being roughened beforehand to increase the contact surface. The sapphire plates are then pressed onto the wings, and the epoxy resin -in this case H20E- is cured at 150 °C for one hour [41]. By using the pattern of very thin resin dots, the sapphire plane is evenly adhered and the bond is uniformly flat. The adhesive

connections made with this technique bond strongly and perform well in ambient conditions and UHV conditions at room temperature [20, 42]. However, the resin bond apparently does not withstand the thermal stress induced by the intense cooling at low temperatures. In these cases, a failure of the coarse drive has been observed, which was caused by the breaking of the adhesive bonds due to the difference in expansion coefficients of the materials involved.
A new method of glueing with epoxy resins was developed with the counsel of the company Epoxy Technology Inc., which is distributing the epoxy resins, by testing a variety of different pre-treatments of the surfaces, epoxy resin types, application methods, and curing recipes. The most successful method shall be described shortly:

Pre-treatment:

First, the gilded surface is roughened with abrasive paper to increase the surface area available for the adhesive to bond to. By providing microscopic scratches and crevices that the adhesive can penetrate, it can form better mechanical bonds. To get rid of contaminations, the surface is then cleaned in an ultrasonic bath. Subsequently, aqua regia, a potent mixture of hydrochloric acid and nitric acid, is applied for 20 to 30 seconds to the surface. This increases the hydrophilicity and wettability of the gold surface. The epoxy resins, with active groups that are binding primarily hydrophilic [43], can therefore stick better to the surface. This is improving the interaction with the epoxy resin.

Epoxy resin type and application method:

The next step is to apply the resin EPO-TEK® EJ2189-LV in a layer of approximately 200μm thickness. The molecular chains originating from the reaction of the resin's two components can reach lengths of a few micrometres. By choosing a layer thickness too small, the length of the created chains and the entangling of the chains may be reduced. A chosen thickness of 200μm resulted in stronger bonds than for smaller thicknesses.

Curing recipe:

Although in the EPO-TEK® EJ2189-LV manual a cure at 150°C for one hour is recommended, a more gentle approach by using a stepped cure proved to be more efficient, extending the curing reaction at elevated temperatures. To give the molecular chains time to get entangled at elevated temperatures, the resin was first cured at 65 °C for two hours. Subsequently, the temperature was ramped up to 150 °C, which is hardening the epoxy resin more quickly, and kept there for another hour to finish the cure. Afterwards, the glued parts are left in the oven to cool slowly to room temperature.
By using a resin thickness of up to 200μm, the likelihood of achieving plane parallelism in the sapphire plates is rising, as the geometric deviations of the scanning unit's wing extensions can be compensated. Therefore, a fixture frame for the curing process was constructed, as shown in figure 3.17, where the scanning unit's frame is fixed in the centre cylinder by six grub

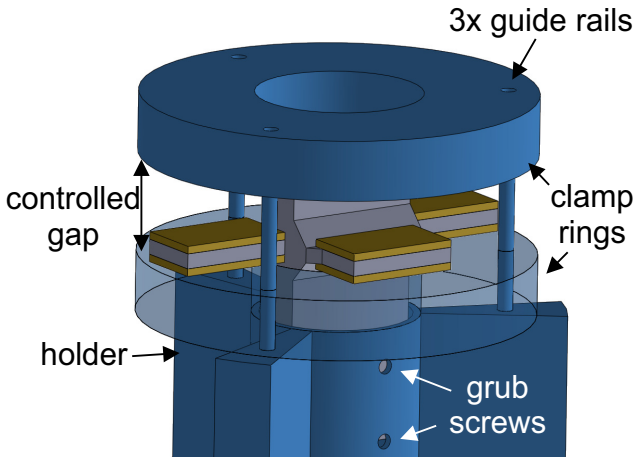

Figure 3.17: 3D model of the fixture frame for glueing the sapphire plates to the scanning unit's frames, with the frame included. To ensure parallelism between the sapphire plates, it is important that the clamp rings are precisely manufactured. This picture was created by P. Lindner in the framework of his doctoral thesis and is used here with his permission [21].

screws from three sides. The frame's wings are sandwiched by two precision-manufactured rings. The gap between the rings can be adjusted by threaded rods as guide rails and fixed with nuts at a desired distance. By measuring the gap size precisely using micrometre screws and adjusting it accordingly, the resin thickness can be controlled. This way, the deviation in thickness of the wings together with the sapphire plates and the epoxy resin in between was achieved to be below 20 micrometres, which is small in comparison to the deviations of the wings glued with the old method. These ranged from 100 μm to 200 μm.
One of the scanning unit's frames was glued this way and installed into the MP-STM's lateral coarse drive. The coarse drive was tested subsequently in UHV at temperatures of 293 K, 140 K, 65 K and 10 K. All tests yielded a successful drive operation over the whole coarse motor's range [44].

3.4 The sample stage

With the scanning units described above, one crucial component of the MP-STM is left to be described - the sample stage. Since it is designed for holding the sample in place while nano-scale objects are investigated on its surface, the sample must move as little as possible relative to the tunnelling probes. Therefore, to prevent mechanical movement due to vibrations and be able to exchange the samples *in situ* with a wobble-stick, spring-loaded holding mechanisms are commonly used. Furthermore, the sample must be strongly coupled thermally to the cryostat and to the tunnelling probes to cool down the sample efficiently and to have a thermal equilibrium between the probes and the sample. The latter is preventing microscopic motion between the sample and the tunnelling probes since they are thermally drifting apart if there is a thermal imbalance. Due to the expansion (or contraction) of the objects during heating (or cooling), the distance in between is changing when the components' temperature difference is changing.

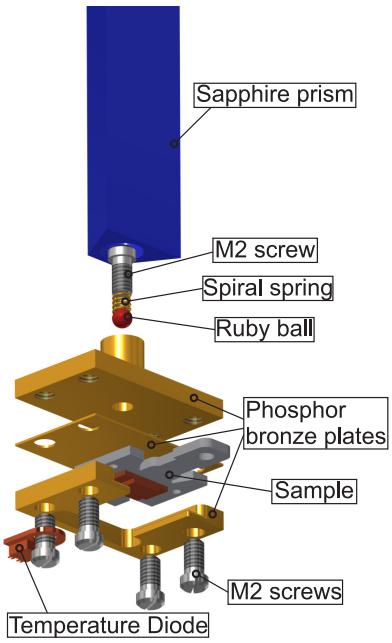

Figure 3.18: 3D Explosion model of the sample stage.

Figure 3.18 shows a 3D explosion model of the sample stage. It is implemented on a sapphire prism, being part of a $z-$coarse motor, which is of the same design used for the side scanning units. The stage consists of two 2 mm plates and a thin 0.25 mm plate made of gilded phosphor bronze that are bolted together. The sample is pressed against the bottom plate by a 2 mm ruby ball that is inserted into the cylindrical extension of the top plate together with a spiral spring and a M2 screw for fixation. The clearance hole in the top plate is large enough for the ruby ball to pass through, so it is pressed against the smaller clearance hole of 1.6 mm diameter in the middle plate. Thus, a part of the ruby ball is reaching through, which is pushed down by the spiral spring and holds an inserted sample right below in position. The cylindrical extension is inserted into the sapphire prism, where the prism's base is glued with epoxy resin to the sample stage's top plate and the cylindrical extension into the hole inside the prism. To connect the sample holder to the bias voltage, a cable is guided through the prism and connected to the screw via a washer soldered to it. Finally, the sample's temperature is monitored by a silicon diode bolted to the sample stage (DT-670A1-SD Lake Shore

Cryotronics [45]). This ensures the most accurate temperature measurement of the sample using temperature diodes. With another diode on the STM's body (diode B), the temperature difference of the microscope's body can be determined (with the error rates of the diodes in consideration). This way, it can be assessed if the MP-STM is in thermal equilibrium, although it should be noted that the tunnelling probe's temperature cannot be adequately monitored in this manner. The microscope's body is made of phosphor bronze, which is a compromise between machinability of the components and fit of thermal conductivity since its thermal conductivity is lower than that of oxygen-free copper or silver [46, 47, 48], but does in contrast not deform during CNC machining. Together with the sapphire prism and the piezo stacks of the coarse drive, the MP-STM's body is forming a bridge between the cryostat and the scanning units.
These implementations ensure that a sample is effectively thermally coupled to the helium bath cryostat. Additionally, it is fixed stiffly in its position, preventing any movement of the sample relative to the sample stage and the tunnelling probes while allowing for easy sample exchange.

3.5 Optical tip to tip approach

For three-probe experiments, the tunnelling tips need to be in proximity to each other. Their minimal geometrical distance, which was defined in section 3.1, is in the nanometre range. It is not possible to approach the tips relative to each other by eye or with conventional high-resolution camera systems.
While the tunnelling probes in conventional scanning tunnelling microscopy are approaching a sample at a similar or even smaller distance, approach algorithms are used, which do not rely on the exact location of the probe. Rather, they rely on the fact that the sample surface is much larger in comparison to the tunnelling probe and cannot be missed. Multiple tunnelling probes, in contrast, are too small to approach each other without localising them. In other multi-probe STM setups, this is done by utilising scanning electron microscopes (SEM) or optical microscopes at close distance [49, 50, 51, 52, 53, 54]. These cannot be used for the MP-STM. The presence of an external magnetic field prohibits the use of a SEM since the field would interact with the electrons. Furthermore, SEMs are causing beam damage and organic contamination of the samples being imaged [55].

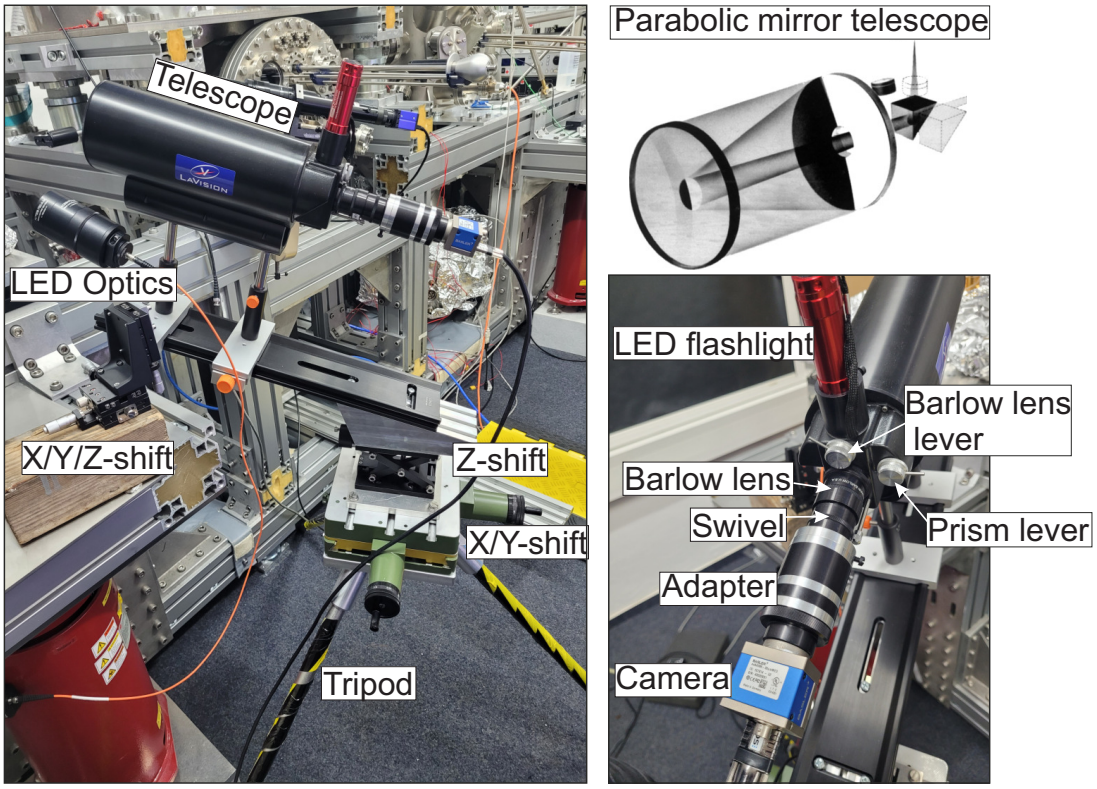

Figure 3.19: **Left:** Photograph of the long-distance microscope (LDM) and its LED optics. The LDM is mounted with a Z-shift and an X/Y-shift onto a tripod. The LED optics are mounted on a combined X/Y/Z shift. **Top right**: schematics of the components comprised in the LDM's telescope. There are two parabolic mirrors shown, which are focusing the incoming light onto a central port. From there, the light can be deflected to a top port by a retractable prism, either directly out or into a retractable Barlow lens. **Bottom right:** A photo of the LDM's rear showing the optics between the telescope and the high-resolution camera, the levers for retracting the prism, and the Barlow lens inside the telescope. On the top port, an electric torch is mounted, which is used to adjust the position of the LDM.

Optical microscopes are too large to fit into the confined space of the STM chamber close to the MP-STM's sample stage. However, the control by optical means can be implemented from outside the UHV chamber. The only visual access to the MP-STM is through the STM chamber's viewport, which is positioned at a distance of 500 mm from the tunnelling point of the microscope, which is located in cryostat's centre shown in figure 2.2 in chapter 2. To reach an optical resolution of a few μm from such a distance, an optical long-distance microscope (LDM) from Questar Corp. is used [56]. With a focus point at a variable distance of 550 mm to 1520 mm, the LDM can be positioned in front of the STM chamber's viewport with its focus positioned on the tunnelling point. It is depicted in figure 3.19, showing the setup as a whole on the left side and the individual components of the LDM on the right. The LDM comprises a Maksutov telescope using a Cassegrain configuration, which is shown

in a sketch on the top right in figure 3.19, and an array of optical components on the telescope rear adapted to a high-resolution camera, which is shown on the bottom right in figure 3.19. The light passes through the front lens to the telescope's back and is reflected by a concave primary mirror with a hole in its centre. It is then reflected onto a secondary convex mirror at the front lens, which focuses the light through the hole in the primary mirror into the telescope's rear. There, it can either pass through the central port or be deflected by a retractable prism, which is illustrated in both possible positions. When deflected, the light is passing through the top port. On this path, a retractable Barlow lens can be positioned in the light's path. Both of its positions are illustrated in the image as well.
The Barlow lens, named after Peter Barlow, is a diverging lens that increases the effective focal length of an optical system and magnifies the projected image [57]. When looking through the top port by eye or installing a torch light on it, the focus point of the LDM can be localised more easily, which is helpful for adjusting the LDM's position. The right bottom image in figure 3.19 is showing the LDM's rear with the levers used for positioning the prism, the top port's Barlow lens with an electric torch installed to it, and the central port. On the central port, another Barlow lens and a swivel are installed in front of an adapter connecting the high-resolution camera from the Basler AG to the LDM. The swivel is allowing a 360° rotation of the image, which is projected through the LDM. It is mounted onto an angled block connected to a Z-shift on top of an X/Y-shift. The angle is adapted to the angle between the tunnelling point in the MP-STM and the viewport of the UHV chamber. Since it is too heavy to fixate it to the chamber system's profile table because it would affect the system's centre of mass, the LDM, together with the Z- and X/Y-shifts, is rested on a tripod separated from the chamber system. The LDM images an area of 1 mm x 1 mm [56]. This area is too small to be illuminated sufficiently by ambient light. Therefore, it is illuminated by a high-intensity LED, which is focused by lenses on the focal point of the LDM. The LED shines on a 1 mm x 1 mm area with an intensity of about 6.5 mW [58]. This light source is itself mounted onto an X/Y/Z-shift, which can be used to adjust its light spot.
The LDM was first tested before the installation of the MP-STM into the UHV chamber system. In figure 3.20, the setup of the MP-STM and the LDM is shown. A low-resolution camera system, which was previously used for the tip-to-sample approach, is now also used for the tip-to-tip approach. For testing, it serves as a comparison to the LDM. It is depicted in figure 3.20 as well. The MP-STM was tested in ambient conditions to ensure its functionality prior to its installation. The LDM was used to localise the right tunnelling tip, approaching the centre tunnelling tip. The objective of this experiment was to achieve overlapping scan ranges on highly oriented pyrolytic graphite (HOPG). The experiment is further presented in section 4.3 below.

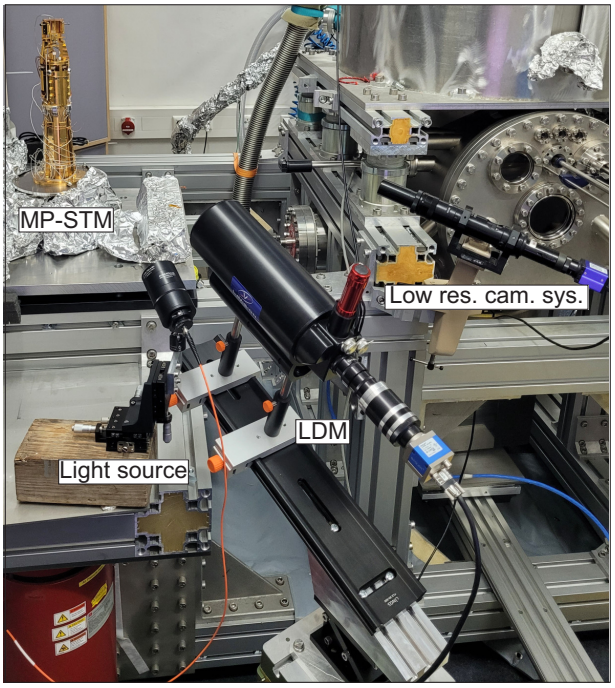

Figure 3.20: The LDM and the LED light source during the first use of the MP-STM prior to its installation into the UHV chamber system. The objective was to test the optical approach of the microscope's right tunnelling tip to the centre tip and achieve an overlap in the scanning unit's scan ranges. The low-resolution camera system, which was previously used for tip-to-sample approaches, can also be used to approach the tips to each other. For testing, it serves as a comparison to the LDM.

Some optical images made during this experiment are shown in figure 3.21. Figure (a) shows the image made by the low-resolution camera system, which features a resolution in the sub-mm range. Figure (b) shows the same tip array, but the image was made with the LDM. In the image, the distance between the tips is better visible. The real tips are below, and their reflections are above the HOPG surface. Both images (a) and (b) show the tunnelling point illuminated in white light. For this, not the LED light source but a very strong white electric torch light was used. The HOPG surface is well visible in (b), showing fine ripples of HOPG flakes on the surface, where only a flat surface would be visible using the low-resolution camera system. Figures 3.21(c) and (d) show the centre and the right tip imaged with the LDM while they are illuminated with the LED monochromatic light source (470 nm$\pm$20 nm [58]). This light allows for a higher optical resolution, which can be identified by the airy discs of the reflections on the tip's surfaces. By measuring the diameter of the first-order airy discs, the optical resolution of the LDM was determined to be around 3 μm.
The distances in the images 3.21(b-d) were calibrated using the known diameter of 250 μm

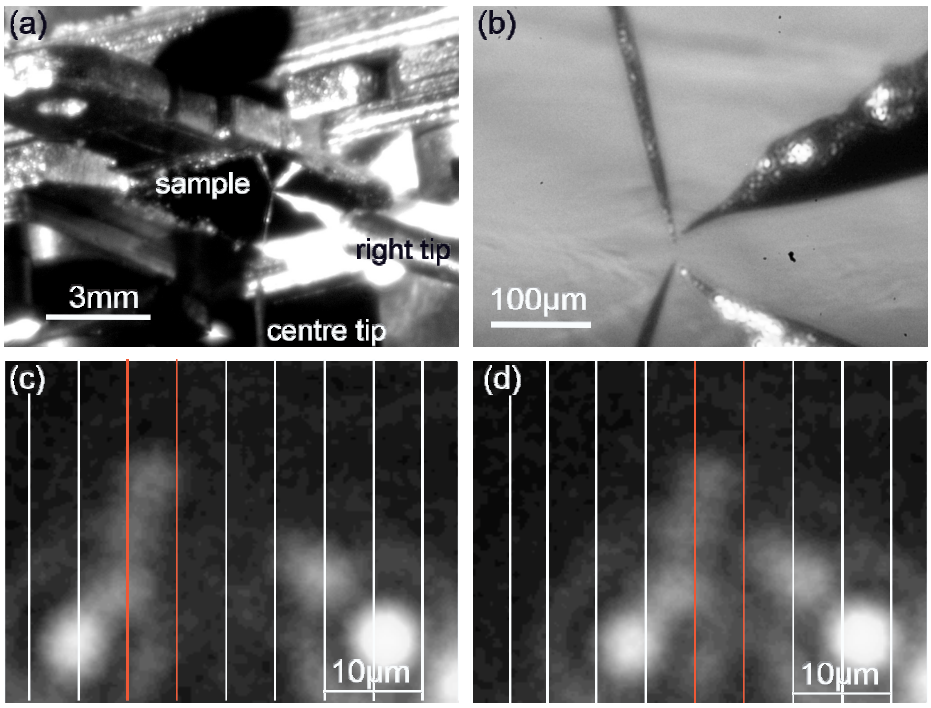

Figure 3.21: Images of the centre and the right tip close to a HOPG sample. Image **(a)** was made with the low-resolution camera system, which allows for a resolution in the sub-mm range. The right and centre tips are marked with R and C. Images **(b-d)** were made with the LDM. **(b)** shows the same tip configuration as in (a) illuminated with white light. Both the microtips (lower part), the HOPG surface, and the tips' reflections (upper part) are well distinguishable. Images **(c-d)** are illuminated by the blue LED and zoomed closely to the tips. The position of the tunnelling junction can be located with an uncertainty of the LDM's resolution. Image **(c)** shows the centre tip in maximal displacement to the left (x-direction), and image **(d)** shows it in maximal displacement to the right. The red lines mark the approximate position of the microscopic centre tip in both images. A travel distance from the leftmost to the rightmost displacement of about 7 μm$\pm$3 μm can be identified.

of the centre tip's shaft. The image used for calibration is not shown here. With a maximal lateral scan range of 6 μm at room temperature (see calibration in section 4), the LDM is able to record the lateral scanning movement. In image (c), the centre scanner is displaced to the very left of its range, which is illustrated with the white and red stripes. The approximate position of the tunnelling junction is in between the red stripes. In image (d), the scanner is displaced to the very right of its range, with the red stripes marking the new position. When comparing (c) and (d), a movement of a few microns can be observed. The tip's approximate position is moving a little less than two stripes to the right.

With this resolution, the right tip could be positioned within the scanning range of the centre scanner while being displaced to the left end of its range. At low temperatures, the scanner's

ranges are expected to be only half of the values at room temperature due to the temperature dependency of the piezoelectric effect. Thus, the scan range is close to the optical resolution at low temperatures, and the side tips can probably no longer be positioned directly into the centre scanner's range. However, with an optical resolution close to the lateral scan range of the tube scanners, an approach is still possible. When driven with the coarse drive as close as possible to the centre tip, the side scanning unit can image the sample surface within its range, which can be compared to the scan range of the centre tip. If no similar features are found, the scanning unit can be moved in the direction of the centre tip by the coarse drive, and the process is repeated. A similar approach was done previously by A. Leis *et al.* with a four-probe STM utilising a microscope positioned directly above the probes with an optical resolution of 2 μm [51]. As will be shown in section 4.3, this was successfully conducted with the LDM at a distance of 560 mm with a similar optical resolution of about 3 μm. Furthermore, in [51], the microscope was imaging the tips from above. This top view was gaining no information on the z-dimensions of the tips. The LDM is pointed at an angle towards the sample, imaging all three dimensions of the tips. While it is more challenging to reconstruct the tips' precise position in lateral dimensions, their three-dimensional shape and position can be reconstructed, limited only by the microscope's resolution.

3.6 Cable management

In contrast to most conventional STM setups, where just one vertical coarse approach and one tube scanner for the tunnelling probe is utilised, the MP-STM is equipped with two side scanners additionally that utilise a coarse step motor in lateral and vertical directions and an S-scanner each. Thus, the amount of electrical components implemented in the MP-STM is considerably larger in comparison to other STM setups.
For each driving direction of the coarse step motors, two contacts are needed, where one is connected to the electrical ground. With the x- and y- direction of the lateral coarse motors being on the same ground, this adds up to a total of 12 contacts implemented for three z and two x/y coarse motors. For the tube scanners, even more contacts are needed since each electrode on the scanner's outer surface is contacted individually. This adds up to five contacts for the conventional central tube scanner and nine contacts for the two S-scanners. Together with the cabling for the tunnelling tips, for the bias voltage that is applied to the sample, and for two temperature diodes (A and B) with four contacts each, a total of 47 contacts exist in the MP-STM setup. These collimate into two semi-circles made of poly-ether-ether-keton on the microscope's low end (further referred to as PEEK rings) that are shown schematically in figure 3.6 on the left-hand side. There, the contacts for the individual components are

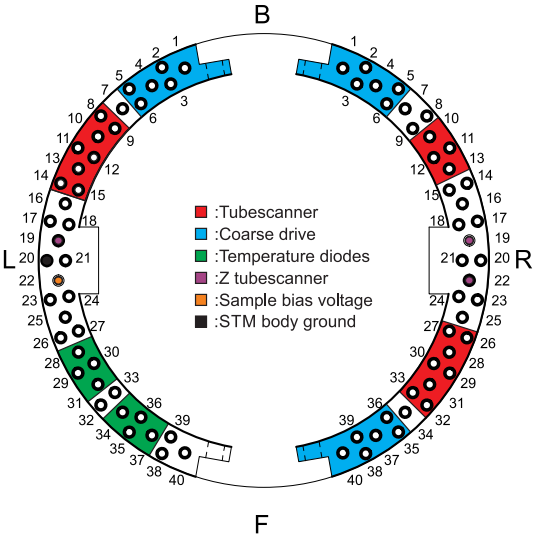

Left		Right	
1		1	
2	XL	2	
3		3	
4	YL	4	
5	ZL	5	ZM
6		6	
7		7	
8	xL1-	8	
9	xL2+	9	
10	xL1+	10	xM+
11	xL2-	11	yM+
12	yL2-	12	xM-
13	yL1+	13	yM-
14	yL1-	14	
15	yL2+	15	
16	Gr	16	Gr
17	Gr	17	Gr
18	Gr	18	Gr
19	zL	19	zM
20	Gr	20	Gr

Left		Right	
21	Gr	21	Gr
22	U	22	zR
23	Gr	23	Gr
24	Gr	24	Gr
25	Gr	25	Gr
26		26	xR1-
27		27	XR2+
28	T1(A)	28	xR1+
29	T2(A)	29	xR2-
30	T3(A)	30	yR2-
31	T4(A)	31	yR1+
32		32	yR1-
33		33	yR2+
34	T1(B)	34	
35	T2(B)	35	
36	T3(B)	36	ZR
37	T4(B)	37	YR
38		38	
39		39	XR
40		40	

Figure 3.22: **left:** Diagram of the two semi-circle connectors at the MP-STM's bottom end viewed from the top. In the coloured regions, PEEK connectors of similar shape are connected. They can be separated into groups of electric components, as shown in the legend. B, L, R, and F are referring to the back, left, right, and front. **right:** Table of the numbered contact sites on the PEEK rings. As indicated by the black brackets, the lateral electrodes of the bottom half of the S-scanners are connected to their neighbouring contacts that are contacting the point-symmetric mirrored electrode on the S-scanner's top half.

ordered by type and their respective scanning units. Ordered as such, the contacts are then placed on different sections of the rings, which are marked in the diagram with different colours referring to the component type. On the right-hand side of the figure, the contacts referring to the numbers on the rings are listed. Here it is also noted to which scanning unit the contacts belong, including the L, M, and R in the captions for left, middle, and right. The diodes are marked by (A) and (B), where diode B is attached to the MP-STM's lower body and diode A is attached to the sample stage, as mentioned in section 3.4.

For the electrical contacts between the PEEK rings and their components, Kapton® isolated copper cabling with 0.2 mm diameter is used as twisted pairs. The twisting of the cables reduces crosstalk and noise effects on them since the fields emitted by the twisted cables cancel each other, thereby reducing the electromagnetic interference. The cabling was chosen to be very thin since it connects to moveable components. However, an even better way to shield a cable from electromagnetic noise is to use coaxial cabling, which was done for the sample bias voltage contact.

Except for the three contacts to the tunnelling tips, every electrical component implemented in the MP-STM is connected to the PEEK rings. Hereby, they are forming the interface

between the microscope's internal cabling and the external cabling that is guided to the outside of the UHV chamber and to the control electronics. On the rings, stackable pins are mounted (number 0462 from Mill-Max Manufacturing Corp.), and below the rings, PEEK connectors are mounted to the ring, facing away from the microscope (right below the coloured regions in figure 3.6). The connectors are constructed similar to the ring sections, with the same kind of pins that can be pushed into the pins on the PEEK rings. From these, the cabling is then guided outside.

Not all of the remaining 44 contacts are connected to the outside, though. The electrical ground of each of the microscope's components and the microscope's body are connected to the contacts 17-24 on each half ring (Gr marking in the table). This way, every component is focused on one common ground and connected to the outside of the UHV chamber with one contact line. This is necessary to reduce the risk of ground loops that could induce electrical noise, since the number of conductor loops connected to the ground potential is greatly reduced by using only one contact leading to the outside. Also, the contacts of the side S-scanners are reduced in number (large red areas in figure 3.6). Since the scanners are driven with the same voltages but with opposite signs, the contacts of the bottom half can be connected to the point symmetrically mirrored contacts on the top half. These are labelled in the table of figure 3.6, with $x/y+/-$ referring to a coordinate system of a point of view from the microscope's front, L or R referring to the left and right scanning units and 1 referring to the bottom, and 2 referring to the top half of the S-scanner. Thus, the neighbouring contacts, e.g. xL1- (referring to negative x on the lower half), are connected to xL2+ (referring to the positive x on the upper half), which is indicated by the brackets in the table. This reduces the number of cables needed for the side unit's S-scanners to five each. Overall, the amount of contacts being guided out of the UHV chamber is this way reduced to 32. This is advantageous because every cable is connecting the UHV chamber wall thermally to the microscope. To reach temperatures as low as 1.5 K the microscope needs to be decoupled from warm sources like the room-temperature chamber wall. Therefore, these thermal bridges need to be as few and as long as possible.

This is why the cabling material, the cables' length, and their route through the cooling anchors of the UHV cryostat are important. For the present, stainless steel coaxial cables and coaxial twisted pair cables were chosen. As discussed in earlier works, stainless steel has a low thermal conductivity, making it an excellent choice for thermal decoupling [19, 20, 42]. However, it should be mentioned that it is not an ideal choice for higher-frequency signals since they have a relatively high resistance and low bandwidth. To reduce the temperature gradient, a cabling route was chosen where the cables are fixed to long paths on cooled components. This is described in more detail in section 3.7.

To transmit RF signals to the tunnelling probes with low loss, flexible silver-plated copper coaxial cabling (low-loss microwave coax 24AWG from molex®[35]) is used from the SMPS RF-compatible connectors of the tunnelling probes through the MP-STM's body towards the thermal shielding connected to the helium bath cryostat. They transmit RF signals highly efficiently, with a signal attenuation of 5.7 dB/m in comparison to stainless steel coaxial cabling with an attenuation of 33 dB/m and are efficient thermal conductors, anchoring the tunnelling probes to the microscope thermally. In the rear of the microscope, they are connected to coaxial cabling that is guided to the back wall of the UHV chamber on a much shorter path in comparison to the other cabling. The length of the RF cabling line has a crucial impact on its transfer function, with a longer line leading to higher signal loss [19, 20, 42].
Since stainless steel is not suitable for RF applications, semi-rigid beryllium copper (BeCu) coaxial cabling was used for the previously installed RF-SP-STM, which is a compromise between thermal decoupling and RF signal transfer. One drawback of this approach is the vibrational coupling via the semi-rigid cabling. Thus, flexible cabling was chosen for the RF line inside the MP-STM. Also, the side scanners must be moveable and cannot be connected by semi-rigid coaxial cabling.
The silver-plated coaxial cables, being excellent thermal conductors, were replaced from the helium bath thermal shielding to the feedthroughs at the UHV chamber's walls by the more thermally insulating stainless steel cables for the first experiments that utilise lateral DC currents. However, for the experiments that rely on RF signals, like pump and probe experiments, the cables can easily be interchanged and updated without the need to demount the MP-STM from the UHV chamber.

3.7 Installation into the UHV chamber

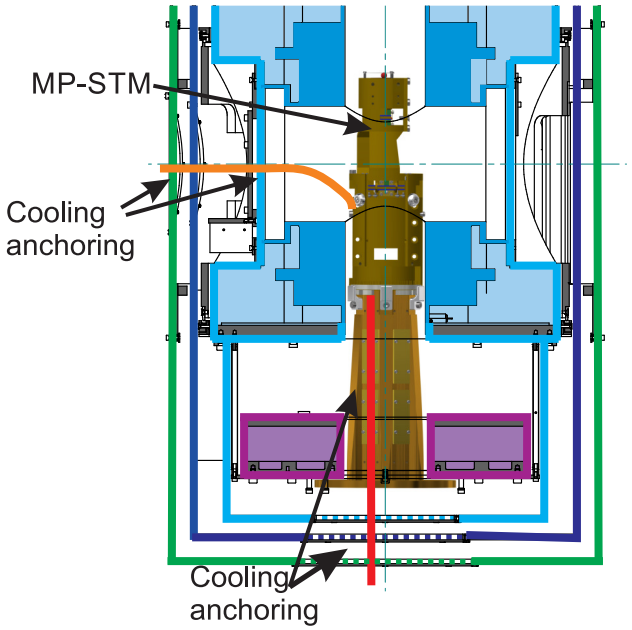

Figure 3.23: Sectional side view of the bath cryostat inside the STM chamber with the MP-STM included. The MP-STM is mounted onto a pedestal, which is bolted to the 1 K pot (described above in chapter 2). The path of the tunnelling probe's cabling, which is guided through the cryostat's rear, is marked in orange. The rest of the cabling, including the cabling for the coarse approach, tube scanner, bias voltage, and temperature diodes, is guided through the bottom of the cryostat. Its path is marked in red.

As described above, the cabling is connecting the MP-STM to the UHV chamber walls thermally. Since it has to be cooled down to 1.5 K, the cabling must be optimised by choosing a long path with cooling anchors towards the cold environment. The STM chamber's cryostat, which was described in chapter 2, features three thermal radiation shields. These are cooled directly (or indirectly, in the case of the helium exhaust shield) by the helium and nitrogen baths. As shown in figure 3.23, the microscope's cabling is separated into two paths. For the installation of the MP-STM and its cabling, each shield features mounting holes that can be covered. At each thermal interface, the cables are thermally anchored to the shield coverings. The path shown in orange, which is leading to the rear of the chamber (left in figure 3.23), includes the cabling of the tunnelling probes. The red path goes through the bottom of the thermal shielding and includes the cabling for the coarse and fine motion components, the temperature diodes, and the sample bias voltage. In the following, the cooling anchors of both paths will be described and how the cabling is implemented into them.

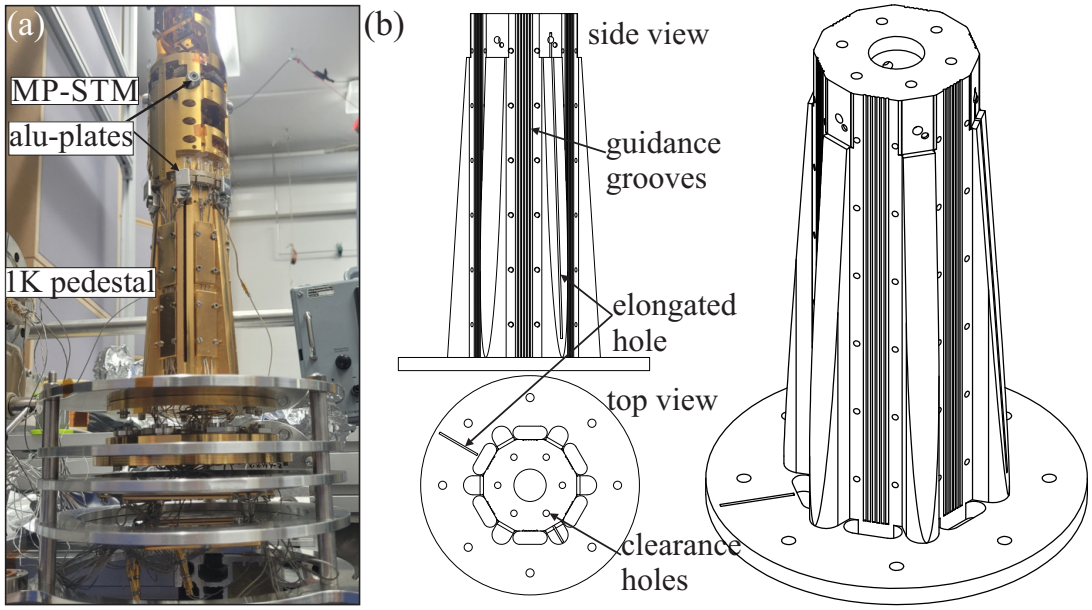

Figure 3.24: **(a)** Photograph of the assembly of the MP-STM and its cabling together with the shield coverings and the pedestal on a test table. The test table is mimicking the array of thermal shieldings inside the UHV chamber. **(b)** More detailed drawing and 3D model of the pedestal.

As shown in the photograph in figure 3.24(a), the MP-STM, the pedestal, and the shield coverings were installed on a test table prior to the installation. The table serves the purpose of mimicking the array of thermal shieldings inside the UHV chamber. Thus, the design and the construction could be tested, and errors could be avoided. Since the tube for housing the microscope is very narrow, small aluminium plates have been mounted around the MP-STM's body and the pedestal, where the lateral coarse drive and the PEEK semi-rings are located, to shield these delicate pieces from collisions during the installation.
A schematic drawing of the pedestal is shown in figure 3.24(b) in more detail. The interface to the microscope can be seen in top view, where it is bolted to the pedestal through six clearance holes. The cabling is guided from the PEEK ring down in grooves along the pedestal's side, where they are fixated by small plates, forming the 1 K cooling anchor. The pedestal and its fixating plates are made of gilded oxygen-free copper (OFHC), since copper is highly thermally conducting and the gold prevents corrosion and increases the copper's reflectivity. To prevent eddy currents that may develop in the copper during a ramp-up of the magnetic field, an elongated hole was cut into the side and the base plate, which is interrupting a potential circular eddy current path.

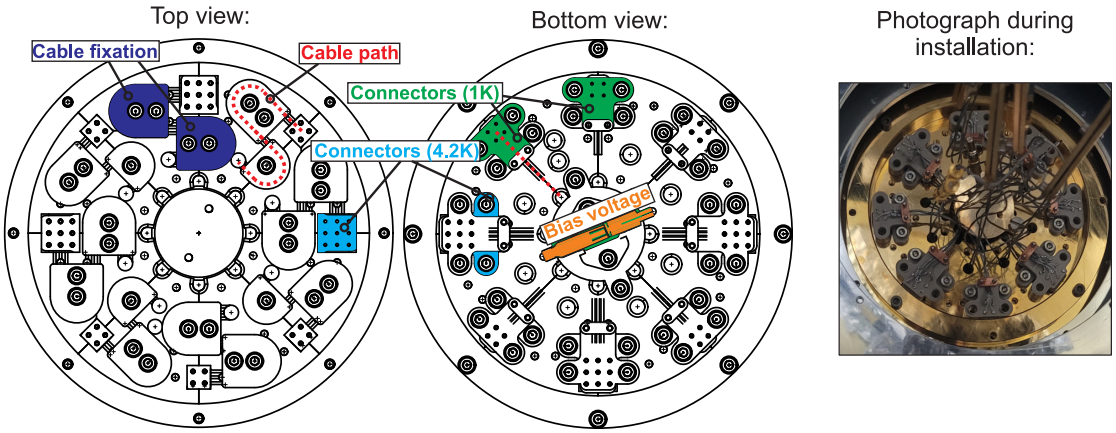

Figure 3.25: Schematic of the top and bottom views of the helium bath shield covering and a photograph taken during installation. The cabling coming from the MP-STM (1 K, green) is connected to the fixed connectors of the shield covering (4.2 K, light blue). The cabling is guided in grooves on the top side (red dotted path) and fixated by semi-circular plates. At the path's end, they are fed through the covering again, down to the next thermal shielding. The central hole is covered by a smaller plate, onto which a D-sub connector for the bias voltage is mounted (orange).

For the installation of the MP-STM and its pedestal, three threaded rods are screwed into the 1 K pot that guides the microscope, while it is lifted by a hydraulic elevator into the chamber. Subsequently, with the microscope installed, the shield coverings are installed one after another. For the covering of the 4.2 K shield, a gilded OFHC plate was used, which is depicted in figure 3.25 as a detailed drawing from the top and the bottom and in a photograph that was made during installation. The cabling coming from the 1 K anchor is fed through a hole in the plate's centre and finished as PEEK connectors (marked in green) that are connected to their counterpart connectors on the plate (marked in light blue). The connectors feature the same kind of pins used at the PEEK ring in the MP-STM. Therefore, the coaxial cabling's conductors are split into inner conductors and outer conductors -which are on ground- and connected separately to the pins. From there, the cables are guided through grooves on the plate's top side and fixated there by semi-circular plates, forming the 4.2 K anchor. In figure 3.25, the cabling's path is marked by the red dotted line that is guided under the semi-circular plates (marked in dark blue). At the end of the path, they are fed through clearance holes and connect down to the next cooling anchor on the helium exhaust shield. The 4.2 K shield's centre hole is capped by a smaller covering, onto which a single D-sub-connector is mounted (marked in orange). The D-sub-connector is connecting the coaxial line for the bias voltage, not dividing the inner and outer conductors like in the other cases. This was done because the bias voltage is the most delicate signal transmitted on this path.

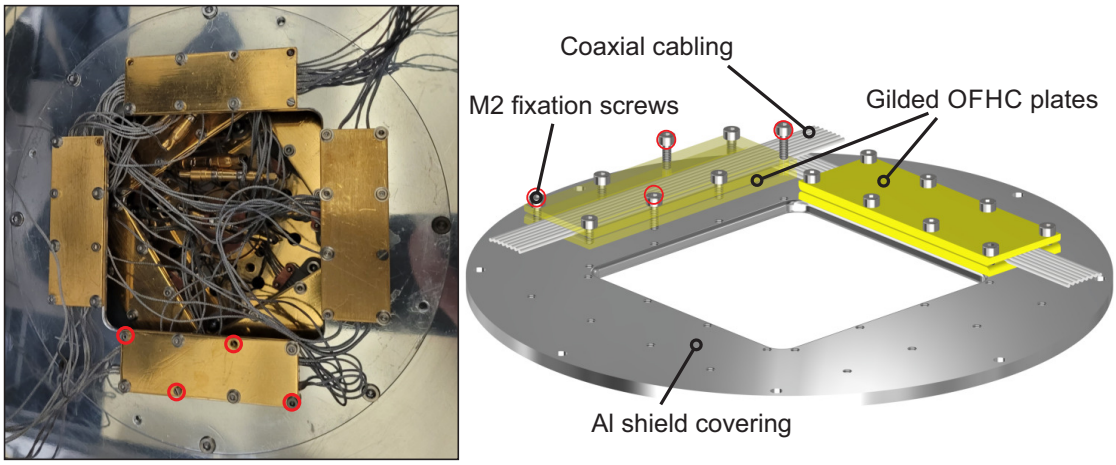

Figure 3.26: Shield cover of the helium exhaust shield and the 77 K shield. In the photograph on the left, the nitrogen shield cover with the OFHC cooling plates is depicted during installation. On the right, a 3D model of the shield covering is shown. The cabling is guided in the grooves of the gilded OFHC plates, which they are sandwiched in. The plates are bolted to the covering plates at the positions marked with red circles. The design of both shield coverings is similar but differs in size of the aluminium plates.

The shield coverings for the exhaust gas shield and the 77 K shield are designed similarly albeit in different sizes. In figure 3.26, a photograph of the 77 K shield covering during installation and a 3D model of the same are shown. They comprise an aluminium plate with a square hole in the centre each. The cabling is sandwiched into gilded OFHC plates that are bolted together with four 4 mm-long M2 screws. The plate sandwiches are then bolted to the aluminium plates with four additional 8 mm-long M2 screws. The sites at which the plates are bolted to the aluminium plates are marked with red circles in figure 3.26. Thus, the plates are forming the cooling anchors of the exhaust gas shield and the 77 K shield. The square holes give enough space to guide the cables in long spirals, which decreases their temperature gradients. For shielding the thermal radiation, a plain plate can be mounted onto the 77 K shield covering in the end. The cabling is guided to the sides, reaching four CF63 feedthroughs at the UHV chamber's walls.

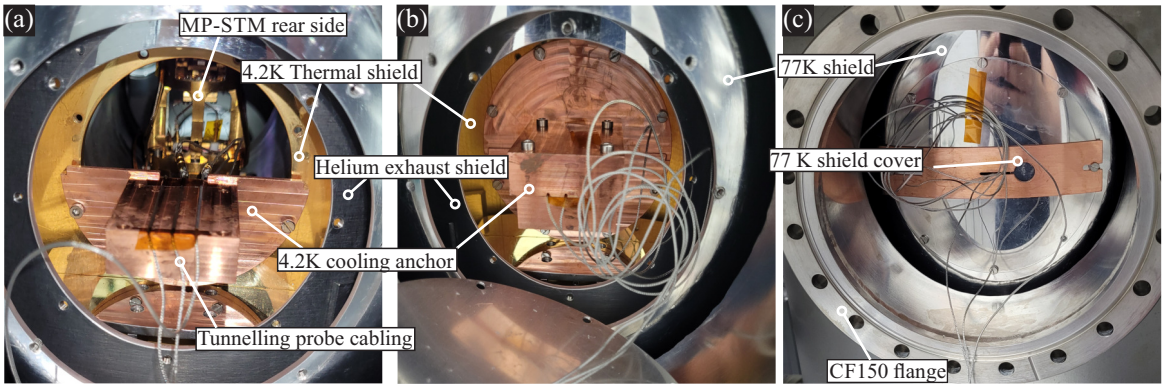

Figure 3.27: Photographs of the 4.2 K cooling anchor of the tunnelling probe's cabling path and the 77 K shield covering during installation. The components are cooled by the 4.2 K shield and the 77 K shield, which are connected to the respective helium and nitrogen baths.

The path of the cabling for the tunnelling probes in the cryostat's rear is much shorter to prevent signal loss in the RF-line. Due to space restrictions, it passes cooling anchors only in the 4.2 K and the 77 K shields. The cooling anchors are depicted in figure 3.27 and have been designed by J. Friedlein [1]. As shown in figure 3.27(a), the 4.2 K cooling anchor comprises an OFHC block with three grooves, into which the three tip cables are put. The cables are fixated then by a second block bolted onto the first and covering the hole in the 4.2 K thermal shield, as shown in the lower picture of figure 3.27(a). Since the copper blocks are reaching through the helium exhaust shield as well, the next cooling anchor is the 77 K shield covering shown in figure 3.27(b). It comprises a cover plate with a clearance hole in the centre and a copper strip upon it. The three cables are fed through a horizontal slit through the copper strip. From there, the cables are connected to CF 16 feedthroughs installed into a CF 150 flange. To account for the greater heat influx due to the cables being shorter, BeCu semi-rigid coaxial cables have been in use for the single-tip RF-STM previously. As described above in section 3.6, flexible stainless steel coaxial cabling is in use currently.

Chapter 4

MP-STM performance

Subsequent to its construction, the MP-STM was tested first in ambient conditions on top of an air-cushioned table and later in an UHV testing chamber. During this phase, the fundamental functionalities of the microscope, like the coarse and fine motions, were tested. Parallel to test measurements on well-known sample systems like Au(111) and HOPG, the scanning units were calibrated at room temperature and later at low temperature (67 K in the case of the centre scanning unit). Apart from the basic requirements for standard STM, the application of lateral currents was also tested, which is presented later in chapter 6. While the functionality of the MP-STM was proven, the test period was also drawing our attention towards important improvements to be added prior to the microscope's operation in its predestined UHV chamber system. For example, one of these improvements was the deployment of the LDM, since the importance of optical localization of the tunnelling tips for three probe experiments was emphasised during the lateral current experiments.
This was leading to a second testing phase directly prior to the installation into the UHV chamber, with the MP-STM being mounted onto the damped aluminium profile table of the UHV chamber system. In the following, the calibration of the MP-STM during the first testing phase will be presented first, showing the basic capabilities of the STM. Subsequently, the performance tests important for three-probe experiments are the simultaneous operation of all three scanning units and the approach of side tips into overlapping scan ranges of the centre and the side scanning unit will be shown. Those were done during the second testing phase, directly prior to the installation of the MP-STM into the UHV chamber system.

4.1 Calibration

For Au(111) and HOPG, the period of the atomic lattice and the mono-atomic step height are known from literature [59, 39, 60], and the features measured by the STM in constant-current mode can be calibrated accordingly. By comparing the measured data with literature values, a calibration coefficient C_i can be extracted that relates the tube scanner's physical displacement to the voltage applied to its electrodes for inducing such displacement. For each tube scanner, two calibration factors can be determined. One for the lateral displacement, which is equal in x- and y-direction, C_{xy}, and one for the vertical displacement C_z. The inert nature of gold makes Au(111) a very stable and easy-to-prepare surface, which features small terraces with mono-atomic step edges. The well-known height of the step edges can be used for the vertical calibration by determining the coefficient C_z. For lateral calibration and the determination of C_{xy}, HOPG is a good choice. It consists of micro-metre-sized grains of monocrystalline graphite with a highly oriented structure and is known for its large, atomically flat terraces with low amounts of crystal defects and contamination. Graphite exhibits a layered-type structure with a honeycomb lattice of planar sp^2 bound carbon atoms and a bond length of about 0.142 nm. The individual layers are stacked in an ABAB configuration along the [0001] direction as shown in figure 4.1(a) and are bound to each other by the relative weak van der Waals interaction. Therefore, the atomic layers can easily be cleaved, and a few of the topmost sheets can be removed by pulling them off with adhesive tape. This easy preparation and the large terraces make HOPG an ideal substrate for the scanner calibration. As seen in the model in figure 4.1(a), due to the ABAB stacking, the carbon atoms of the top surface layer, marked in blue and yellow, lie above different lattice sites of the carbon layer below. The atoms marked in blue are located above the carbon atoms of the underlying layer, and the atoms marked in yellow are above the empty centres of the carbon hexagons below. Due to this carbon site asymmetry the local density of states (LDOS) near the Fermi energy is different, i.e., the yellow atoms appear higher in STM images, thereby forming a triangular lattice [59].

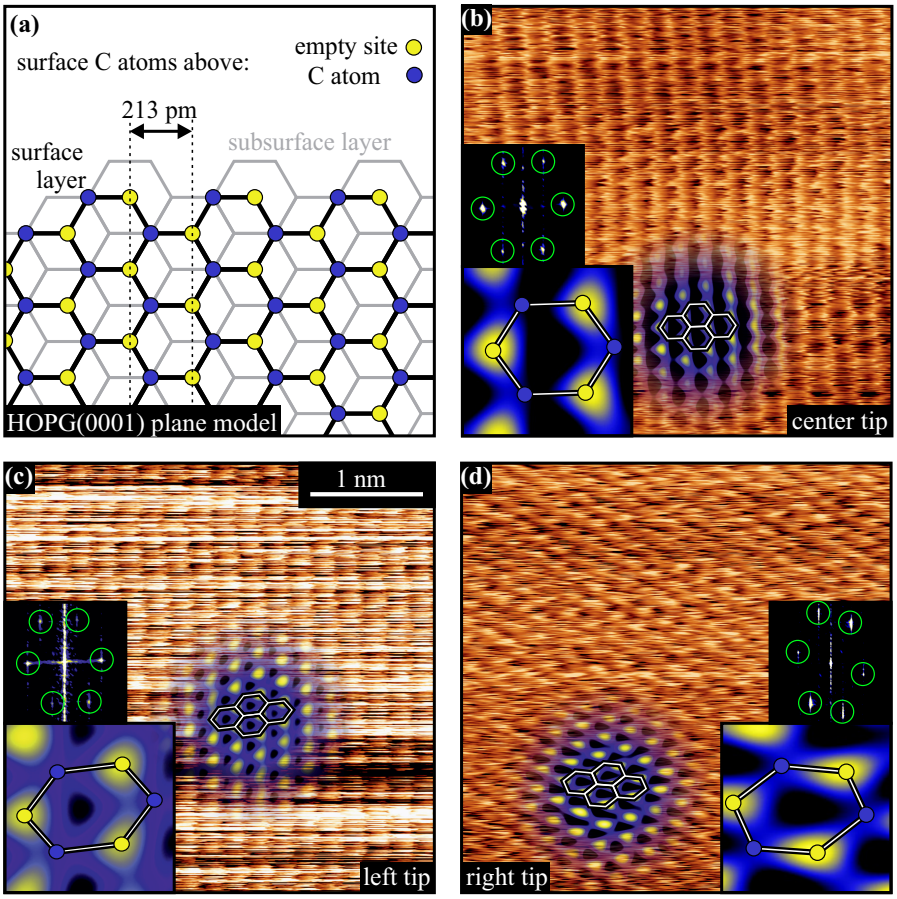

Figure 4.1: Calibration of the lateral displacement of the tube scanners. **(a):** HOPG lattice model with blue and yellow dots as carbon atoms of the surface layer and 213 pm as distance between the lines of yellow sites. **(b-d):** Topographic STM image of the atomic lattice on freshly cleaved HOPG surfaces in ambient conditions. FFT-filtered topography is blended in via round inserts into the lattice, with the honeycomb marked in white. Small inserts: FFT of the images with green circles marking the periodic structures in k space. Big inserts: Zoom into the filtered topographic data with atom sites marked in blue and yellow. Scanning parameters: (b): $I_T = 5$nA, $U_{bias} = 2$mV, (c): $I_T = 3$nA, $U_{bias} = 100$mV. (d): $I_T = 9$nA, $U_{bias} = 7$mV; all in ambient conditions. This picture was created by P. Lindner in the framework of his doctoral thesis and is used here with his permission [21].

Freshly cleaved HOPG samples have been used to calibrate each of the three scanning units [21]. In the figures 4.1 (b), (c), and (d), topography images measured in constant-current mode with each scanning unit are shown. In each image, the triangular lattice is visible, even though the signal is overlaid with white vibrational noise and noise due to ad- and desorption of contaminants on the scanning tips. These noise sources manifest in horizontal stripes in the fast scan direction, but by limiting the dynamic range of the colour scale to an 80 pm amplitude, the visibility of the atomic lattice can be increased. This way, noise signals with an amplitude higher than 80 pm, which is above the corrugation of the atomic lattice, are

filtered out.
In the left-top insert in each picture, the fast Fourier transformation (FFT) of the images can be seen, showing the periodic structures of the topography in k space as average. The six bright spots marked with green circles correspond to the period of the atomic lattices. By filtering the noise outside the green circles and computing the inverse FFT, the atomic triangular lattices remain as dominant structures. These are blended as a yellow-blue lattice into the topography image. By comparing the literature data with the measured topographic images, the lateral calibration factor can be derived as $C_{xy} = \frac{b_{\text{lit.}}}{b_{\text{meas.}}}$.
It is important to notice that in the presence of thermal drift, only the fast scanning direction can be calibrated reliably. For the slow scanning direction, drift and creep effects have to be taken into account. Figure 4.1 shows the data used for the calibration in x-direction. During the measurement, the tip is moved fast in x-direction back and forth and moved slowly, line, per line in y-direction. To reliably calibrate the y-direction, the fast and slow scanning directions have to be switched, thus rotating the direction of the scanning lines by 90°. Due to the symmetric shape of the tube scanner, the calibration coefficient in y-direction deviates negligibly from the coefficient in x-direction. For this reason, and because the procedure is equivalent, the calibration in y-direction shall not be further discussed in the following. It is recommended to recalibrate the tube scanners when starting new experiments; especially when the tunnelling probes or the experimental environment are changed. For example, the piezoelectric properties are temperature-dependent and will be altered significantly when cooling to low temperatures.
For the calibration of the scanner's vertical displacement, the mono-atomic step edges on Au(111) were used, since this system features far smaller terraces than HOPG. The distance $b_{\text{lit.}}$ between the atomic layers in (111) direction is defined by the lattice constant $a = 408pm$ to be $b_{\text{lit.}} = \frac{a}{\sqrt{3}} = 235\text{pm}$ as seen in the model shown in figure 4.2(b). For the preparation of the Au(111) samples, they were annealed using a Bunsen burner. This way, contamination can be removed and the gold surface is healed. In figure 4.2(a), three images of multiple Au(111) terraces, measured by each scanning unit, are shown on the left side. The images are smaller, scanning only a short range into the slow scanning direction, and are tilt-corrected. This is done to minimise the effect of thermal drift in the vertical direction.

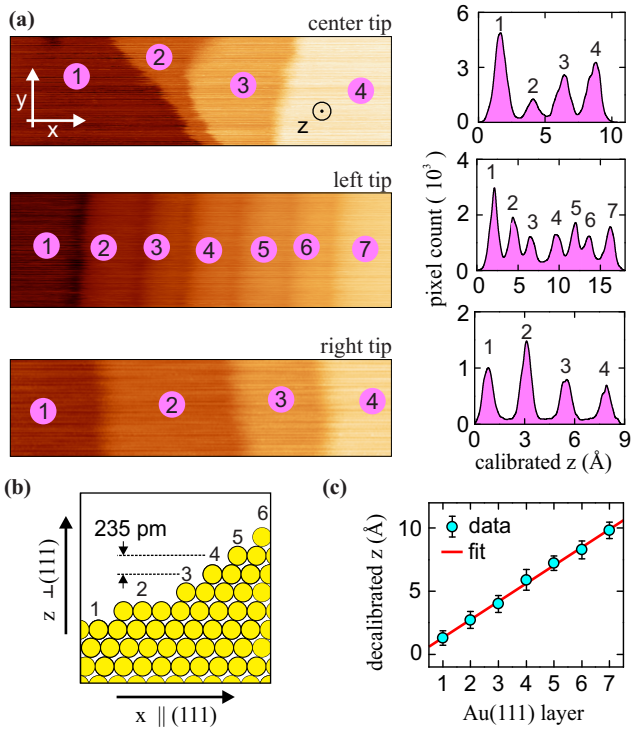

Figure 4.2: Tube scanner's calibration of vertical displacement using Au(111) step edges. **(a)** left side: STM topography images of Au(111) in ambient conditions measured with each scanning probe. The data is tilt-corrected, and the terraces are given indices. Right side: histograms showing the height distribution of the images on the left. **(b)** Model of the Au(111) lattice viewed from the side to show the step edges with 235 pm height. **(c)** Step height fit of the calibration procedure as described in the text for the left scanning unit. Scanning parameters: Centre tip: $I_T = 5$nA, $U_{bias} = -60$mV, Left tip: $I_T = 8$nA, $U_{bias} = -60$mV. Right tip: $I_T = 6$nA, $U_{bias} = -60$mV; all in ambient conditions. This picture was created by P. Lindner in the framework of his doctoral thesis and is used here with his permission [21].

To the right of the topographic images, the respective z histograms are shown, indicating the number of pixels on their vertical axis relative to their height value in z on their horizontal axis. Each of the individual peaks of the curves is fitted with the Gaussian distribution $f(z) \propto exp(-\frac{(z-z_0)^2}{2\sigma^2})$. There, z_0 is the z-value average of each peak, and σ is the standard deviation of the recorded data in each peak. The average and the standard deviation, determined this way, are then fitted to a linear function $f(x) = \mathrm{A} + bx$, which is weighted with the standard deviations (shown in fig. 4.2(c) for the left tip). The plot of the linear function shows the non-calibrated z value on the vertical axis relative to the number of the respective mono-atomic terrace on the horizontal axis. In the plot, A represents the height in z of the lowest mono-atomic terrace with the number 0, and the function's gradient should be the average step edge height, which can be compared to the literature value of $b_{lit} = 235$pm, yielding the calibration coefficient C_z.

The calibration coefficients for room temperature, determined as described above, are listed in table *i*. The scan ranges in lines two and four are determined by multiplying the calibration coefficients with the maximum voltage of 150 V delivered by the Nanonis electronics to the MP-STM's tube scanners. The values of the calibration coefficients differ between the respective scanners due to their different geometry.

	Left scanner	Centre Scanner	Right Scanner
C_{xy} (nm/V)	8.31	20.37	9.63
xy-range (μm)	2.46	6.11	2.89
C_z (nm/V)	1.92	1.44	2.68
z-range (nm)	288	216	402
C_{xy}/C_z (nm/v)	4.24	14.20	3.59

Table i: Room temperature calibration factors and scan ranges of the three scanning units.

4.2 Simultaneous operation

For the three scanning units of the MP-STM to operate simultaneously, the capability to maintain tunnelling contact and scan at the same time is important. Since a sample bias is applied to the sample stage in reference to a common ground potential in all the tunnelling probes, the scanning units should, in principle, not interact. In order to prove this hypothesis, we conducted simultaneous measurements with the three scanning units on HOPG. As mentioned above, this measurement was done during the second testing phase of the MP-STM prior to its installation into the UHV chamber system. In addition to testing the capability of simultaneous operation, the overall functionality of the microscope was also tested.
In figure 4.3, the three images of the HOPG surface measured with each scanning unit are depicted, with the topographic image in large, the current image in the top smaller insert, and the FFT of the topographic images as small inserts at the bottom left. Although the topographic signal is overlaid with noise from electrical and mechanical sources and ad- and desorption events, the atomic lattice is well observable in the images of the left and right scanning units (a and c) and faintly visible for the centre unit (b). However, it is better visible in the current maps, which are created by the current signal measured simultaneously with the z-signal of each scanning unit. The current image inserts are placed in overlap with the topographic images and show the area of the topographic image they are covering as the current signal. Furthermore, the FFT maps show the Bragg peaks, which are created by the periodic atomic lattice. These are clearly visible even for the image measured by the centre scanning unit.

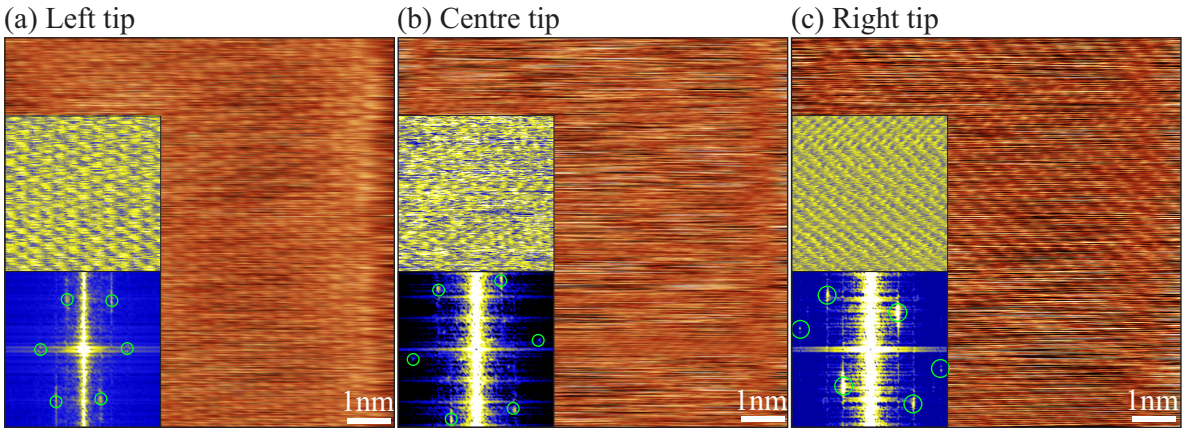

Figure 4.3: **(a-c):** Measurements done with all three scanning units simultaneously on HOPG in ambient conditions before installation into the UHV chamber system. The large images are the topographic maps of a 9 nm x 9 nm area on the HOPG measured with each unit. Although partially overlaid with noise and ad- and desorption events, the atomic lattice is observable in each map. Small inserts top: The current signal measured simultaneously to the topography at the position it is measured at. The atomic lattice can be observed better on the map created by the current signal. Small inserts bottom: FFT of the topography with green circles marking the Bragg peaks, which are created by the periodic structure of the HOPG's atomic lattice. **Scan parameters(a-c):** $I_T = 1\,\text{nA}$, $U_{bias} = 20\,\text{mV}$. (all tips): PtIr; all in ambient conditions.

For this measurement, the MP-STM was mounted onto the table described in section 3.7, which was screwed to the air-cushioned aluminium profile table of the UHV chamber system. The electrical contacts were connected according to the setup of the STM chamber. While this position of the MP-STM was ideal for assembly and cabling, it is non-ideal for STM measurements. Coupling of vibrational modes and no shielding from ambient radiation are limiting the signal-to-noise ratio. Nonetheless, the main objective of the test was achieved in demonstrating the capability of simultaneous tunnelling contact and imaging. Moreover, the signal-to-noise ratio was sufficient to detect the atomic lattice on HOPG.

4.3 Overlapping scan area

One of the key features of the MP-STM its ability to approach the tunnelling probes in close proximity. A way to prove this capability is to bring the scanning units into overlapping scan ranges. When in close proximity, the scanning units should partially be imaging the same sample surface area. By identifying distinct features on the sample, like defects or noticeable step edges, and comparing the topographic images of the centre and an approaching side tip, potential overlap of the scan ranges can be proven. The comparison of topographic images can also be used to approach the tips to each other in the first place. Since the optical resolution

of the LDM is close to the maximal scan range of the scanning units, an exclusively optical approach may be insufficient to achieve overlapping scan ranges. This is especially the case when operating the MP-STM at low temperatures because the piezoelectric effect of the tube scanners is temperature-dependent. When approaching by comparing topographic images, the side tips are approached step-wise towards the centre tip while imaging the sample's topography. These topographic images are compared with the whole scan range of the centre scanning unit. This is done until topographic features can be identified within the scan range of both scanning units. Once the scan ranges are overlapping, the geometric configurations of the tunnelling junctions in three-tip experiments can be controlled precisely.
For the attempt to approach the centre tip with the right tip into overlapping scan ranges, the vibration damping, radiation shielding, and electronics of the ambient setup were optimized. For overlapping scan ranges, the capability to detect distinct features on a sample is clearly needed, which requires improved tunnelling conditions. This was done by positioning the MP-STM on rubber damping feet closer to the centre of the UHV chamber's damping table, by covering the microscope with a radiation shield, and by detecting and removing ground loops in the peripheral cabling. Figures 4.4(a) and (b) show 3 nm x 3 nm topographic images of the atomic lattice of HOPG measured with the centre and the right tip. The images show an improved signal-to-noise ratio in comparison to the measurements presented above in section 4.2. The inserts on the bottom left of each image show the FFT of the topographic image, with the Bragg peaks of the atomic grid well identifiable.

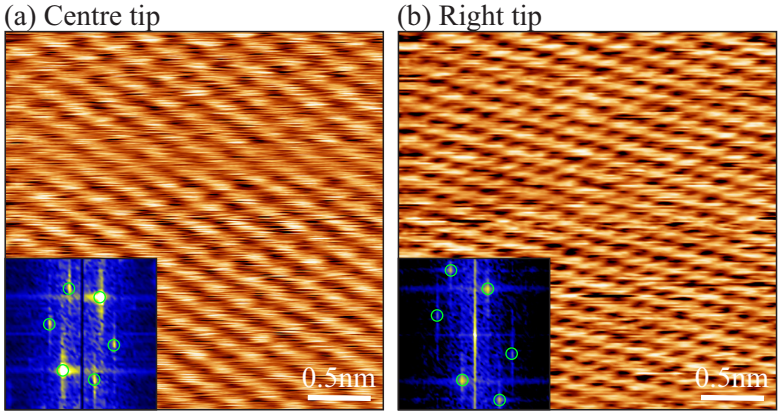

Figure 4.4: Topographic images of HOPG measured with (a) the centre tip and (b) the right tip in ambient conditions after optimizing the tunnelling conditions of the MP-STM. The atomic lattice is well identifiable, and the signal-to-noise ratio is greatly increased in comparison to the images shown in figure 4.3 in section 4.2. The small inserts show the FFTs of the topographic images, with Braggs peaks of the atomic grid well observable. **Scan parameters: (a):** $I_T = 4$ nA, $U_{bias} = 10$ mV, Cr coated W tip; **(b):** $I_T = 4$ nA, $U_{bias} = 500$ mV(b): PtIr tip; all in ambient conditions.

As described above in section 3.5, the scan range of the centre scanning unit is well observable with the LDM at room temperature. This allowed us to approach the right tunnelling tip into the centre tip's scan range by exclusively optical means. While doing so, the centre tip was held at a maximal lateral distance from the right scanning unit, in negative x-direction, to avoid mechanical contact between the tips.

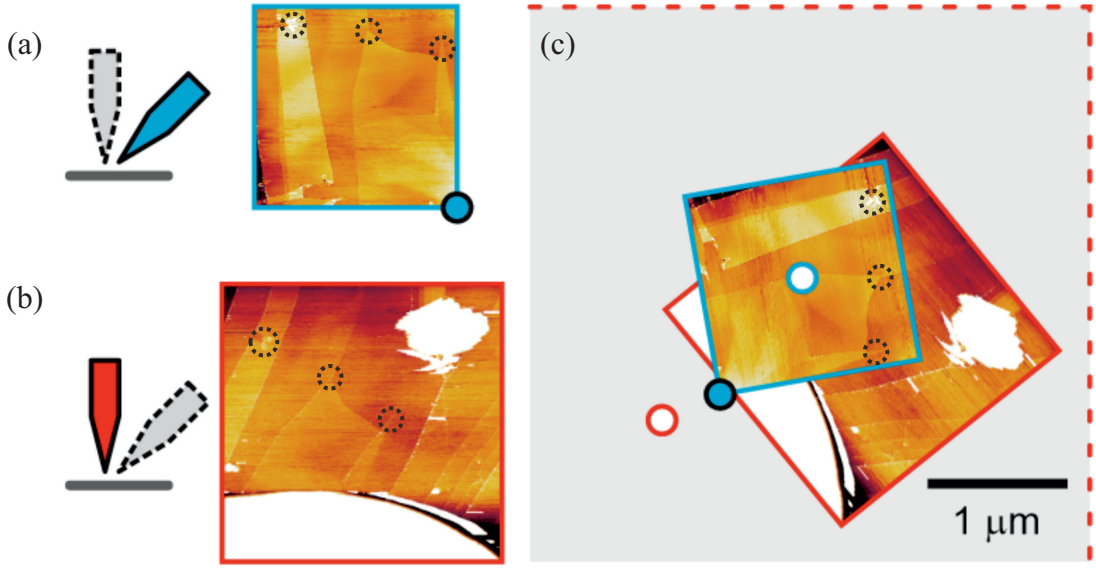

Figure 4.5: Topography scans of the right **(a)** and the centre tip **(b)** with overlapping scan ranges. The right tip was scanning over its whole scan range first, which is shown in light blue. Subsequent to the scan, it was parked at the position of the blue dot, retracted by about 300 nm. The centre tip was scanning the same area after that. In **(c)** both images are laid over each other, marking the three distinct features the area can be recognized by (black circles in each picture). These are a folded HOPG flake, an y-shaped step edge, and a triangular flake extending over two terraces. The centres of both scan ranges are illustrated as white dots, with the contour in the colour of the respective scans. In **(b)**, the whole topographic image of the centre tip is shown. There, the right tip seems to be imaged at the image's bottom. For both pictures, the same scanning parameters were used: $I_T = 50\,\text{pA}$, $U_{bias} = 500\,\text{mV}$. Right tip (a): PtIr; Centre tip (b): Cr-coated W; all in ambient conditions.

With the right tip being in close proximity to the centre tip, which was judged by LDM images, a topographic image with the full scan range was done. It is shown in figure 4.5(a). In the image, three distinct features on the HOPG surface can be perceived: a folded HOPG flake on the top left, an y-shaped step edge, and a triangle-like flake extended over a step edge on the top right. The right scanning unit's range is illustrated by the light blue square. In image (c), to the right of image (a), a larger image is showing the right scanning unit's range relative to the centre scanning unit's range, which is marked as a red dotted line. The centres of both scan ranges are marked by white dots contoured in their respective colours.

For clarification, the three distinct features on the HOPG surface are marked by black dotted circles in each of the three images.
Subsequent to the scan, the right tip was retracted by about 300 nm away from the sample and parked on the bottom right of its scan range, which is marked by the blue dot. Then, a larger area, comprising the area scanned with the right tip, was imaged with the centre scanning unit starting from the top and proceeding downwards towards the parking position of the right tip. The topographic image is shown in figure 4.5(b). There, the same three distinct features are observable. This allows to determine the relative locations of both scans and to arrange them accordingly, as shown in the image (c) to the right. In the bottom part of image (b), the centre scanning unit is seemingly imaging a large structure with a height of about 140 nm, which was not present before in the topographic image of the right scanning unit. Apparently the centre tip is interacting with the retracted and parked right tip, imaging a convolution of a tunnelling contact to the HOPG surface and a tunnelling contact in between the tips.
With the centre tunnelling tip getting into interaction with the right tip and imaging it partially, the objective of the experiment was achieved. The right tip was successfully approached in close proximity to the centre tip, and both were imaging overlapping scan areas. Furthermore, in figure 4.5(c), the scan range centres are close to each other, with a distance of less than 1.5 μm in between. This indicates that the tunnelling tips can be positioned into overlapping scan areas at low temperatures too. Then the scan ranges are decreasing, but the scan range centres can be brought sufficiently close to each other.

Chapter 5

Ultra-sharp single crystalline chromium tunnelling tips

As discussed above in section 3.1, the geometry of the tunnelling tips in multi-probe applications is crucial to the minimal achievable distance in between the tunnelling tips. To achieve tip-to-tip distances on the nm scale, ultra-sharp tips are deployed as tunnelling probes. Characteristics of such ultra-sharp tips are the small opening angle ϕ below 25° and a tip radius r below 30 nm. The electrochemical etching of tunnelling tips for conventional STM is well established, but the tips produced this way have tip radii typically larger than 100 nm. The creation of ultra-sharp tips via electrochemical etching is more complicated. Such tunnelling tips made of tungsten or a platinum iridium alloy (PtIr) can be purchased from companies like NaugaNeedles LLC, where tips with opening angles ϕ of a few degrees and apex radii r of 10 nm to 30 nm are offered [61]. However, this option is rather costly, with about 100 Euro per tip. Tungsten wire with 99.95 % purity is cheaper, with prices less than 10 Euro per meter (depending on the producer and quantity purchased [62, 63, 64]).
In order to have a home-made option, we developed a method to prepare ultra-sharp tungsten tips by combining the results of previous studies on tip etching methods [65, 66, 67, 23]. To this end, a thin tungsten wire of 250 μm diameter is etched in a potassium hydroxide solution (KOH) in two steps. A voltage is applied between the tip as anode and a cathode in solution, which is activating the chemical reaction. First, the wire is pre-etched to narrow it towards the apex, resulting in a smoother gradient towards the apex and therefore a smaller opening angle. During etching, a pulse generator is supplies the electrodes with pulses of 1 ms width with a 100 ms pause in between. The tungsten is reacting with the hydroxide ions (OH^-) to water and tungstate anions (WO_4^{2-}), which form a viscous flow down along the wire and decrease the activity of the OH^- ions. By applying a pulsed voltage with a 100 ms pause,

the WO_4^{2-} can dissipate in the solution, resulting in a more uniform OH^- ion activity along the wire and a more uniform etching [66].
In the second step, the pre-etched wire is moved up and down by a step motor, parallel to the tungsten wire. This way, the electrolyte is distributed more uniformly, preventing local concentrations, which can result in the formation of multiple etching menisci. This undesirable effect can occur during static etching and is not following a specific pattern, which makes it hard to control [67]. By moving the tip vertically, the electrolyte solution etches the tip more uniformly, which results in a smooth and controllable tip shape and opening angle. When the etched meniscus is thin enough, the remaining wire below the meniscus breaks off since the material becomes too thin to support it. The part breaking off is called a drop-off, and based on its size, the opening angle and the apex radius of the etched tip can be controlled. By choosing a large and therefore relatively heavy drop-off, the meniscus is pulled down and stretched thin, resulting in a small opening angle and a small apex radius. If successful, an ultra-sharp tip is etched this way. However, in the case of a drop-off that is too large, it can break off, leaving behind a large tip with a big radius.
Furthermore, when the drop-off is falling down, the reaction is still ongoing, and the remaining ultra-sharp tip is etched blunt. Therefore, a cut-off circuit is implemented that monitors the etching current and is sensitive to slight changes that occur when the drop-off is separated from the rest of the wire. In the event of separation, the cut-off circuit shuts down the voltage, ending the etching reaction. Thus, the opening angle and the apex radius are not only dependent on the weight of the drop-off and on the tip's vertical oscillation during etching but also on the response time of the cut-off circuit. The cut-off circuit used by S. Tunze is responding with a time period of 264 ns. More details about it can be found in [23]. By using this method, tungsten tips were etched successfully and reproducibly, featuring opening angles of (17±10) ° and apex radii of (12±8) nm. These dimensions were measured with a scanning electron microscope (SEM). The tips are well suited for deployment in three-probe STM experiments. However, for the investigation of magnetic nanostructures using spin-polarized STM (SP-STM), tungsten is not an appropriate tip material since it is not magnetic. By using a ferromagnetic or antiferromagnetic tunnelling tip material, magnetic surface properties can be investigated. Due to the tunnelling magnetoresistance (TMR), the tunnelling current flowing between a spin-polarized tip and a magnetic sample is sensitive to the enclosed angle of the magnetic moments of the tip and sample surface [25, 16]. A suitable and favourable tip material is antiferromagnetic chromium. Since the net magnetisation of chromium is zero, it emits no stray field, thereby avoiding perturbations of the magnetic textures of samples. Furthermore, Cr-tips are not susceptible to external magnetic fields. This is a useful characteristic when investigating the interaction between magnetic structures and

an external magnetic field. Chromium is also a very robust material that forms a thin oxide layer in ambient atmosphere, making it very stable on the one hand, while on the other hand, the oxide layer is easy to remove in UHV conditions, e.g., by applying bias voltage pulses between the sample and tip. It is known that Cr bulk tips allow for atomic resolution, which was proven on the Si(111) 7x7 surface [68], and are found to be sensitive to in-plane as well as to out-of-plane components of the magnetization, which was proven on monolayers (ML) and double layers (DL) of Fe/W(110) [69].
In continuation of the development of home-made tips, we developed the etching of ultra-sharp chromium tips. In the following, the process of etching a single crystalline ultra-sharp chromium tip, cut out of a Cr single crystal, will be shown.

5.1 Electrochemical etching of ultra-sharp tunnelling tips

In general, chromium is electrochemically etched in hydrochloric acid (HCl). The voltage is applied between a chromium cylinder and an electrode inside the acid solution, as shown in figure 5.1. The process of electrochemical etching in HCl is a redox reaction, where the chromium is oxidised and resolved. At the cathode, electrons are reacting with hydronium ions and protons to form hydrogen and water:

$$\begin{aligned} 2H_3O^+ + e^- &\leftrightarrow H_2 + H_2O \\ H^+ + e^- &\leftrightarrow H_2 \end{aligned} \tag{5.1}$$

At the chromium cylinder, which is the anode, the reaction is happening in two steps. First, water molecules diffuse through the oxide layer and react with the chromium. By giving up electrons into the circuit, the two components react chromium oxide and protons, which are diffusing back into the solution. Secondly, the chromium oxide is reacting with water to from chromium acid, which is dissolved in the solution:

$$\begin{aligned} Cr + H_2O &\leftrightarrow CrO_3 + 6H^+ + 6e^- \\ CrO_3 + H_2O &\leftrightarrow H_2CrO_4 \end{aligned} \tag{5.2}$$

The protons from the first reaction step are either reacting with water into hydronium ions or are reaching the cathode. There, the protons and hydronium ions are again reacting to form water and hydrogen.

In the past, one main problem with etching chromium wires was presumably their grainy microscopic structure, which prevented uniform etching and a smooth ending towards the tip shaft, resulting in non-uniform opening angles. To solve this issue, we tested the use of

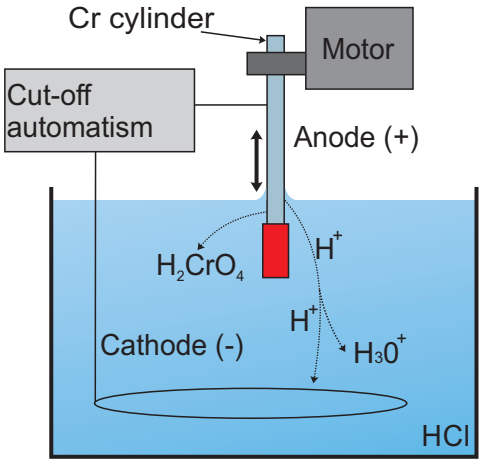

Figure 5.1: Setup for electrochemical etching of a chromium rod in the last etching step. The chromium rod is etched in a HCl solution and is vertically oscillated by a step motor. Once the drop-off, which is covered with insulating nail polish, is breaking away, the reaction is stopped by the cut-off circuit.

single-crystalline chromium. For this purpose, a 1 mm thick cylindric single crystal is cut into stripes using a diamond saw, which are filed down into cylinders with an approximate diameter of 1 mm. The subsequent stepwise etching process is schematically shown in figure 5.2(a).

At first, about three-quarters of the cylinder is pre-etched in the hydrochloric acid with a concentration of $5\frac{\text{mol}}{\text{L}}$ to narrow down the tip, thus creating a smoother gradient towards the apex that allows for a small opening angle. Then the remaining previously unetched part is etched down to a diameter of 0.25 mm in the same solution to fit it into the SMPS connectors that are the tip sockets (see section 3.1). For the last step, the apex of the pre-etched cylinder is covered with nail polish as an insulating material. In contrast to tungsten, which is etched much quicker at the meniscus close to the solution's surface in comparison to the tungsten in solution, chromium is etched more evenly in hydrochloric acid. This would result in the drop-off being dissolved before it could break off. Therefore, it is covered by an insulating material that prevents the etching of the drop-off. The etching in the final step of the process is similar to the etching method of tungsten wires, except that it is done in hydrochloric acid with a concentration of $1\frac{\text{mol}}{\text{L}}$. In figure 5.1, the step motor and the cut-off circuit are illustrated. The cylinder is driven by the motor in a vertical oscillation with an amplitude of about 2 mm, resulting in a smooth and controllable tip shape and a small opening angle. During the drop-off phase, the cut-off circuit shuts down the voltage in a time period of 264 ns, ending the redox reaction.

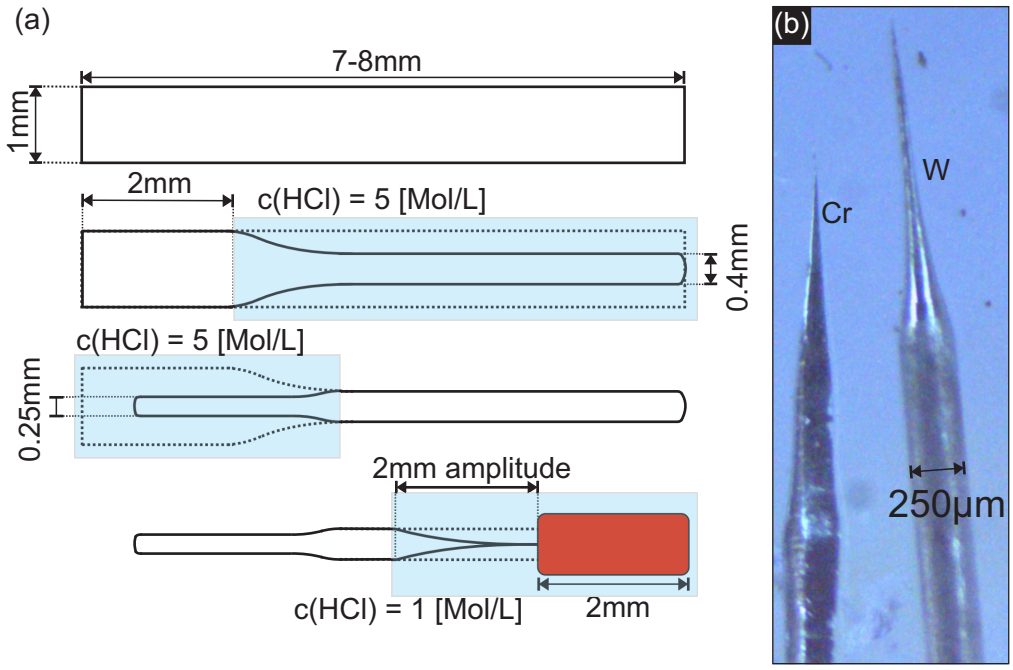

Figure 5.2: (a) Stepwise etching of a chromium tip, starting with a rod, cut out of a single crystal. The pre-etching is done in a $5\frac{\text{mol}}{\text{L}}$ HCl acid solution, and the last step is done in a $1\frac{\text{mol}}{\text{L}}$ solution. There, the micro-tip is formed by utilizing the 2 mm vertical up-and-down motion and the insulated drop-off. (b) The resulting Cr tip, imaged by an optical microscope, compared to a W-tip etched with the established recipe [23]. For size comparison, the diameter of the W wire is marked.

The result is shown in figure 5.2(b), as obtained with an optical microscope. There, the chromium tip is positioned next to a tungsten tip with a base radius of $250\mu m$ for comparison. The tungsten tip was etched according to the method developed in [23]. Both tips have a very sharp macroscopic opening angle and a tip apex that is smaller than the microscope's spatial resolution. The tips can be compared qualitatively. The chromium tip features no granular flakes and its similarity to the tungsten tip indicates the success of etching an ultra-sharp single crystalline chromium tip. To further optimize the method, further trials and quality checks with a SEM are needed.

5.2 Spin-resolved imaging with an ultra-sharp single-crystalline Cr tip

The single crystalline chromium tip's performance for imaging magnetic nanostructures can be tested. For this, the iron double-layer (Fe DL) on Ir(111) was utilized, which hosts magnetic spin spirals at low temperatures. Fe multilayer systems on Ir(111) have previously been studied intensively[70, 5, 71, 72]. While the Fe mono-layer is growing pseudomorphically on the Ir(111), the second layer exhibits dislocation lines resulting from uniaxial strain relief due to the large lattice mismatch between Fe and Ir(111). These dislocation lines are influencing the magnetic states of the Fe double-layer, resulting in spin spiral formation at temperatures up to 200 K [71, 72]. The spin spirals cannot be influenced by an external magnetic field of up to 3 T. This gives the opportunity to test the magnetic sensitivity of the chromium tip.
The single crystal chromium tip was tested in the UHV chamber system, described in chapter 2, since it allows for low temperatures and the application of an external magnetic field in z-direction. Since the development of the electrochemical etching method for single crystalline chromium tips was done during the testing phase of the MP-STM, another STM was installed into the UHV chamber system, which was used for testing the tips. It is the RF-SP-STM, which was designed and constructed by J. Friedlein [1]. Both the chromium tip and an Ir(111) sample were inserted into the chamber system and prepared for the experiment. The Ir(111) was cleaned by annealing in an oxygen atmosphere at 1200 °C for 40 minutes, sputtering with Ar^+ ions for one hour at room temperature, and by annealing in UHV at 1400 °C for 5 minutes to heal the crystal's surface. The tip was prepared by tunnelling into the clean Ir(111) crystal and pulsing with ± 10 V pulses between the tip and sample to remove the topmost chromium oxide layer. Subsequent to these preparation steps, 2.5 monolayers of Fe were deposited onto the clean Ir(111) surface by molecular beam epitaxy at elevated temperatures of approximately 150 °C.
In figure 5.3(a), a 200 nm x 200 nm overview topography image is depicted, which was measured in constant height mode. There, several terraces of varying Fe layer heights are visible. ML and TL are short forms for mono-layer and triple-layer. All layers with higher coverings are marked with numbers of the amount of monolayers deposited.
Below the overview STM image in figure 5.3(a), a spin-resolved dI/dU image of the large Fe DL terrace, which is marked by the white dotted line in the overview image, is depicted. There, the dislocation lines can be identified as pairs of lines arising with a period of $4(\pm 0.7)$ nm.

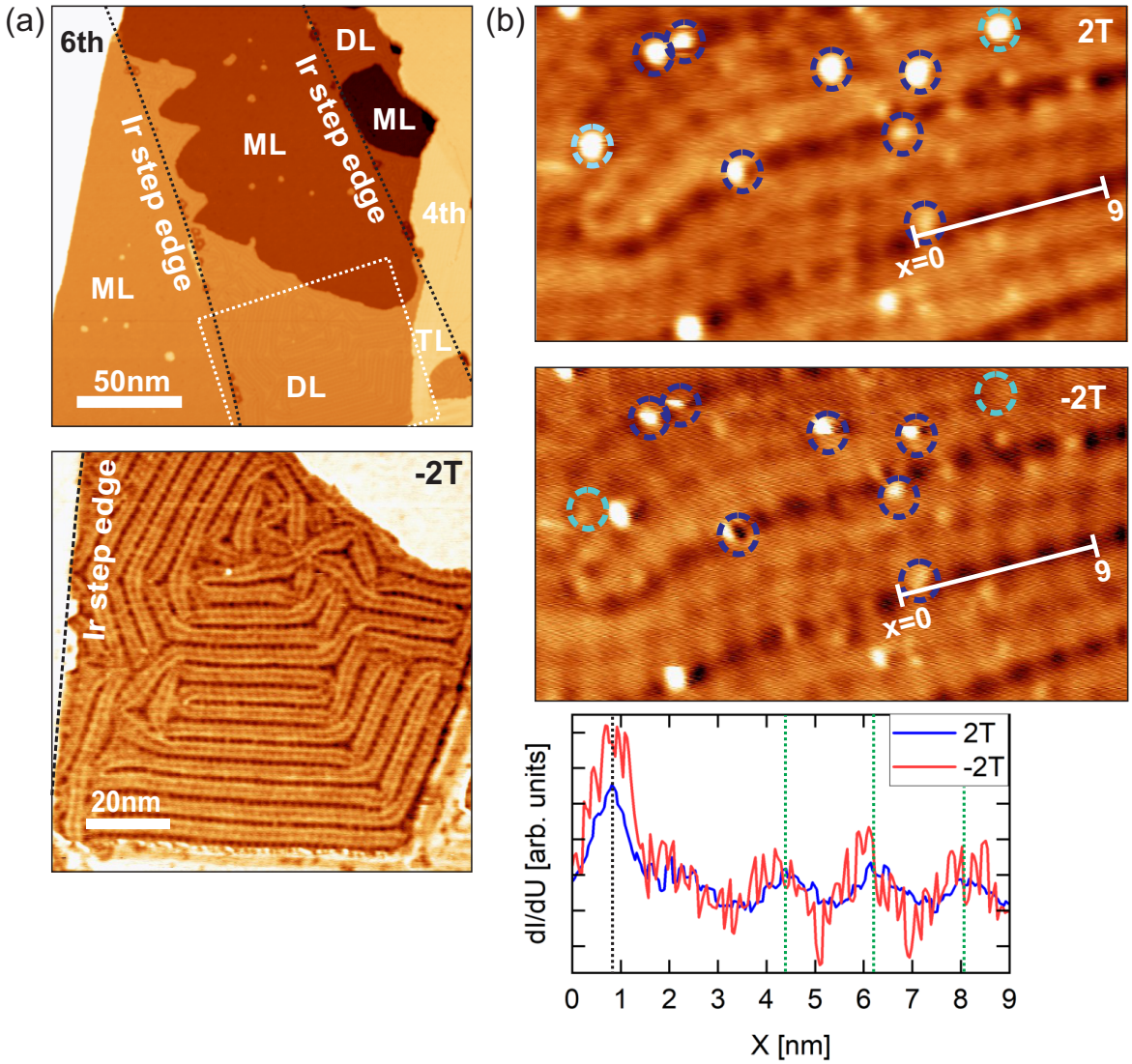

Figure 5.3: Images of the Fe on Ir(111) sample showing the spin spirals on the Fe DL. **(a) top:** Topographic overview scan in constant-current mode showing various terraces of different Fe layer height. **(a) bottom:** Spin-resolved dI/dU image of the large Fe DL, which is marked by the white dotted line in the overview image, obtained in constant height mode. The characteristic dislocation lines, paired lines with a period of $4(\pm 0.7)$ nm, and the spin spirals, which are propagating as alternating signals along the dislocation lines, are observable. **(b):** Close-up spin-resolved dI/dU scans of another DL terrace showing spin spirals in the presence of magnetic flux densities in z-direction of 2 T (top image) and -2 T (middle image). This particular terrace was chosen because it features impurity atoms, which can be used to compare the spin spiral positions of both scans. Those atoms are partially mobile on the surface. The atoms that clearly changed their position are marked in light blue, and those that remained at least partially in place and can be used for positioning are marked in dark blue. **(b) bottom:** Line scans indicated with white lines in the images above. The maxima of a fixed impurity atom (black dotted line) and the maxima of the spin spirals (green dotted lines) are compared. **Scanning parameters: (a) both**: U_{bias}=200 mV, I_{T}=0.8 nA, T=4.5 K, B=-2T. **(b)**: U_{bias}=200 mV, I_{T}=0.5 nA, T=4.5 K, B(top image)=2T, B(bottom image)=-2T.

The alternating signal, which is propagating along the dislocation lines, is caused by the spin spirals of the Fe DL. The imaging of the spin spiral is proving the tip's sensitivity to magnetic textures of the sample surface.
Magnetic contrast can also be achieved when a Fe cluster on the sample surface is picked up by a non-magnetic tunnelling tip. This was done for investigating the Fe DL on Ir(111) in [71, 72]. In contrast to a spin-polarized chromium tip, a Fe cluster is, however, aligning with the external magnetic field. Chromium is not susceptible to an external magnetic field due to its net zero magnetisation. The spin spirals formed by the Fe DL dislocation lines are found not to be influenced by external magnetic fields as well. Thus, by inverting the external magnetic field applied to the sample, one can test whether the tunnelling tip's magnetic sensitivity is caused by a spin-polarized Fe cluster or by the spin-polarized chromium tip.
To test this, a patch of a Fe DL terrace was imaged twice in the presence of an external magnetic field, first at 2 T and then inverted to -2 T. The corresponding dI/dU images are depicted in figure 5.3(b). According to D. L. Peng *et al.*, the coercivity value of Fe clusters is approximately 4.5 mT [73], which is small enough to achieve a complete polarisation inversion upon changing the external magnetic field from 2 T to -2 T. Therefore, the magnetic moments of an Fe cluster should align with the external magnetic field, and the image of the spin spiral should be inverted. In the case of a spin-polarized chromium tip, the spin spiral in both images should remain unchanged.
The spin spirals are compared along the white line, which is illustrated in both images of 5.3(b). The dI/dU signals of both lines are plotted against position (x [nm]) in the plot below. The red line is referring to the lower image measured at -2 T external field, and the blue line is referring to the image above measured at 2 T. The first large peak in each graph at $x \approx 0.9$ nm, which is marked with the black dotted line, is caused by the impurity atom marked in dark blue on the left side of both lines. From there, the maxima of both spirals can be compared. Although the signal in the image measured at -2 T is overlaid with a noise oscillation, the maxima of the red graph, which are marked by the green dotted lines, can be identified. The positions of the local maxima in the blue and red graphs are about the same, as indicated by the green lines. The fact that the maxima are not perfectly aligned may be due to the reduced signal-to-noise ratio in the lower image at -2 T, or to the impurity atom at $x \approx 0.9$ nm having moved slightly. An inversion of the spin spiral, however, can be excluded, which proves the absence of a Fe cluster at the Cr-tip apex.

In conclusion, the etched single crystal chromium tip shows sensitivity to magnetic textures of sample surfaces. A magnetic contrast due to a Fe cluster can be excluded. The single-crystal ultra-sharp Cr-tip is functioning just as well for SP-STM as formerly utilized bulk chromium tips prepared by different methods. This is an important milestone towards three probe experiments in combination with SP-STM.

Chapter 6

Lateral current application

One of the key features of the MP-STM is the capability of applying lateral currents in variable directions to a sample while the centre tunnelling probe is in tunnelling contact. This is done by utilizing the side probes as electric contacts in close proximity to the centre probe. Due to the small distances, high current densities can be applied very locally on the sample surface, despite applying low total currents to the contact tips. Furthermore, the current path direction can be easily changed due to the tip's mobility on the sample.
This opens up the possibility of conducting electronic transport and spin transport measurements that have previously been unattainable. To induce motion in atomic scale skyrmions, which is a key ambition of this project, experimental and theoretical studies suggest the existence of a current density threshold between $10^{10}\,\frac{\mathrm{A}}{\mathrm{m}^2}$ and $10^{11}\,\frac{\mathrm{A}}{\mathrm{m}^2}$ [9, 10, 11, 12]. It is, however, not the geometric prerequisites alone that can be an obstacle to such experiments. The feasibility of the application of such high current densities is also dependent on the following questions:

- What are the determining factors in the current density, magnitude, and distribution?
- How does an external magnetic field affect the lateral current?
- In what magnitude do side effects, such as Joule heating, influence the experiments?
- Can the threshold of $10^{10}\,\frac{\mathrm{A}}{\mathrm{m}^2}$ be reached within the experimental constraints of the MP-STM without harming the sample integrity?

In order to answer these questions, lateral current experiments on $NbSe_2$ and Ir(111) will be discussed, which were aimed at testing the limitations on the lateral current on different sample systems and the current's effect on the charge density wave (CDW), which can be observed in $NbSe_2$ at temperatures below 34 K [74].

Furthermore, a simulation study will be presented that was done utilizing the COMSOL Multiphysics® software. The simulation study is aimed at investigating the distribution of lateral currents in samples, their interaction with external magnetic fields, and the effects of Joule heating in further detail.

6.1 Lateral current experiments

The lateral current experiments, presented in the following, were conducted during the first testing phase of the MP-STM while it was installed in the UHV testing chamber described in [42]. For these, tips made of pulled PtIr wire were used as STM tips for the side scanning units, while an ultra-sharp PtIr tip from Nauga Needles LLC was used as centre STM tip. The tips were approached by optical means first to the sample and subsequently to each other. Due to the shape of the side unit's STM tips, they were positioned at a distance of 200 ($\pm$10) μm to each other. With all three tips in position, the side tips were carefully driven into the sample, and their position was fixed by the Nanonis control electronics. Subsequently their cables for tunnelling current were disconnected and connected to a current source with an electric potential floating relative to the bias voltage between centre tip and sample. This can be done by using batteries as a current source. When the circuit of the side tips is contacting the sample, the floating potential of the current source is adjusting to the applied bias voltage, resulting in a potential equalisation in form of a voltage peak. Therefore, the centre tip was retracted during the contact of the side tips with the sample. After the equalisation of potentials, no influence of the two circuits on each other was detected. The total current applied to the side tips can be controlled by using a potentiometer on the current source.

6.1.1 $NbSe_2$

The first substrate tested is the transition metal dichalcogenide $NbSe_2$. Similar to HOPG, it is also a layered system with Van-der-Waals interaction binding the layers together. An atomically flat surface can be easily prepared by cleaving. Its surface features a trigonal atomic lattice with a lattice constant of 3.5 Å. At temperatures below 34 K $NbSe_2$ develops a 3 x 3 charge density wave (CDW) on its surface [74]. $NbSe_2$ was chosen for these properties since it can be prepared in the UHV testing chamber, which lacked preparation equipment for ion-sputtering and annealing. Furthermore, the CDW was expected to be a potential indicator for effects of the lateral current on the electronic states on sample surfaces.

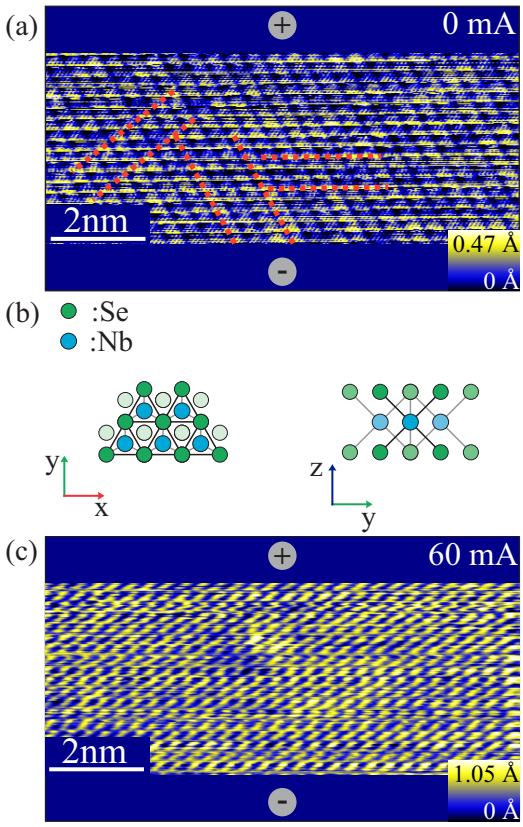

Figure 6.1: Topographic images of $NbSe_2$ at 0 mA **(a)** and 60 mA **(c)** applied lateral current. The symbols '+' and '-' are illustrating the direction of the left and right STM tips relative to the images and the direction of lateral current. In **(a)**, the atomic lattice can be observed as a triangular pattern and the CDW as an alternating signal intensity. The red dotted lines mark one wave period of the CDW. **(b)** shows a model of the atomic lattice of one layer of $NbSe_2$ as top view (xy-plane) and as sectional side view (yz-plane)[75, 74]. The image of **(c)** is distorted due to thermal drift, but the atomic lattice is observable as line pattern. **Sanning parameters:** PtIr tip, $U = -200$ mV, $I_t = 100$ pA, $T_{0mA} = 20$ K, $T_{60mA} = 28.6$ K (temperatures measured with temperature diode on sample holder).

During the experiment, the centre tip was imaging the topography of an area of 10 nm x 10 nm on the $NbSe_2$-surface, while the total current applied to the side tips was increased in discrete steps from 0 mA to 60 mA. The MP-STM was cooled by a He-flow cryostat and was in thermal equilibrium at 20 K in the beginning. By imaging the atomic grid and the CDW on the $NbSe_2$ surface for each step of increasing total current, the influence of the lateral current on the substrate, the CDW, and the tunnelling conditions was tested.

Figure 6.1(a) shows a topography image measured by the centre tip, while the side tips were in contact but no lateral current was applied. The direction of the contact tips relative to the topographic image is indicated by the '+' and '-' symbols. Consequently, the lateral current's direction is also indicated this way. The triangular pattern is observable in the topographic image. It is formed by the atomic lattice, which is shown as a model in figure 6.1(b) [75]. The model shows one layer of the $NbSe_2$ as top view in the xy-plane and as sectional side view in the yz-plane. The colour brightness is illustrating the distance to the position of view in the model, with the pale colours indicating atoms further away. The triangles of Se-atoms on the model's top layer with an Nb-atom beneath its centre are imaged in the topographic image as filled triangles. The triangles with a smaller z-signal are the triangles of the top Se atoms without a Nb atom in their centre.

The signal intensity of the pattern is alternating over a period of three atomic rows. In figure 6.1(a), the intensity maxima of one period length

are marked by red dotted lines parallel to the corresponding atomic row. This signal alternation is caused by the CDW due to its changing local density of electronic states. The imaged atomic lattice shows a lattice constant of (3.0±0.6)Å and a periodicity of the CDW of (9.0±1.7)Å, which is in agreement with the literature.
Figure 6.1(c) shows the topographic image of the $NbSe_2$, which was measured while a total lateral current of 60 mA was applied. The image is distorted, and the atomic lattice is observable as a line pattern showing the most dominant atomic rows. The CDW is not identifiable.

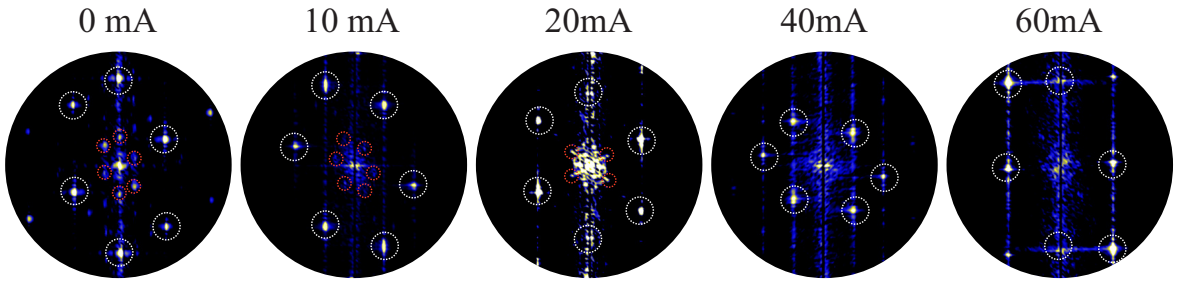

Figure 6.2: FFTs of the topographic images measured with the centre STM tip while a stepwise increased lateral current from 0 mA to 60 mA was applied to the sample. The intensity peaks marked by the white dotted rings are showing the period of the atomic lattice, while the peaks marked by the red dotted rings are showing the period of the CDW. The scan direction was rotated during some of the measurements, resulting in rotated intensity peaks. **Scanning parameters:** PtIr tip, U = -200 mV, I_t = 100 pA, T_{start} = 20 K.

While the atomic lattice is still observable in the topographic images measured during the application of lateral currents, the distortions complicate the identification of the CDW. Figure 6.2 shows the FFTs of topographic images at each step of lateral current increase. In the leftmost FFT, which is the transformation of the topographic image shown in figure 6.1(a), the periodic structures being the atomic lattice and the CDW result in the respective peaks of intensity. The peaks corresponding to the atomic lattice are marked by white dotted circles, and the peaks corresponding to the CDW are marked by red dotted circles.
With stepwise increasing the total current, the high-intensity peaks of the FFTs are increasingly stretched. This corresponds to the periodic structures in the topographic image being distorted, as discussed above regarding the topographic image shown in figure 6.1(c). The rotation of the FFT pattern in between measurements is caused by the fact that the scan direction was rotated for some measurements, which can help to counteract the effects of thermal drift.
A plausible cause for the distortion is thermal drift, which occurs due to a thermal imbalance between the sample and STM tip. The sample, being heated by the lateral current due to Joule heating, is moving relative to the STM tip due to its thermal expansion.

While the intensity peaks of the atomic grid remain well identifiable for topographic images with increasing total currents applied, the intensity peaks of the CDW are decreasing and start to vanish at currents of 40 mA and above.
This may also be explained by local current-induced heating of the sample. The lateral current may have deposited enough heat on the sample surface by Joule heating to surpass the transition temperature of 34 K.
If the hypothesis of temperature increase due to Joule heating is correct, a thermal expansion of the sample is to be expected. In this case, the distance between the sample and the tip is decreasing. This results in a retraction of the tip since the feedback loop of the centre scanner adjusts the tip-to-sample distance to stabilise the tunnelling current. Thus, an expansion of the sample is expected to be observable in the z-signal of the centre tube scanner.

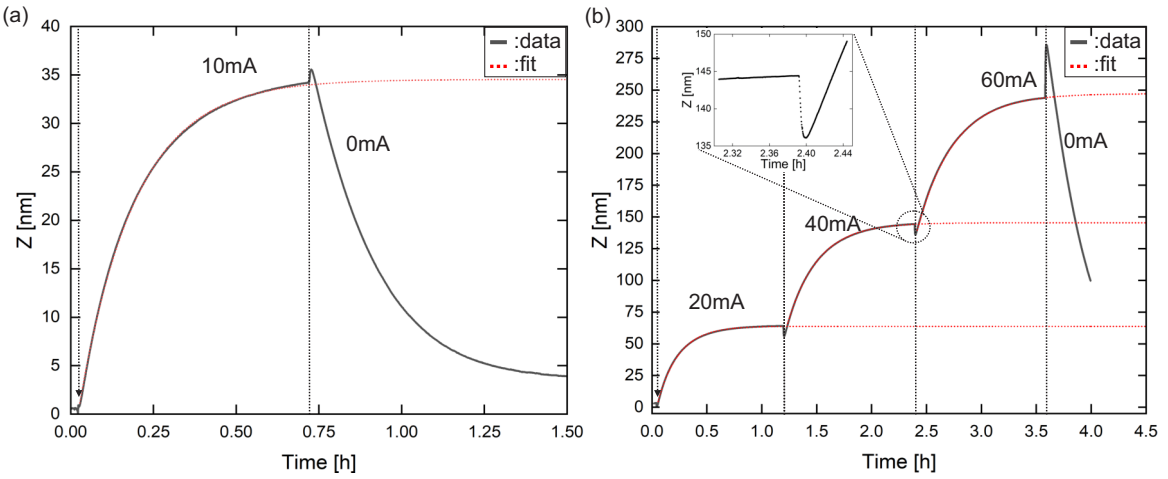

Figure 6.3: z-signal of the centre tube scanner plotted against time during the topographic imaging of the $NbSe_2$ sample, while the lateral current was increased stepwise. **(a)** shows the measurement during the application of 10 mA. **(b)** shows the z-signal during the current steps from 20 mA to 60 mA. The vertical black dotted lines mark the moments when the current was changed. The black dotted arrow marks the activation of the lateral current. The saturation level of the z-value for each current was fitted, which is marked by the red dotted lines. The insert shows a zoom into the rapid change in z upon changing the lateral current from 40 mA to 60 mA. **Scan parameters:** See figure 6.2

In previous experiments, the tunnelling tip of a STM was heated with a laser to create a thermal disbalance [76]. During the tip-expansion, the retraction of the tip was measured. The tip was retracting until a new thermal equilibrium was achieved, which is observable as a saturated z-value.
In our lateral current experiment and parallel to the measurement of topographic images, the z-signal of the centre STM tip was measured as well. This data is plotted in figure 6.3 against time. A lateral current of 10 mA resulted in a retraction of 34.5 nm as shown in the

plot 6.3(a). After the lateral current was deactivated, the tip was approaching its initial position again. In addition to the slow increase of z, a more rapid decrease during current activation and an increase during deactivation were observed.
Figure 6.3(b) shows the remaining steps of the increase of lateral current from 20 mA to 60 mA. The current was increased during this interval without deactivating it in between steps. For each current value, an individual saturation level in z is observed. During the activation and each step of increasing the current, the rapid decline of z is also observed. At the point of final current deactivation at $t = 3.6$ h, z is also rapidly increasing, like in (a), although it is greater in comparison to the previous slower increase. After deactivation, the tip is approaching its initial position again.
The curves may be explained by a thermal expansion during the application of current towards a saturated z-value, which is the distance the tip is retracted until the system reaches thermal equilibrium. With each step of increasing the lateral current, this equilibrium is at an increased local temperature on the sample. This leads to an individual saturation level in z for each current. After deactivation, the sample is cooling again and contracting. The tip is then approaching a position close to its initial position.

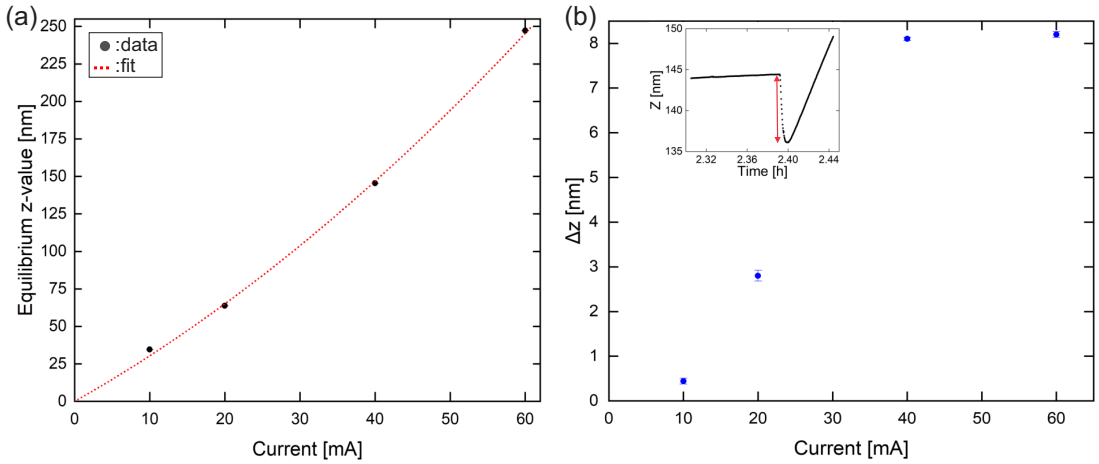

Figure 6.4: **(a)** Saturation levels of z in figure 6.3, which were determined by fitting, plotted against current. **(b):** Amplitudes of the rapid changes in z upon changing the applied lateral current. The insert shows the rapid change in z from figure 6.3(b) from 40 mA to 60 mA. The data points were determined by subtraction of the average z-value in the graphs local minimum and the average z-value directly before changing the current.

Figure 6.4(a) shows the saturation levels plotted against the total applied lateral current. Following the hypotheses of thermal expansion caused by Joule heating, a dependency of the saturation levels on the total applied lateral current is expected.

In a simplistic approach, the power P deposited in the sample by lateral current can be described by Joule's law:

$$P = R \cdot I^2, \tag{6.1}$$

where the sample's resistance R is constant and the current I is adjusted by the current source that is connected to the side tips in electrical contact with the sample. In this model, an ideal current source is assumed.
For the saturation levels in z, it is assumed that the sample is in thermal equilibrium with its surroundings and that its temperature is not changing. In this case, the power deposited by Joule heating is equal to the cooling power P_c of the sample in thermal contact with the system's cryostat. The latter is described by Fourier's law of thermal conduction:

$$P_c = k \cdot \frac{A \cdot (T_1 - T_2)}{L}, \tag{6.2}$$

where T_1 is the temperature of the sample, T_2 is the temperature of the cryostat, and k is the thermal conductivity of the connection. Furthermore, A is the cross-section area, and L is the length of the conducting connection. Therefore, under the assumption that all other parameters are constant, the temperature of the sample T_1 is quadratic dependent on I:

$$T_1 = I^2 \cdot \frac{R \cdot L}{k \cdot A} + T_2 \tag{6.3}$$

Assuming the sample is expanding uniformly in each direction proportionally to its temperature increase, this results in a thermal expansion of volume ΔV that is dependent on the change of temperatures in between the levels of thermal equilibrium for different total lateral currents:

$$\Delta V \approx V_0 \cdot \alpha \cdot \Delta T. \tag{6.4}$$

Here, V_0 is the initial volume, and α is the sample's expansion coefficient.
Thus, in order to fit the data points shown in figure 6.4(a), a quadratic dependency and the requirement that the sample is not expanding or shrinking when no current is applied ($z(0) = 0$) were assumed. For this the trial function $z(I) = a \cdot I + b \cdot I^2$ was used. This resulted in a fit with the parameters $a = (2.8 \pm 0.19)\frac{\mathrm{nm}}{\mathrm{A}}$ and $b = (0.021 \pm 0.0037)\frac{\mathrm{nm}}{\mathrm{A}^2}$. The fit shows a quadratic dependency and a more dominant linear dependency of the saturation levels z on the applied lateral current I. The linear part of the function may be explained by a linear thermal drift, which distorts the saturation levels. Since the sample is in thermal imbalance to the STM during the experiment a thermal drifting may cause an linear dependent offset for the saturation levels. Furthermore, the temperature dependence of parameters assumed

to be constant or a change in resistivity due to change of the mechanical contact of the tips with the sample may play a role.
Figure 6.4(b) shows the amplitudes Δz of each rapid decrease in z that occurred upon changing the applied lateral current plotted against current. These data points were determined by averaging the value of z in each step before changing the current and comparing it with the average of the z value at the minimum of the rapid decline. This was possible due to the great number of data points, with one data point per second, in comparison to the rate of change in z. The data points of $\Delta z(10\,\mathrm{mA})$ to $\Delta z(40\,\mathrm{mA})$ seem to follow a positive dependency on the lateral current, similar to the quadratic relation observable for the saturation levels. The data point $\Delta z(60\,\mathrm{mA})$, however, is of similar value to $\Delta z(40\,\mathrm{mA})$.
One possible explanation for the rapid changes in z may be a thermal expansion of the contact tips. Since the highest current density of the lateral current is in the contact of the tips with the sample, the highest increase in temperature can be expected there. This may lead to a thermal expansion of the side tips on a quicker time scale in comparison to the sample. The expanded tips may be pressing against the sample surface and moving it away from the centre tip, hence the decrease in z. Upon deactivation, the tips may cool quickly again due to their good thermal connection via the coaxial tip cabling, and the sample is no longer pressed away from the centre tip. Based on the model discussed above, this explanation of thermal expanse requires a quadratic relation between the points Δz and I. At least the data for 60 mA does not fit that model. However, since the contact tips would be pressing against the sample, a more complicated relation may be plausible. Deformation of the PtIr tips or a change in contact resistance may hinder an increase in Δz and lead to saturation at 60 mA.
While the information gained through the data is not sufficient to assess the exact interaction of the side tips with the sample or the exact increase in temperature on the sample, there is evidence for heat deposition due to Joule heating. The heating may benefit from the layered structure of the $NbSe_2$ and another material may show different behaviour. The anisotropic crystal structure of $NbSe_2$ causes the electrical and thermal conductivity to be direction-dependent. The electrical resistance in between layers confines the lateral current to the upper layers, which results in a pronounced current density and heat deposition due to Joule heating. Additionally, the reduced thermal conductivity between layers may cause an inefficient dissipation of heat. In isotropic crystal structures, the current may be spread more evenly, and the deposited heat may dissipate more efficiently, resulting in a lower increase in temperature.
Even though the sample was heated, the centre tip did not need to be retracted beyond the range of the centre tube scanner, and it was possible to image the atomic lattice of $NbSe_2$ during the whole experiment.

6.1.2 Ir(111)

The application of lateral currents to manipulate the motion of atomic-scale skyrmions on the Pd/Fe/Ir(111) system is one of the project's key ambitions. The second lateral current experiment is, therefore, aimed at investigating the effects of lateral current on the thin film system's substrate, Ir(111). In order to compare the substrate Ir(111) with $NbSe_2$ of the previous experiment, the same tip configuration was used with pulled PtIr side tips in contact and at a distance of 200 μm from each other and the centre tip in the centre between them.

In a series of three measurements, a lateral current of 10 mA, 15 mA, and 25 mA was applied via the side tips to the sample with the centre tip fixed in tunnelling contact in constant current mode, and the centre tube scanner's z-signal was recorded. In between each of the measurements, the lateral current is set to 0 mA for the substrate to relax into its initial state. Figure 6.5 shows on the left the z-signal of the centre tip plotted against time for each measurement run. The curves of the measurements with 15 mA and 25 mA are plotted with an offset to prevent overlapping of the curves.

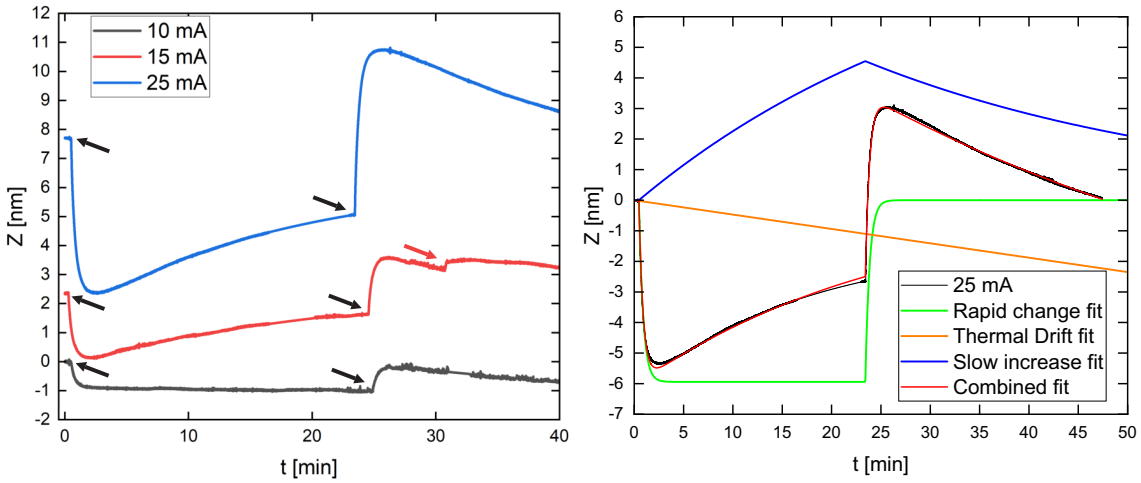

Figure 6.5: **Left:** The z-signal of the centre tip plotted against time for varying total lateral currents applied by the side tips. The activation and deactivation of the current can be identified easily by the sharp drop and the sharp increase in the z-signal. They are marked by black arrows. In between, the z-signal slowly increases and slowly decreases again after deactivating the current. In addition to these effects, a thermal drift is also present in each curve. During the slow decrease in the 15 mA curve, the z-signal changes rapidly once, which is marked by the red arrow. **Right:** For interpretation, each curve was fitted by a sum of limited exponential growth functions as trial functions and the thermal drift. **Sanning parameters:** PtIr tip, $U_{\text{bias}} = 80$ mV, $I_T = 2$ nA, $T_0 = 37.4$ K

In the plots, the direction of z is equal in meaning to the previous experiment, where the negative z-direction is directed towards the sample and the positive is directed away from it. Each curve starts with an initial value in z and features a rapid decrease in z upon activating the lateral current. For the runs with 15 mA and 25 mA total lateral current, the z value increases slowly after that towards a saturation level. Upon deactivating the current, the value of z is rapidly increasing again and then slowly approaching its initial value plus a thermal drift again. The moments of activation and deactivation of current are marked by black arrows in figure 6.5. The behaviour of the retraction and expansion of the tube scanner shows similarities to the previous experiment on $NbSe_2$. The rapid changes in z are happening on a smaller time scale in comparison to the changes in z afterwards before deactivating the current again. Furthermore, the more slower changes are also approaching a saturation value, which appears to be current-dependent.
On the other hand, the amplitudes of both types of changes in z are very different from the previous experiment. In contrast to the previous experiment, the total changes in z are below 10 nm and the rapid phase shows a larger amplitude than the slow phase. This may indicate a smaller increase in temperature in general and a far lower increase in temperature in the sample compared to the contact tips, given the previously discussed model of thermal expansion of the sample and side tips is correct.
The red curve of 15 mA is featuring a jump during the approach to the initial value. A likely reason for that is the drifting of the centre tip over a step edge of the Ir(111) surface. The signal change in figure 6.5 is marked by the red arrow.
Each of the curves was analysed by fitting it with a sum of limited exponential growth functions and thermal drift with the following trial function:

$$\begin{aligned} z(t) &= z_0 + t \cdot d \\ &+\Theta(t,0,1,t_{on}) \cdot \Theta(t,1,0,t_{off}) \cdot A_r(1 - e^{-\frac{t-t_{on}}{\tau_r}}) \\ &+\Theta(t,0,1,t_{off}) \cdot A_r(1 - e^{-\frac{t_{off}-t_{on}}{\tau_r}}) \cdot e^{-\frac{t-t_{off}}{\tau_r}} + \\ &+\Theta(t,0,1,t_{on}) \cdot \Theta(t,1,0,t_{off}) \cdot A_s(1 - e^{-\frac{t-t_{on}}{\tau_s}}) \\ &+\Theta(t,0,1,t_{off}) \cdot A_s(1 - e^{-\frac{t_{off}-t_{on}}{\tau_s}}) \cdot e^{-\frac{t-t_{off}}{\tau_s}}. \end{aligned} \tag{6.5}$$

Here, the initial z-value is z_0 and the thermal drift is assumed linear with the slope d. The heavy-side functions Θ are dividing the graph into regions of activated current [t_{on},t_{off}] and deactivated current $t > t_{off}$. In each region two limited exponential growth functions for rapid change in z (with indices r for rapid) and for slow change in z (with indices s for slow) were fitted. For each the parameters for amplitude A and for time constant τ were fitted.

In figure 6.5 on the right the fit for the 25 mA curve is divided into each part of the trial function. The rapid change in z is shown in green, the slow change in z is shown in blue, and the linear thermal drift is shown in orange. It was found that for intervals two and three, the same functions and parameters could be applied for each part. This enabled an analysis of the amplitude of each growth function.

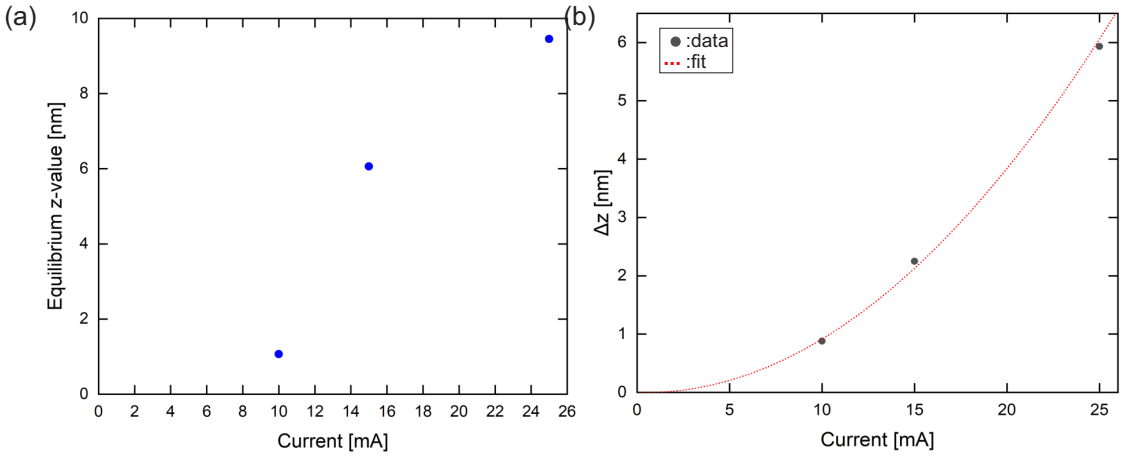

Figure 6.6: Amplitudes of the curves plotted in figure 6.5. **Left:** The saturation levels or amplitudes A_s of the slow increase in z during the application of currents. The data point for $I = 10\,\text{mA}$ did not converge unless its time constant was fixed as the average of the fit functions of the other curves. **Right:** Amplitudes A_r of the rapid changes in z upon activating and deactivating the lateral current.

Figure 6.6 shows the saturation levels of z for each step in I and the amplitudes of the rapid changes Δz upon changing the lateral current. On the left side, the amplitudes of the slow increase in z are plotted against applied current. Since the curve in figure 6.5 for 10 mA the curve is not rising after activation of current the fit for this data point did not converge on the first try. A reason for this may be that the rise in z caused by the lateral current is smaller than the decrease in z caused by thermal drift during the experiment, which was working in the opposite direction.

Since the growth functions that did converge show approximately equal time constants for different current values, a time constant for the non-converging function was fixed, which is the average of the constants gained from the other fits. This led to the convergence of the function, but the correctness of the value cannot be trusted. This may also explain why the data is not easy to fit into a model, and the functional relation between the saturation levels and the applied current can only be guessed.

For the amplitudes of the rapid changes in z, on the other hand, a model could be fitted since these functions did converge well. On the right hand side of figure 6.6, the data points are plotted against applied current and fitted by the same trial function as was used in the

$NbSe_2$ experiment. The following function resulted in:

$$z(I) = (0.01 \pm 6.210^{-4})\frac{\mathrm{nm}}{\mathrm{A}^2}I^2 - (0.01 \pm 0.01)\frac{\mathrm{nm}}{\mathrm{A}}I. \tag{6.6}$$

Here the z-signal is predominately quadratically dependent on the lateral current, which fits well into the model of thermal expansion discussed for the experiment with $NbSe_2$. In contrast to the former experiment, however, the linear dependency is less pronounced. This may be due to the deactivation of lateral current in between measurements that caused the system to relax into thermal equilibrium and lessen the effect of thermal drift in between measurements.

When comparing the data with the results of the lateral current experiment on $NbSe_2$, the contrast in amplitude of the changes in z-value stands out. If the hypothesis of an expanding sample due to Joule heating is correct, it can be assumed that the increase in temperature on the Ir(111) is considerably smaller.

By considering the comparatively small effect of the lateral current on $NbSe_2$ on the centre tip's z signal, a disturbance of tunnelling conditions while applying lateral currents to an Ir(111) surface is not to be expected. The very faint retracting of the centre tip during the application of 15 mA, and 25 mA is indicating that a local application of high current densities is not resulting in large heat deposition by Joule heating. The quick expanding upon activating the current and the quick retracting upon deactivating are more difficult to explain but may be due to the Joule heating of the contacting site tips.

6.2 Numerical simulations on 2-tip transport experiments

The observations of the lateral current experiments indicate the effects of strong lateral current on a sample and the tunnelling conditions of the centre tip, and the effects of Joule heating. However, the experiments do not provide indications on the current density achievable on the sample, nor is the tip configuration optimal since no ultra-sharp tips were used. In order to get a better understanding of the lateral current with other tip configurations and to assess the feasible current densities, the interaction of current with an external magnetic field, and the effects of Joule heating, numerical simulations were done.

With the contacting tips at macroscopic distances from each other, the current distribution can be calculated analytically. The contact areas of the tips with the sample are negligibly small in comparison to the distance from each other. Therefore, they can be approximated as point contacts. In order to apply high current densities without depositing much heat due to Joule heating, however, the contact tips need to be in ultimate proximity. This way, high current densities can be achieved by applying low total lateral currents. In this case, the geometry of the contact sites can no longer be assumed as points, and analytical calculations become incorrect. Also, the interaction of the currents with the conducting material, dependent on the material properties, deposition, and dispersion of heat, and the interaction with an external magnetic field are creating an even more complicated picture.

To simulate lateral currents, we created a model of a crystalline sample and two contacting side probes utilizing the COMSOL Multiphysics® software. The geometry of the side probes and the sample is simplified, which is shown in figure 6.7(a). The sample crystal is approximated as a quadratic plate with side length a and thickness t, and the side probes are approximated as cylinders with radii r and length l, with their bottom side in ideal ohmic contact with the sample. They are positioned at a distance of d from each other. Starting from this model, the geometric parameters were varied, and the model's properties were calculated utilizing the finite element method (FEM).

The FEM, first formulated in 1940 by Richard Courant, is a widely used tool for solving partial differential equations [77]. It is creating an approximation of the function $u(x, y, z)$ by calculating a linear combination of trial functions $\phi_i(x, y, z)$ that are multiplied by coefficients c_i:

$$u(x, y, z) \approx \sum_{i=1}^{n} c_i \phi_i(x, y, z) \tag{6.7}$$

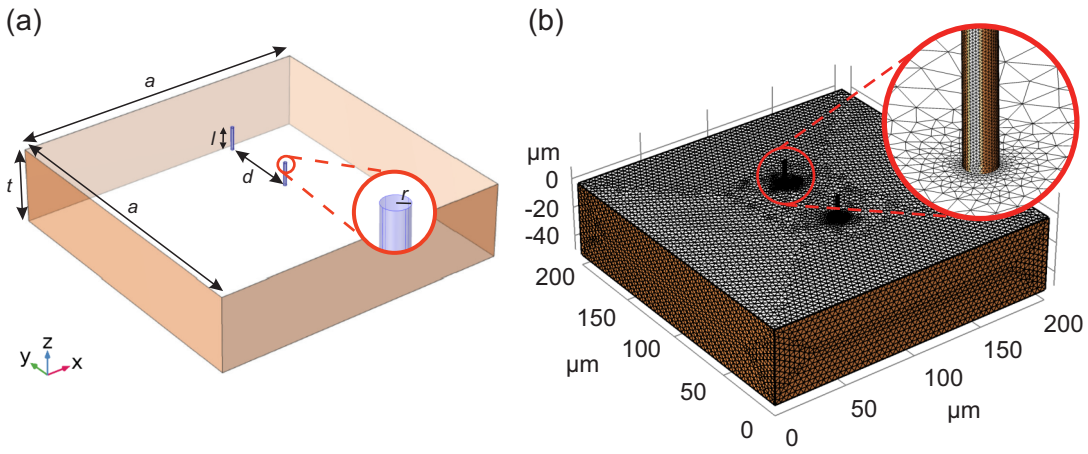

Figure 6.7: Model used for the simulations. **(a):** The sample is approximated by a quadratic plate with the side lengths a and the thickness t. The contact tips are approximated as cylinders with the radii r, length l, and distance to each other d. **(b):** Mesh grid of the model. The more complex the geometry, the finer the mesh was chosen. The initial geometry is given by the following parameters: a=200 μm; t=50 μm; d=50 μm; r=1 μm and l=15 μm.

The domain of the problem, which is in this case the sample and the contacting side tips, is divided into smaller, finite-sized elements, for which the linear combinations are calculated. By this so-called discretization, the domain is covered in a mesh of the finite elements, which are simple geometric structures such as tetrahedrons [78]. When for each element an approximation of the function $u(x, y, z)$ is determined, these are combined to form a global approximation of the differential equations. To achieve an accurate approximation to the problem, the mesh grid is incrementally refined by creating smaller, finite elements until the solution shows convergence. This results in maps of physical values, e.g., the current density $\vec{\mathbf{J}}$, with the values referring to the individual finite element of the model's grid.
In the following, the simulations of the lateral current on the sample will be presented. As a first step, the lateral current density was simulated in dependence on geometric and material aspects[1]. In the second step, the influence of an external magnetic field on the lateral current density, distribution, and direction is simulated and discussed. Finally, in the last step, the thermal aspects of Joule heating are included in the simulation, investigating the heat distribution.

[1]This aspect of the simulation was done in collaboration with Dorothee Herrmann within the frame of her bachelor thesis [79]. Figures 6.7 to 6.12 were originally created by D. Herrmann. They are altered marginally and used in this thesis with her consent.

6.2.1 Current density distribution

For the lateral current that is applied by the two side tips in ideal ohmic contact to the sample at a large distance from each other relative to the contact areas, the tips can be assumed to be point contacts as a first approximation. These contacts are at the positions $\vec{r}_1$ and $\vec{r}_2$ on the surface of the sample crystal with a distance of d to each other. The sample surface and the two point contacts are illustrated in figure 6.8. The illustrated lines refer to the electric field $\vec{\mathbf{E}}$, with arrows indicating the field's direction. The absolute value of the field strength is proportional to the field line density. Due to its relation to the electric field $\vec{\mathbf{J}} = \sigma\vec{\mathbf{E}}$, the current density is proportional to this line density as well, and the current is flowing in the direction of the field lines. Here, σ is the electrical conductivity of the conducting material, which is either the contacting tips or the sample. The largest amount of current density can therefore be found alongside the connecting line in between the contact sites.

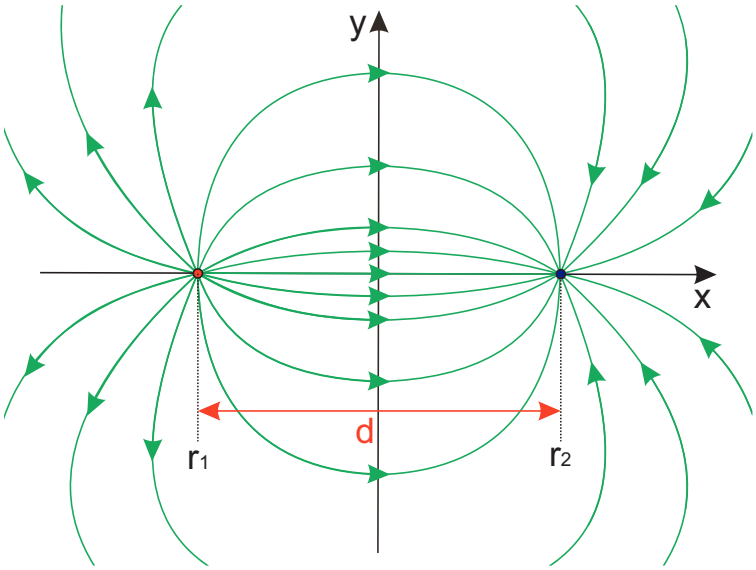

Figure 6.8: Sketch of the electric field in between two point contacts at the positions $\vec{r}_1$ and $\vec{r}_2$ on the sample crystal's surface. The green lines are illustrating the electric field lines $\mathbf{E}$ with their density referring to the electric field strength.

For a three-dimensional sample crystal with a thickness $t > d$ the current density $\vec{\mathbf{J}}$ on a position $\vec{r}$ with a total current I_{12} from $\vec{r}_1$ to $\vec{r}_2$ can also be calculated analytically by:

$$\vec{\mathbf{J}} = \frac{I_{12}}{2\pi}\left(\frac{\vec{r}-\vec{r}_1}{|\vec{r}-\vec{r}_1|^3} - \frac{\vec{r}-\vec{r}_2}{|\vec{r}-\vec{r}_2|^3}\right). \tag{6.8}$$

By defining the coordinate in the centre between the side tips as zero and the x-positions of the tips as $\vec{r}_{x1} = -R$ and $\vec{r}_{x2} = R$, while their y and z values are zero, the current density in

the centre of the coordinate system, which is the position of the centre probe in the three-tip geometry, can be calculated by:

$$J_C = \frac{I_{12}}{\pi R^2}. \tag{6.9}$$

By adding the boundary of the sample crystal being a thin film with a thickness of $t < d$, the expansion of current in z-direction is confined, leading to:

$$J_C = \frac{I_{12}}{\pi R t}. \tag{6.10}$$

However, due to the complexity of the tip's geometry in ultimate proximity to each other, the assumption that the contact sites are point contacts is not suitable. The analytical approximation can be seen as the first step in calculating the current properties, which can be compared to the results from numerical simulations. For modelling the lateral current, the following differential equations of Ohm's law and the continuity equation were utilised:

$$\begin{aligned} \vec{\mathbf{J}} &= \sigma\vec{\mathbf{E}} = \sigma(-\mathrm{grad}\, V) \\ \frac{\delta\rho}{\delta t} + \nabla \cdot \vec{\mathbf{J}} &= 0. \end{aligned} \tag{6.11}$$

Here, V is the electric potential of the field, and ρ is the electric charge density. A boundary condition is added to the simulation by $\vec{\mathbf{n}}\vec{\mathbf{J}} = 0$, where $\vec{\mathbf{n}}$ is the normal vector to all surfaces of the model. This way, the current cannot exit the conducting bodies.
Likewise to the real experimental setup, the side tips are applying the lateral current in the simulation. The current is defined as constant.
In figure 6.9, a simulation of the absolute value of the current density $\mathbf{J}$ on an Ir crystal contacted with PtIr tips is shown. As starting parameters, a total current of 200 mA in between the tips, a tip-to-tip distance of $d = 50\,\mu$m, which is defined by the distances of the contact site's edges to each other, and a contact site radius of $r = 1\,\mu$m are defined. These parameters describe the side tips at relatively large distances from each other and with large contact site radii in comparison to ultra-sharp tunnelling tips. This is done to start from a perspective where the simulation model is comparable to the point contact approximation since $r \ll d$.

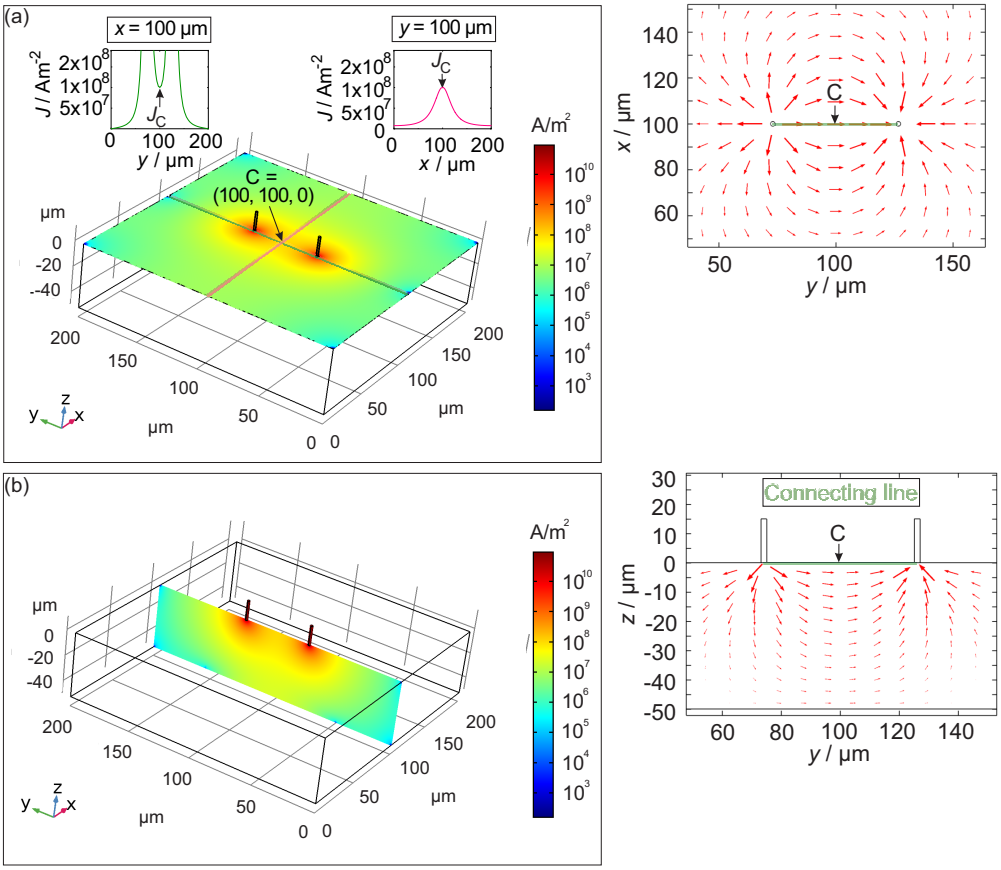

Figure 6.9: Simulation of the current density. **(a) left:** Absolute value of the current density on the xy-plane of the sample surface illustrated by a logarithmic colour scale. In the inserts, the current density is plotted along the marked green and red lines, showing a saddle point at point C (100/100/0). **(a) right:** Electric field on the same xy-plane, with the arrows being proportional to $\log(\vec{\mathbf{E}})$, which also indicate the current direction. A 100% current flow in y direction is visible along the green line, connecting the contact sites. **(b) left:** Absolute value of the current density on a yz-plane that is the cross section of the sample below the contact sites. The values are, like in (a), illustrated by a logarithmic colour scale. **(b) right:** Electric field in the same yz-plane. The current direction below the connecting line is still in the majority in y-direction but is gaining vertical components at increasing distances to the surface. **Simulation parameters:** $a = 200\,\mu$m, $t = 50\,\mu$m, $d = 50\,\mu$m, $r = 1\,\mu$m, $I = 200\,$mA

The results of the simulation with these starting parameters can be easily compared with an analytical calculation based on the point contact approximation, enabling a judgement about the reasonableness of the simulation results. The geometric starting parameters of the sample crystal are $a = 200\,\mu$m and $t = 50\,\mu$m. On the crystal's surface in the left figure 6.9(a) and the crystal's cross section in the left figure 6.9(b), the current density is illustrated by a logarithmic colour scale.

It is decreasing radially around the contact tips, but less so on the connecting line in between the tips. In the inserts of figure 6.9(a), the current density is plotted along the red line parallel to the x-axis and the green line parallel to the y-axis. The green line is crossing the contact points, which have the maximal current density, and shows a local minimum of $\vec{\mathbf{J}}$ at C. The same point is a global maximum on the red line. Thus, C is a saddle point on the sample crystal's surface with a current density of $J_C = 1 \cdot 10^8 \mathrm{Am}^{-2}$.
The right figures of 6.9 (a) and (b) depict the simulated electric field on the sample's surface in (a) and on the sample's cross section in (b). The size and direction of the red arrows are proportional to $\log(\vec{\mathbf{E}})$. Due to the relation $\vec{\mathbf{J}} = \sigma\vec{\mathbf{E}}$, the current direction is also indicated this way. On the connecting line between the tips (green), the current is directed completely in the positive y-direction. With the connecting line showing the least decrease in current density at increasing distances from the tips and the current flowing completely in y-direction there, the measuring centre tip should ideally be placed there. Thereby, C is a suggestive reference point to the current density visible at the centre tip's position.
When comparing the right-hand figures 6.9 to figure 6.8, the result of the simulation shows qualitative agreement to the electric field that is expected from an analytical solution of two point contacts. With the simulation parameters in figure 6.9 $d = t$ both the equations 6.9 and 6.10 may be applied to calculate the absolute value of the current density J_C at the point C with $J_C^{thick} = I/(\pi(\frac{d}{2} + r)^2)$, which is neglecting the vertical confinement of the current expansion in the sample, and $J_C^{thin} = I/(\pi t(\frac{d}{2} + r))$. This results in $J_C^{thick} = 9.42 \cdot 10^7 \mathrm{Am}^{-2}$ and $J_C^{thin} = 4.90 \cdot 10^7 \mathrm{Am}^{-2}$. These values are close to the simulated value of the current density at the point C of $J_C = 1.0 \cdot 10^8 \mathrm{Am}^{-2}$. The deviation is most likely due to the consideration of the contact point's geometry in the simulation. Nonetheless, the simulation model is seemingly delivering reasonable results that can be used to assess the real physical properties of the lateral current applied to a metallic sample by the side tips.
In order to find the determining geometric relations for the current density J_C at point C, which is also assumed to be the position of the centre tip, multiple simulation series were done. By varying the geometric parameters of the tip configuration with tip distance d and radii r and of the sample with thickness t and side length a, the effect on J_C was investigated. As discussed above, the scan range of the centre scanner is, depending on its temperature, up to 6 μm in x- and y-direction. The results for the current density shown in figure 6.9 are varying inside this scan range of 36 $\mu\mathrm{m}^2$ by 5% in maximum. Depending on the geometric configuration, the current density's local variation may change. However, the variations are small, and the evaluation of current densities averaged over a 1 $\mu\mathrm{m}^2$ range is deemed sufficient to learn about the relations between the current density and the geometric configuration of tips and samples.

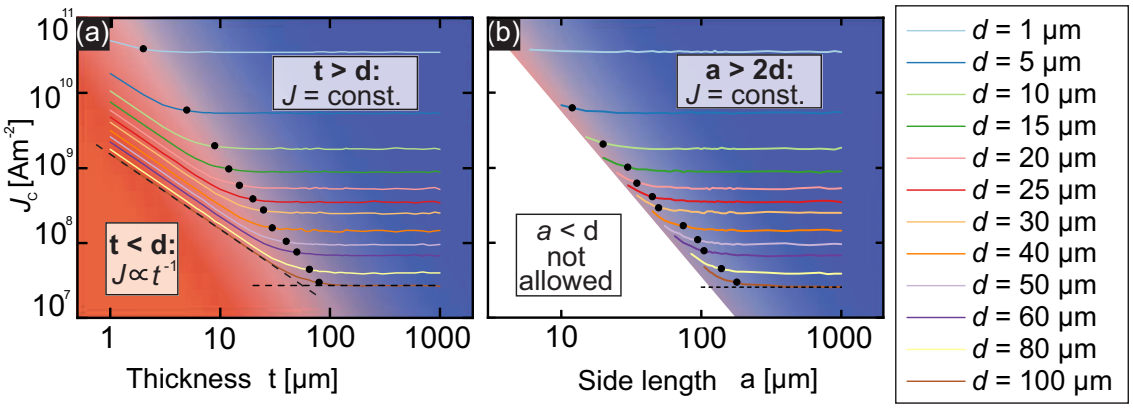

Figure 6.10: Current density J_C resulting from simulation series plotted against the parameters of sample thickness t and sample side length a with varying tip-to-tip distances d. **(a):** Plot of J_C against t. Both axes are logarithmic. The plot is split into two coloured regions. Blue marks the relation $t > d$ and shows no dependence between the current density and t. Red marks the relation $t < d$ and shows the relation $J \propto t^{-1}$. In between, the relation is in a transition phase. The black dotted line shows the average of the $d = 100\,\mu$m curve in the blue area, and the black dots are marking a value 10% above the average of each curve in the blue area. **(b):** Plot of J_C against a. Both axes are logarithmic. The blue area marks the relation a > d and shows no dependence between J_C and a. The geometric relation a < d is geometrically not feasible. In the area between a > d and a < d the relation of J_C and a is in transition, and the black dots are marking a value 20% above the average of each curve in the blue area (the black dotted line for d=100 μm). **Constant simulation parameters:** I=200 mA, r=1 μm

In figure 6.9, some effects of the model's boundaries on the current density can be observed. While the current density decreases radially around the contact points, this distribution seems to be suppressed at the sample model's edges. To investigate the effects of the sample's geometry on J_C, two simulation series were done where the geometric parameters of the sample thickness t and the sample side length a were varied. Additionally, the tip-to-tip distance d was varied from 1 μm to 100 μm in each series.

In figure 6.10, the resulting values are plotted, with figure 6.10(a) showing the current density J_C plotted against the sample thickness t and figure 6.10(b) showing J_C plotted against the sample side length a. Both axes of both plots are logarithmic. The graphs shown in different colours mark the varying tip distances. One can observe an anti-proportional relation of the J_C to d in both plots, which is in agreement with the radial decreasing of the current density around the contact tips. The plot (a) can be separated into two areas. The right shows the plot with the relation $t > d$, shown in blue, and the left shows the plot with the relation $t < d$, shown in red. The blue area shows no observable relation between J_C and t. This may be due to the large distance between the sample's surface and bottom, with the boundary affecting the current locally and having no relevant effect on the current density at C.

When the sample is thin enough, the effect on J_C becomes evident. The red area in figure

6.10(a) shows an anti-proportional relation $J_C \propto t^{-1}$, which appears as a straight decreasing curve in the double logarithmic plot. This behaviour is in agreement with the analytical solution of equation 6.10, which also includes this relation. In the case of d=1 μm (light blue), where the point approximation is not applicable, the behaviour deviates as the current density is decreasing more slowly with increasing sample thickness. In the zone in between the blue and red areas in figure 6.10(a), which is shown as colour transition of red into blue, an increasing of J_C with decreasing thickness t can be observed. To categorise this relation, each of the constant curves in the blue area was averaged, and the average was compared to the increase of each curve. As an example of this, in figure 6.10(a) the average of the curve for $d = 100\,\mu$m is indicated by a black dotted line. The black dots on the curves are marking an increase of 10 %, which occurs at about $t \approx d$ for each. At this point, the sample's edge boundary effect seemingly becomes relevant to J_C and the relation between the current density and thickness t is transitioning to the hyperbolic relation of the thin film approximation.

In figure 6.10(b), the blue area shows no relation between the current density J_C and the sample's side length a. The area for the relation $a < d$ is geometrically not feasible since the side tips would not be in contact with the sample. However, at the edge of the blue area towards $a < d$, a transition to another relation of J_C to the length a can be observed. When again comparing it to the average of J_C in the blue area, a characteristic point of increase can be identified. At $a \approx 2d$, the black dots are marking an increase of 20% for each curve. The more steep transition in comparison to figure 6.10(a) may be explainable by the sample model's symmetry. In the case of small t, the spreading of current is confined by the sample's edge in negative z-direction and by the sample surface. In the case of small a, the spreading of current is confined in x- and y-direction, as well as the sample surface. This results in a confinement of current from more directions and a more steep change of J_C for small a.

To further investigate the dependence between the current density J_C and the tip-to-tip distance d, as well as the tip radii r, another series of simulations was done, varying r and d. Figure 6.11 shows the current density J_C plotted against d for multiple curves with varying r from 10 nm, which is an expectable value for ultra-sharp tips, to 10 μm. Again, both axes are logarithmic. It should be noted here that d is the distance from the edge of one contact area to the other and not the distance from centre of point contact to the other centre. This way, a distance of $d < r$ does not indicate an overlapping of contact areas.

The curves are compared to the black dotted line, which shows the current density that is analytically calculated with the assumption of point contacts using equation 6.9. When substituting $R = \frac{d}{2}$ (R does not refer to a radius here) the equation shows the relation $J_C \propto d^{-2}$.

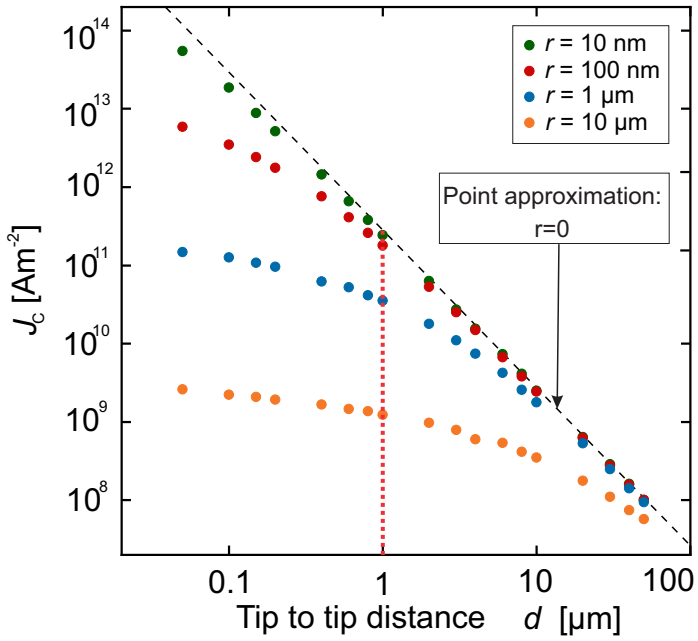

Figure 6.11: The current density J_C plotted against the tip-to-tip distance d with varying tip radii r. Both axes are logarithmic for easier interpretation. The dotted line shows the curve for the analytical approximation of point contacts with the relation $J_C \propto d^{-2}$. **Other simulation parameters:** $l = 15\,\mu$m, $I = 200$mA, $a = t = 200\,\mu$m

In the plot, a deviation of the data points from the model with the point contact assumption can be observed that increases with decreasing d and increasing r. This reflects that the assumption of point contacts becomes less applicable with a decreasing difference between d and r. In the case of tip radii equal to d or smaller, the current density is approaching saturation levels dependent on the tip radii. For example, while the orange data points for $10\,\mu$m are approaching a level of J_C between 10^9Am^{-2} and 10^{10}Am^{-2} for small d, the data points for 100 nm saturate at around 10^{13}Am^{-2}. When looking at fixed distances d, as shown by the red dotted line in figure 6.11, the strong dependence of J_C on r becomes even more apparent.

A possible explanation may be found within the field line model, which is illustrated in figure 6.8. The field lines have source points on the contact area's edge, with the line extending perpendicular to the circle's tangent. With a larger contact area, more source points are available, resulting in fewer field lines per unit length on the contact area circumference and a smaller current density between the contact sites.

For experimental applications, a few key statements can be concluded from these simulations.

- The current density reaches a relation of $J_C \propto t^{-1}$ for $t < d$.
- J_C is increasing with decreasing tip-to-tip distance d and reaches a saturation level for small d.
- J_C is for small d strongly dependent on the tip radii r including its saturation levels.

Therefore, in order to reach a high current density at point C, small tip radii, a small tip-to-tip distance, and a thin conducting sample are favourable. As described above in chapter 4.3, the creation of ultra-sharp tips is feasible, and tip radii as small as 10 nm can be reached. While experiments on the Pd/Fe/Ir(111) system [2] have been done on Ir bulk crystals so far, there have also been studies on thin film systems that are deposited on a non-conducting substrate like the Ir/YsZ/Si(111) multilayer system [6]. The conductive layers in these systems can be thinner than 1 μm. As discussed in chapter 4.3, small tip-to-tip distances are accessible for the MP-STM.

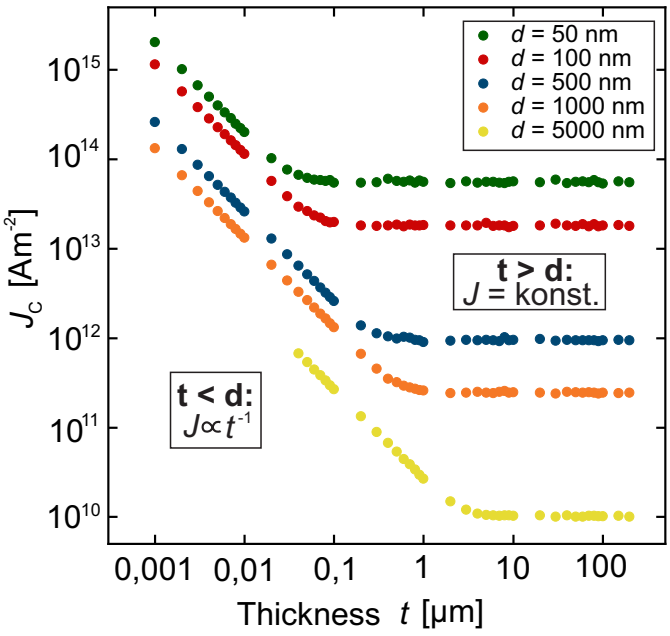

Figure 6.12: The current density J_C plotted against the sample thickness t for varying tip-to-tip distances. The simulation parameters are chosen to be close to the limit of experimental feasibility. Both axes of the diagram are logarithmic. **Simulation parameters:** $r = 10\,\text{nm}$, $l = 15\,\mu\text{m}$, $I = 200\,\text{mA}$, $a = 4d$.

With the limits of feasibility for the parameters known, the simulation series of figure 6.10(a) was repeated with parameters closer to these limits. The results are plotted in multiple graphs with varying tip-to-tip distance in figure 6.12, with both axes being logarithmic. Like in the

simulation series of figure 6.10(a), the plot shows a hyperbolic relation of J_C to t for small sample thickness. However, even for $t > d$, where the sample thickness is not influencing J_C, current densities above the threshold of $10^{10}\frac{\mathrm{A}}{\mathrm{m}^2}$ can be reached when using ultra-sharp contact tips and reaching a tip-to-tip distance below $5\,\mu$m. Both of these parameters have been discussed above in sections 3.5 and 4.3 and can be considered achievable. Therefore, even when applying lateral currents on a bulk crystal ($t \gg d$), the current density threshold of $10^{10}\mathrm{Am}^{-2}$ is achievable at $d < 5\,\mu$m. When considering the results of the lateral current experiments, the total lateral current of $I = 200\,\mathrm{mA}$ is very high, and negative effects due to Joule heating may be expected. However, considering the equations 6.8 and 6.9 for the point contact approximation, the current density J_C is linearly dependent on the total applied current. If a similar dependency can be assumed for the simulations shown in figure 6.12, a total lateral current in the μA range is sufficient to achieve the threshold of $10^{10}\mathrm{Am}^{-2}$ at tip-to-tip distances in the nanometre range.

However, it should be considered that some of the simulation's aspects may be imprecise. The sample surface is simulated as a flat surface, while in reality it features atomic step edges, defects, and dislocation lines. These may alter the surface's electrical conductivity relative to the bulk's conductivity and may have direction-dependent effects on the current. Furthermore, the tip contact's geometry can deviate from a circular contact area, which can result in a less symmetric current density distribution. In the following, the additional effects of Joule heating and the impact of an external magnetic field on the lateral current will be investigated.

6.2.2 The Hall effect

As a next step, an external magnetic field in z-direction of the sample was included in the simulation. For this, the interaction of the lateral current with the external magnetic field was included in the differential equations 6.11. The term for the electric field in the relation $\vec{\mathbf{J}} = \sigma\vec{\mathbf{E}}$ is thereby extended as follows [80, 81]:

$$\vec{\mathbf{E}} = \vec{\mathbf{E}}_0 + \vec{\mathbf{E}}_\mathrm{H} = \vec{\mathbf{E}}_0 + \vec{\mathbf{v}} \times \vec{\mathbf{B}}. \tag{6.12}$$

In this equation, $\vec{\mathbf{E}}_0$ is the electric field without interaction with the magnetic field, and $\vec{\mathbf{E}}_\mathrm{H}$ is the component of the electric field that is describing this interaction. $\vec{\mathbf{v}} \times \vec{\mathbf{B}}$ is the cross product of the charge carrier drift velocity and the external magnetic field. This term can also be described by using the Hall coefficient R_H of the conductors in the model as $\vec{\mathbf{v}} \times \vec{\mathbf{B}} = R_H(\vec{\mathbf{E}} \times \vec{\mathbf{B}})$. This results in:

$$\vec{\mathbf{J}} = \sigma(\vec{\mathbf{E}} + R_H(\vec{\mathbf{E}} \times \mathbf{B})). \tag{6.13}$$

The specific conductance σ can be rephrased as a tensor including the term for magnetic interaction since the magnetic field consists of the z-component B_z only. Thus, equation 6.13 can be written as:

$$\vec{\mathbf{J}} = \hat{\sigma} \cdot \vec{\mathbf{E}} = \sigma \begin{pmatrix} 1 & \alpha & 0 \\ -\alpha & 1 & 0 \\ 0 & 0 & 1 \end{pmatrix} \cdot \vec{\mathbf{E}}, \tag{6.14}$$

with $\alpha = \sigma R_H B_z$. The drift velocity of charge carriers inside a conductor is dependent on the conducting material's purity, structure, and temperature T. A parameter that is used as a benchmark for conductor purity and crystal structure is the residual-resistance ratio (RRR). It is defined by the quotient $\mathrm{RRR} = \frac{\rho(295\mathrm{K})}{\rho_0}$ with the resistivity ρ at room temperature and the residual resistivity ρ_0 at the lowest possible temperature of the electric conductor. For elemental conductors, such as copper, a high RRR value indicates a high material purity. It is influenced by scattering sources like defects, contamination, and grain boundaries. Therefore, it can only be individually measured for each conductor, whereby ρ_0 is extrapolated by the resistivity at the minimal achievable temperature in a measurement setup. The drift velocity is, according to the Drude model, equal to the product of the electric field vector and the electrical mobility μ:

$$\vec{\mathbf{v}} = \mu\vec{\mathbf{E}}. \tag{6.15}$$

The relation $\sigma = qn\mu$ (with q as charge and n as number of charge carriers) links the drift velocity to the specific conductivity σ. Since the Hall coefficient is also directly linked to the drift velocity, both parameters are dependent on the temperature T and the RRR value. Furthermore, they are dependent on the external magnetic flux density, thus forming a complex parameter space with $\sigma(\mathrm{RRR}, \mathrm{T}, \mathrm{B})$ and $R_H(\mathrm{RRR}, \mathrm{T}, \mathrm{B})$. By fitting the parameters to the experimental environment of interest, information about the effect of the external magnetic field on the lateral current can be gained.
Since the exact RRR factor for the used iridium crystals is not known, for the simulation it was assumed to be at $3 \cdot 10^3$, which is applicable for a single crystalline elemental material, like the Ir(111) used in our STM experiments, according to [81].
The temperature was chosen to be the boiling point of helium at 4.2 K. This poses a reasonable starting point for lateral current experiments with varying temperatures since it can be achieved by using the 1 K-pot as a liquid helium reservoir without pumping on it and without using its 4 W electric heater.

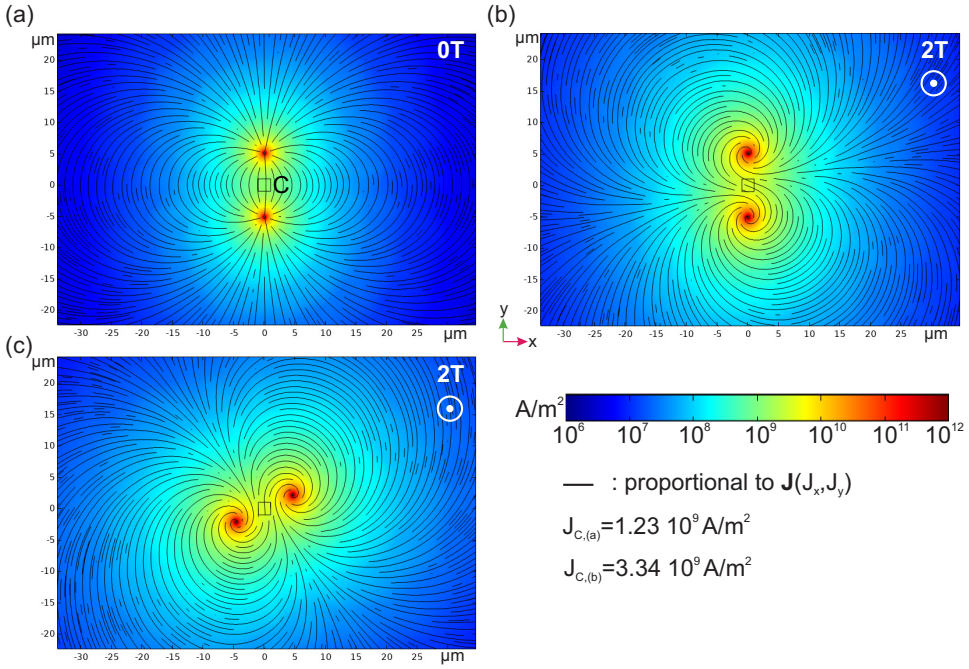

Figure 6.13: Current density simulations, which include the Hall effect. The images show the current density on a logarithmic colour scale with black lines that are proportional to the x- and y-components of the current, indicating the current direction. **(a):** Surface with no external magnetic field applied for comparison. **(b:)** By applying an external magnetic field of 2 T field strength, the current's direction in the area C in the centre between the tips is tilted strongly. Furthermore, the current density is decreasing more slowly with increasing distance from the contact sites. **(c):** The tilting of the current direction at C may be compensated by rotating the contact tips according to the tilt angles. **Simulation parameters:** For all: $a = t = 200\,\mu\mathrm{m}$ $d = 10\,\mu\mathrm{m}$ $r = 100\,\mathrm{nm}$ $I = 100\,\mathrm{mA}$ for (a): $B = 0$ and for (b,c): $B = 2\,\mathrm{T}$.

The simulation of the lateral current in interaction with an external magnetic field in z-direction is shown in figure 6.13. The current density is shown as a logarithmic colour scale, and the black stripes are proportional to the vector of the surface current density $\vec{\mathbf{J}}_{xy}$. Figure (a) depicts the current density map with no external magnetic field applied for comparison. There, the current path is following the electric field in between the contact sites, as shown above in the simulation of figure 6.9. The current density map is in agreement with the findings of the simulation series discussed above and presented in figure 6.11. It shows a current density $J_C = 1.23 \cdot 10^9 \frac{\mathrm{A}}{\mathrm{m}^2}$ at C. The lines in between the contact sites are indicating a current parallel to the y-axis on the connecting line and gaining x-components with increasing distance from the centre point C, which is marked by the black square.
When adding an external magnetic flux density of 2 T in z-direction, the field's interaction with the lateral current is observable. The current direction in the proximity of point C is tilted in x-direction, and the current that was extending radially around the contact sites in the case of (a), is forced into a spiral path around the contact site. These spiralling paths show similarity to the spiral current pattern caused by the Hall effect on current in a Corbino geometry [82]. The colour scale indicates a slower decline in current density with increasing distance from the contact points. This is likely due to the electrons being forced on the spiral paths, while they would connect in a more direct path without an external magnetic field. Simultaneously, the current density at the contact points appears to be greater. With a current density of $J_C = 3.34 \cdot 10^9 \frac{\mathrm{A}}{\mathrm{m}^2}$, it is reasonable that the current is unable to spread to the simulation's borders as it is forced into spiral paths around the contact points.
Figure 6.13(c) shows an alternative geometric configuration of the contact tips, which compensates for the change of current direction in C by rotating the tips around it. This way, the current direction can be stabilised in an experiment that, for example, investigates the lateral currents effect on a structure in correlation to a varying external magnetic field. One such possible experiment may be the manipulation of skyrmions with a lateral current while the skyrmions are stabilised in an external magnetic field. The direction of the current may be important to the interpretation of results, especially when taking into account additional interactions with the magnetic field like the skyrmion Hall effect. However, it should be noted that not only the current direction but also the deviation of the current direction in the area in proximity to point C is expected to be influenced. This can also be observed in the results of figures 6.13(b) and (c), where the black lines, indicating the current direction, are less coherent in their direction in comparison to result (a).
Based on the equation of the Lorentz force:

$$\vec{\mathbf{F}} = q(\vec{\mathbf{E}} + \vec{\mathbf{v}} \times \vec{\mathbf{B}}), \tag{6.16}$$

which forces the electrons on their spiral path in the simulations, an inversion of the current path is expected when either the current polarisation or the magnetic field are inverted. However, more testing and refining of the simulation is needed to investigate this in the context of the geometric configuration. Furthermore, the angle of tilting in the current direction is based on a complex parameter space of the parameters RRR, T, and B_z. To learn more about these relations more and more refined simulation series and experiments are needed to gain more knowledge. Experimentally, the current may be investigated while controlling the external fields B_z and T, generating insight about the RRR of the sample in use and the current's interaction with the field. This could be done by scanning tunnelling potentiometry, which involves investigating the local chemical potential of the sample surface, or by investigating the effect on skyrmions.
Experiments, including the application of lateral currents and simultaneously external magnetic fields, should be accompanied by simulations of the current direction. Although the limitations in accuracy due to the neglected surface structures should be considered, this can help in interpreting experimental results. A further refinement of the simulation geometry and more simulation series with varying external magnetic fields, temperatures, and RRR values are needed as well. Also, the determination of the RRR value of an Ir(111) sample in use by a four-probe measurement at room temperature versus low temperature may help to additionally refine the simulation model and interpret experimental results.

6.2.3 Joule heating

Since the sample's temperature can have a considerable impact on its properties, all potential heat sources need to be considered in an experiment. This includes the application of currents to the sample. Electrons are moving as charge carriers through the conductors and are colliding with and scattering on crystal defects and phonons. These interactions generate heat, which is also known as Joule heating. As the lateral current experiments indicated, the heat deposited by this mechanism needs to be carefully considered.
In order to include Joule heating into the simulation, the differential equations 6.11 relevant to the simulation of the current density are extended by the following three differential equations:

$$\frac{dP}{dV} = \vec{\mathbf{J}} \cdot \vec{\mathbf{E}}, \tag{6.17}$$

which describes the deposition of heat power per volume $\frac{dP}{dV}$ by Joule heating [83]. The heat will be phrased as Q_e in the following. As above, $\vec{\mathbf{J}}$ and $\vec{\mathbf{E}}$ are referring to the current density and the electric field.

The conductive heat flux density $\vec{\mathbf{q}}$ is described by Fourier's law:

$$\vec{\mathbf{q}} = -k\nabla \cdot \mathbf{T} \tag{6.18}$$

where k is the thermal conductivity of the heat-conducting medium.
The gradient of the conductive heat flux density is described by a heat balance equation:

$$\nabla \cdot \vec{\mathbf{q}} = Q_e \tag{6.19}$$

which links the conductive heat flux density to the heat power deposited by Joule heating.
The heat balance function, used by Comsol Multiphysics®, is, in its completeness, written as:

$$\rho C_p \vec{\mathbf{u}}_{trans} \nabla T + \nabla(\vec{\mathbf{q}} + \vec{\mathbf{q}}_r) = Q_{ted} + Q \tag{6.20}$$

The first term describes heat transfer by convection, with $\vec{\mathbf{u}}_{trans}$ being the velocity vector of the translational motion of a fluid. The second term describes heat transfer by conduction with the conductive heat flux $\vec{\mathbf{q}}$ and by radiation with the radiation heat flux $\vec{\mathbf{q}}_r$. These are equal to the heat generated by thermoelastic damping Q_{ted} and other heat sources Q, which is in this case caused by Joule heating Q_e. Since the samples in the MP-STM are in a vacuum and shielded from thermal radiation, heat transfer through thermal convection and heat influx through radiation are negligible. Thermoelastic damping can be neglected as well, since the modelled structures are not experiencing mechanical stress or vibrations.
Since the experiments are conducted at temperatures ranging from 1.5 K to 100 K the expected power radiated by an area heated by Joule heating is very low. According to the Stefan-Boltzmann law, a surface $A = 1\mu\text{m}^2$ at a temperature of $T = 150\,\text{K}$ would radiate off a power of $P = \epsilon\sigma_B A T^4 \approx 2.8 \cdot 10^{-11}\,\text{W}$, with the Stefan-Boltzmann constant σ_B and the emissivity ϵ, which is assumed to be 1. In comparison, the power deposited by Joule heating in a volume $V = 1\,\mu\text{m}^3$ at a temperature of 100 K can be approximated by $Q_e \cdot V = \frac{J^2}{\sigma} \cdot V$ which results in $Q_e \cdot V = 1.1\,\mu\text{W}$ for a current density of $J = 10^{10}\,\frac{\text{A}}{\text{m}^2}$ and an electric conductivity at 100 K of $\sigma(100\,\text{K}) = 9 \cdot 10^7\,\frac{\text{S}}{\text{m}}$. Thus, the power radiated off can be neglected over the power deposited by Joule heating.
Additionally, a boundary condition is included by $-\vec{\mathbf{n}}\vec{\mathbf{q}} = 0$, which forbids heat flow outside the modelled bodies.

As discussed above, the specific electrical conductivity σ of a conductor is dependent on its temperature T and its purity. This is the case for the thermal conductivity k as well, which is dominated by the electron heat transfer in metals. While electron-phonon scattering dominates the electric resistivity and the thermal conductivity at higher temperatures, it becomes less decisive at low temperatures, giving rise to electron scattering events on defects, impurities, and grain boundaries. Therefore, the crystal structure and the material's purity are becoming more relevant, which is benchmarked by the RRR value, as mentioned above. Furthermore, in alloys, the scattering between different kinds of elements becomes an important factor for the residual resistivity, resulting in a low RRR value and thereby relatively low thermal and electrical conductivity at low temperatures in comparison to elemental metals [81].

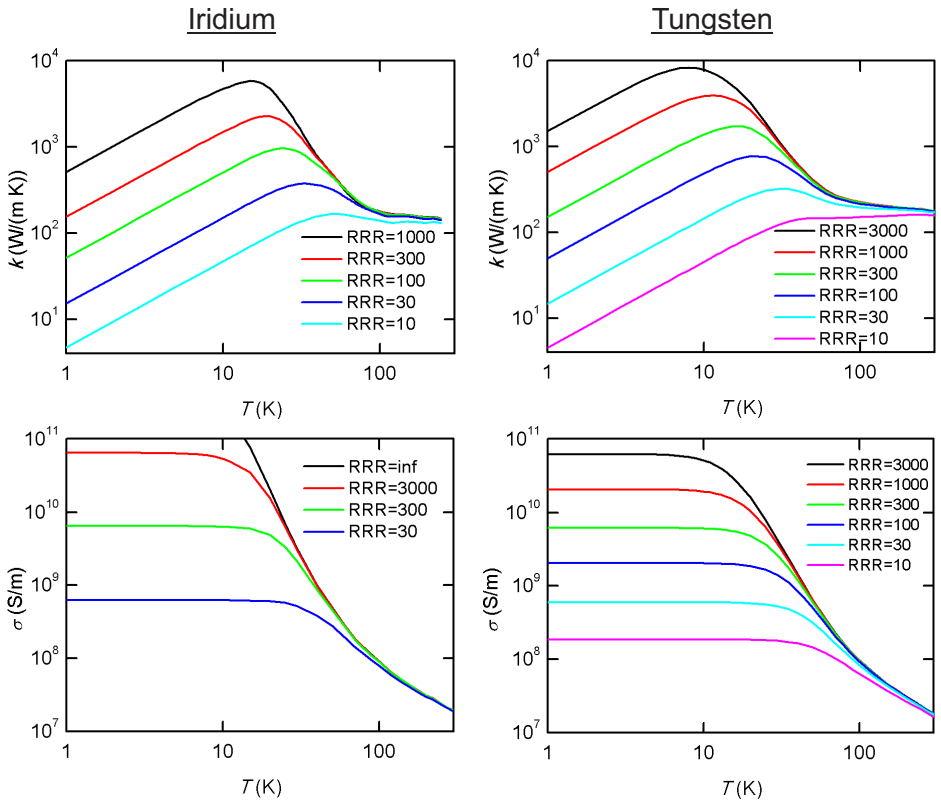

Figure 6.14: Electric (σ) and thermal (k) conductivities of iridium (left) and tungsten (right) plotted against temperature T for varying RRR values. The plots are composed of data from literature and data extrapolated based on the former [84, 85, 86, 87, 88, 89, 90, 91].

In figure 6.14, the electric and thermal conductivity of iridium and tungsten are plotted against temperature T in a double logarithmic diagram. Additionally, the RRR values of the materials have been varied, which shows the effects of temperature and purity on their conductivities. The electrical conductivity of both metals is increasing with decreasing temperature due to less electron-phonon scattering, reaching a saturation point that is dependent on the RRR value.
The thermal conductivity of both metals is reaching a maximum in temperature and intensity, which is influenced by the RRR value. The temperature of the maxima is in agreement with the temperature of the electric conductivity reaching saturation. This may be due to electron heat transfer being the dominant mechanism in metals, which has reached saturation at this temperature. At lower temperatures, the thermal conductivity is decreasing since the heat flux by electron heat transfer is no longer increasing and the heat transfer by vibration of adjacent atoms is decreasing further.

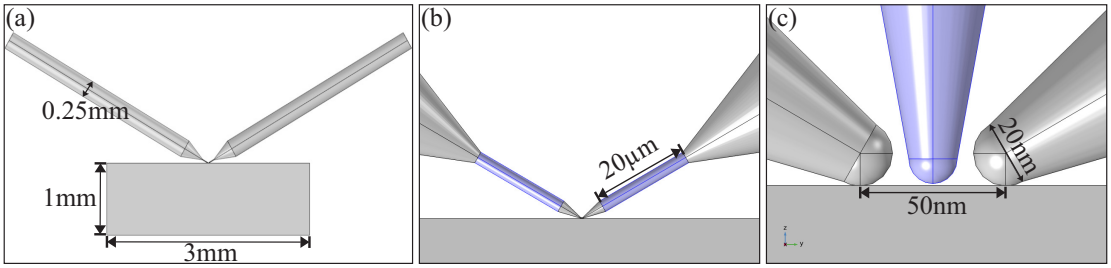

Figure 6.15: Sectional side view of the simulated model. **(a):** Overview. **(b):** Zoom shows the micro-tips. **(c):** Zoom shows the contact points and a potential central tip in between (which is not included in the simulation).

It can be expected that the tip's and the sample's geometry will influence the heat dissipation. In order to get more precise results, the simulation model geometry was refined and oriented on the ultra-sharp tips and samples used for experiments. The new geometry of the simulated model is shown in figure 6.15. The quadratic sample is modelled with the side length $a = 3\,\mathrm{mm}$ and the thickness $t = 1\,\mathrm{mm}$. The contact tips are modelled with a $250\,\mu\mathrm{m}$ diameter, cylindrical microtips of $20\,\mu\mathrm{m}$ length, and tip radii of $r = 10\,\mathrm{nm}$. The tips, which have a tip radius r_n, are penetrating the modelled sample by $e = 0.5\,\mathrm{nm}$, which results in a contact radius of $r_c = \sqrt{e(2r_n - e)} \approx 4.4\,\mathrm{nm}$. Their contact areas are positioned at a $d = 50\,\mathrm{nm}$ distance from each other (measuring from edge to edge), which allows enough space for the centre tip in between. From a geometric point of view, this is close to the minimal achievable tip distance, giving an upper limit for the current density achievable by changing the tip distance. In reference to the results discussed above, this should result in a current density on the order of $10^{14}\,\frac{\mathrm{A}}{\mathrm{m}^2}$ at the centre point in between the tips when applying a current of $I = 200\,\mathrm{mA}$.

For simulating the thermal development due to Joule heating, these geometric parameters remained unchanged, and the applied current was varied. For exceeding the threshold of $10^{10}\,\frac{\mathrm{A}}{\mathrm{m}^2}$, a current of just $20\,\mu$A should be sufficient, assuming the current density is linearly dependent on the total applied current.
Since low RRR values result in lower thermal conductivities at low temperatures, a higher temperature increase may be expected. Low estimates of RRR values were used for the side tip's and sample's materials in order to create a worst-case scenario and an upper limit of the expected temperature increase.
When installed into the UHV chamber, the MP-STM is cooled by a helium bath cryostat. The sample is connected to that cryostat via the microscope's body, which is thermally connected with the sample at its bottom side and at the ends of the contacting tips. These interfaces to the STM body are considered heat sinks in the simulation. This means their temperature is set to the initial temperature used for the simulation T_0 and cannot be increased.

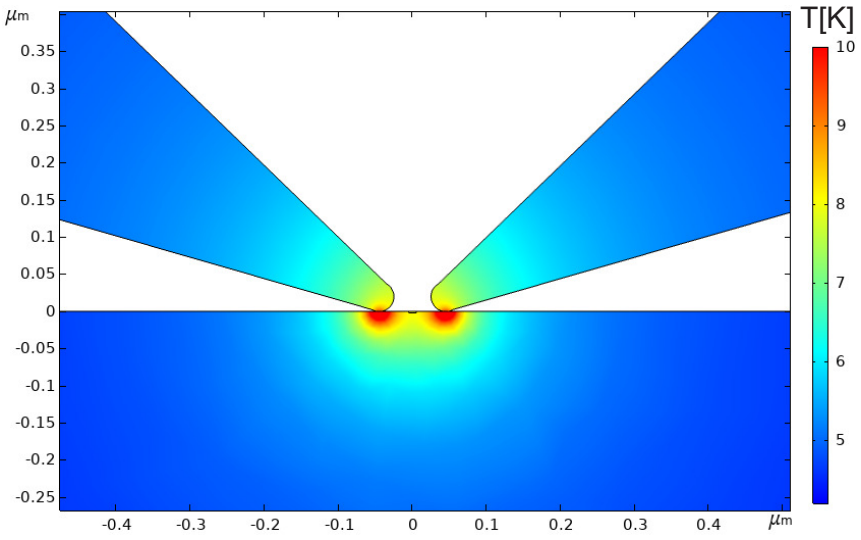

Figure 6.16: Temperature map of the model's sectional side view in equilibrium, indicated by a colour scale. **Simulation parameters:** $\mathrm{T}_0 = 4.2\,\mathrm{K}$, $I = 10\,\mathrm{mA}$, $\mathrm{RRR}_{\mathrm{Ir}} = 100$, $\mathrm{RRR}_{\mathrm{W}} = 100$.

In figure 6.16, the result of such a simulation is shown as a sectional side view for fixed parameters for RRR values of 100, initial temperature $T_0 = 4.2\mathrm{K}$, and applied current $I = 10\,\mathrm{mA}$. The result shows the system at thermal equilibrium while the current is applied, and the temperature is indicated by a colour scale ranging from 4.2 K to 10 K. The temperature map shows a radial decrease in end-temperature around the contact points and a local minimum in the centre of the connecting line in between the tips. This similarity to the current density simulation seems to reflect the relation of deposited heat by Joule heating to the current

density described in equation 6.17.

A simulation series was done in order to investigate the relation of equilibrium temperature to the applied total current and the RRR values of tips and samples. Therefore, the temperature at the contact sites as well as the point C between the contact tips were calculated. Since the current density is expected to be maximal at the contact sites, the highest temperature increase is expected there. The data points are plotted against the applied total current in three curves with varying RRR values in figure 6.17.

As expected, the temperature is increasing with the total applied current, but it also seems to be strongly dependent on the RRR value. With a higher RRR value, the increase in temperature is less steep with larger total currents.

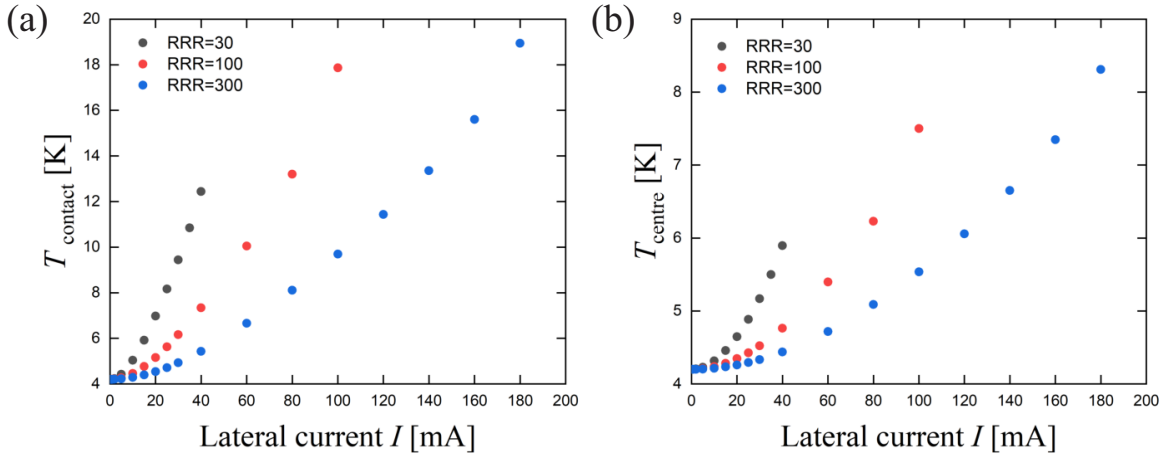

Figure 6.17: Temperature of **(a)** the tip's contact points and **(b)** the centre in between the contact tips plotted against applied current for varying RRR values. For the tips and the sample, the same RRR values were assumed for simplicity. $T_0 = 4.2\,\mathrm{K}$

The difference in temperature increase between the contact sites and point C is noteworthy. This difference amounts to a factor of about two for some data points, which indicates a strong cooling effect of the sample and a low spreading of heat. Furthermore, for the curve of $\mathrm{RRR} = 300$ a temperature increase of less than 5 K at C from the starting temperature 4.2 K can be observed for currents of up to 180 mA. As mentioned before, this total current should be sufficient to apply a current density above the threshold of $10^{10}\,\frac{\mathrm{A}}{\mathrm{m}^2}$.

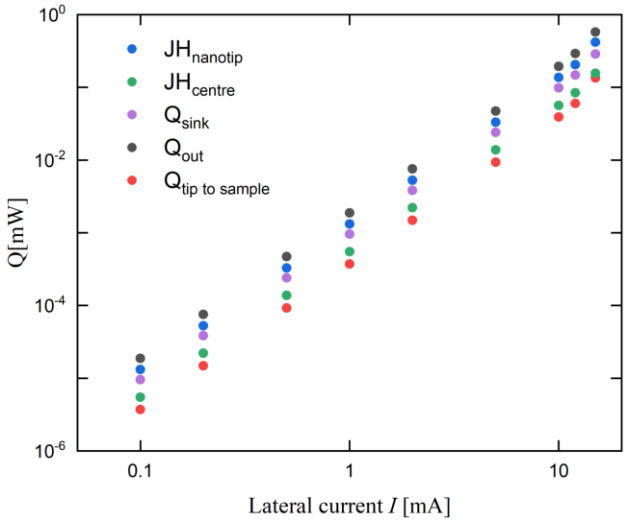

Figure 6.18: Power deposition by Joule heating and heat flow in thermal equilibrium plotted against total current. **Simulation parameters:** $\mathrm{RRR_W} = 10$, $\mathrm{RRR_{Ir}} = 10$, $T_0 = 4.2\,\mathrm{K}$

It should be mentioned that when starting at a higher temperature, a higher increase in equilibrium temperature is to be expected due to the thermal and electrical conductivity decreasing with increasing temperature. Since the RRR value for a single crystalline material with high purity can be estimated to be more than 10^3 [81], an even less steep increase in temperature should be expected in an experiment, with the tips and the sample being highly pure. For alloys like PtIr, however, lower RRR values are to be expected since the minority metal atoms are acting like impurities and lead to a high residual resistance. It is therefore advisable to use side tips of pure materials for contact and no alloys.

As a next step, the heat flow leading to the temperature equilibrium in the first place can be evaluated. Figure 6.18 shows the amount of heat power being generated at the contact sites ($\mathrm{JH_{nanotip}}$) and the sample's centre ($\mathrm{JH_{centre}}$), as well as the heat flow out through the heat sinks ($\mathrm{Q_{sink}}$), and in between the tip and sample ($\mathrm{Q_{tiptosample}}$) plotted against the total applied current. The heat flow of both heat sinks, the sample crystal and the contact tips, is about equal in amount. Therefore, $\mathrm{Q_{sink}}$ of both sinks is plotted as single data points. Their sum is plotted as $\mathrm{Q_{out}}$. Both axes are plotted logarithmically.

The data of $\mathrm{JH_{nanotip}}$ confirm the assumption that in the simulation the most heat is deposited in the point contacts due to the high current density passing through the confined geometry of the microtip. While the heat flow into the cooling sinks is equal for the tips and the sample, a finite part of the heat from the tips is flowing to the sample. This indicates that the contact tips are important for the consideration of Joule heating for the application of lateral currents on iridium.

The geometric configuration of contact tips and samples and the total applied current are sufficient to surpass the threshold of a current density of $10^{10}\,\frac{\mathrm{A}}{\mathrm{m}^2}$, as discussed above. With these parameters, an increase in temperature in equilibrium of less than 10 K was calculated. Therefore, harmful effects on the investigated systems are not expected. For example, the phase diagram of skyrmions on the Pd/Fe/Ir(111) thin film system, which was investigated by P. Lindner [21], shows stable skyrmions at temperatures $T < 80\,\mathrm{K}$ and in external magnetic fields $B > 1\,\mathrm{T}$. Therefore, an increase of 10 K is tolerable for the investigation on skyrmions. Another important finding of the simulation is the large impact of the RRR value on the temperature increase, which leads to the conclusion that elemental metals of high purity should be used for the contact tips. Alloys, such as PdIr, have low RRR values and are not preferable for the application of lateral currents. As discussed above, this may be the explanation for the rapid change in z-signal in the experimental data of the lateral current experiments. A repetition of the lateral current experiments with contact tips made of pure tungsten may give more insight into this.

In future experiments that include the application of lateral currents, the thermal simulation will be useful to assess potential experimental limitations and to interpret experimental data. In order to refine the simulations, the variation of geometric parameters as well as the interaction with external magnetic fields should be included. Another interesting aspect is the sample thickness. When applying lateral currents to thin conductor systems, a respective simulation can be advantageous.
The main objective of the thermal simulation was to assess the feasibility of the application of high current densities to bulk crystal samples. It can be concluded that a local application of current densities above the threshold of $10^{10}\,\frac{\mathrm{A}}{\mathrm{m}^2}$ is feasible, and even higher current densities are accessible without harming effects on the structures by Joule heating.

Conclusion

This thesis presents a home-built MP-STM that is designed for three tip experiments capable of high-frequency applications in UHV, in a temperature range of 1.5 to 100 K, and in the presence of external magnetic fields with flux densities of up to 3 T.
The design solutions for the major challenges that accompany the ambitious requirements of the MP-STM were shown. These include the following key features that deviate from conventional STM designs: Ultra-sharp STM tips are used that feature small tip radii and small opening angles, fulfilling the geometrical requirements to approach them in close proximity to each other. The electrical connection of the STM tips is shielded by coaxial cabling to enable the transmission of high-frequency signals. For the side scanning units in which the tunnelling junctions are distant from their tube scanners' central axes, S-scanners are utilised to prevent a strong vertical displacement during lateral scanning. A lateral coarse drive was developed for the side scanning units. The tips are approached by optical means utilising a long-distance microscope equipped with a Maksutov telescope in a Cassegrain configuration.

As proven by test measurements, all three of the separate functioning scanning units are capable of stable and precise imaging. Their spatial resolution is sufficient to image the atomic lattice of highly oriented pyrolytic graphite and the atomic step edges of Au(111) in ambient conditions on an air-cushioned table, and they can be operated simultaneously on the same sample. It was also shown that the right and the centre STM tips can be brought into sufficient proximity by optical means to be in overlapping scan ranges. Both scanning units were imaging distinct features on HOPG, which are visible in both scans, which proves their close proximity to each other. Furthermore, it shows that the long-distance microscope's spatial resolution is sufficient to approach the right tip into the scan range of the centre tip.
For spin-polarised scanning tunnelling microscopy, a home-made etching method was developed to etch ultra-sharp single-crystalline chromium tips. One chromium tip, which was etched this way, was tested. By imaging spin spirals on the Fe double layer on Ir(111), the tip's sensitivity to magnetic contrast was proven. The presence of an Fe cluster, which would

also cause sensitivity to magnetic contrast, was excluded by inverting the external magnetic field from 2 T to -2 T. As expected for a chromium tip, the contrast was not inverted along with the external field.

To assess the feasibility of applying high current densities with two contacting tips locally, simulations based on the finite element method were done, utilizing the software COMSOL Multiphysics®. Furthermore, two lateral current experiments on different substrates were conducted.
When applying lateral current to the layered transition metal dichalcogenide $NbSe_2$ starting at 20 K the charge density wave that can be observed below 34 K on the substrate is vanishing with increasing total lateral current. While the atomic lattice of $NbSe_2$ can be imaged well at higher lateral currents, thermal drifting and a current-dependent tip retraction in z-direction were observed. This may be caused by Joule heating, resulting in a temperature increase above the critical value of 34 K and an expansion of the sample.
The experiment was repeated on an Ir(111) single crystal, measuring tip retraction in the centre tip's z-signal. In contrast to the experiment on $NbSe_2$, only a very small expansion is observable. This indicates a tolerable increase in temperature for the planned experiments. For the z-signal, a more complex behaviour can be observed than what is expected for a simple expansion of the sample due to heating. In more spatially confined tip configurations with ultra-sharp tips, even less net heat deposition can be expected.
The simulations were focused on the determining geometric parameters for current density magnitude and distribution, the interaction of lateral current with an external magnetic field in z-direction, and the effect of Joule heating caused by the lateral current. To this end, an iridium sample and two tungsten contacting tips were modelled.
The simulations showed that the tip radii, the tip-to-tip distance, and the sample thickness are determining geometric parameters for the amount of current density in the centre between the contacting tips. For a sample thickness t smaller than the tip-to-tip distance, the relation $J_C \propto t^{-1}$ was shown, which is in agreement with a point contact approximation.
In the presence of external magnetic fields in z-direction, the lateral current is forced into spiralling paths on the sample surface. The Hall effect is forcing the charge carriers, which are radially spreading from the contact sites, onto spiralling paths. Through this interaction, the current direction in the centre between the contact sites is tilted, which has to be considered for the interpretation of experimental results, and the current density is decreasing slower with increasing distance to the contacting tips. However, the tilt can be corrected by rotating the side tips around the centre.

The simulation of heat deposition by Joule heating showed that the increase in temperature in equilibrium in the centre between the contacting tips is not expected to exceed an increase of about 10 K when a total current of up to 180 mA is applied. In addition, it can be assumed that merely a total current of 20 μA is needed to apply surface current densities above the threshold of $10^{10} \frac{\mathrm{A}}{\mathrm{m}^2}$, which is the predicted threshold to induce motion in nano-scale skyrmions. Therefore, it can be concluded that the application of high-density surface currents without harming effects of Joule heating is feasible. Furthermore, it was shown that the increase in temperature is dependent on the residual resistance ratio of the conducting metals. This leads to the conclusion that contact tips made of elemental metals are favourable. The simulations prove to be a useful tool in assessing the potential boundaries of lateral current experiments and helping in interpreting the results. However, their precision is limited to the assumptions made for the geometric models and the grade of discretization into finite elements.
In conclusion, the MP-STM is ready for more advanced experiments and shows great potential for three-tip applications.

Outlook

To enhance the understanding of surface current applications, the numerical modelling may be refined and expanded. This can be particularly valuable for the interpretation and assessment of future three-tip experiments involving surface currents. Further test measurements, including the application of surface currents with ultra-sharp tips in close proximity, especially in the presence of an external magnetic field, will support the findings of numerical modelling.

Installed into the UHV chamber system described in chapter 2, the MP-STM can now be used for the three-tip experiments on carbon nanotubes and atomic-scale skyrmions on Pd/Fe/Ir(111). It is capable of three-tip measurements with the tunnelling tips in overlapping scan ranges and of transmitting high-frequency signals to the tunnelling junctions of each, as was shown in previous works [42, 19].

There are many possible applications for the MP-STM. Of particular interest is the continuation of the study of atomic-scale skyrmions stabilised by the Dzyaloshinskii-Moriya interaction at the interface of Ir(111)-based thin film systems, which were previously intensely studied in the group [1, 2, 3, 4, 5, 6]. By utilising the side probes as contacts, the effect of lateral currents on individual skyrmions will be studied in real-space and in the time domain. By combining SP-STM and the three-tip configuration, spin- and time-resolved spectroscopy, magnetic imaging, tunnelling potentiometry, electron spin resonance spectroscopy, and pump-probe schemes can be utilised for this purpose.

The first experiments on atomic-scale skyrmions will be conducted on the bilayer system Pd/Fe on Ir(111), building upon the studies of [2]. The induction of motion on atomic-scale skyrmions will be tested by applying spin-polarised surface currents to large Pd/Fe terraces. These tests will be done at varying external magnetic fields and at temperatures ranging from 1.5 K to 100 K to understand the relations between skyrmion motion and these parameters. Multiple questions will be addressed regarding the influence of pinning centres, such as defects and impurities, and of the skyrmion Hall effect on the skyrmion's motion, as well as the interaction of skyrmions with the Pd/Fe bilayer's edges. It will commence with the

application of constant currents and imaging the skyrmions on the Pd/Fe bilayer with the third scanning unit. The study will then advance to the application of pulsed surface currents while detecting the passing of skyrmions with telegraph signals, and later to the application of pump and probe schemes.

Another key interest is the study of carbon nanotube based circuitry and hybrid DNA-nanostructures. The exploration will be initiated with the electrical characterization of nanotubes by contacting them with ultra-sharp tips in a three-tip configuration. This effort aligns with the group's pivotal role in a joint venture project focused on developing carbon nano-tube-based circuits, including logic gates and field-effect transistors. The utilisation of the MP-STM will culminate in the testing and characterising of these devices.

Experiments planned for this endeavour are starting with the contacting of one or multiple carbon nanotubes with two tips and scanning them with the third. Thereby, I-V curves shall be measured, and the tuning of the tube's electrical properties shall be tested. Hybrid DNA nanostructures and carbon nanotube circuitry will be received from collaborating colleagues. They will be imaged to identify their exact structure, and subsequently, they will be electrically characterised and tested by using the three tips as electrical contacts.

Reference List

[1] J. Friedlein et al. “A radio-frequency spin-polarized scanning tunneling microscope”. In: *Review of Scientific Instruments* 90.12 (Dec. 2019). ISSN: 1089-7623. DOI: 10.1063/1.5104317.

[2] P. Lindner et al. “Temperature and magnetic field dependent behavior of atomic-scale skyrmions in Pd/Fe/Ir(111) nanoislands”. In: *Physical Review B* 101.21 (June 2020), p. 214445. ISSN: 2469-9969. DOI: 10.1103/PhysRevB.101.214445.

[3] Kirsten von Bergmann et al. “Interface-induced chiral domain walls, spin spirals and skyrmions revealed by spin-polarized scanning tunneling microscopy”. In: *Journal of Physics: Condensed Matter* 26.39 (Sept. 2014), p. 394002. ISSN: 1361-648X. DOI: 10.1088/0953-8984/26/39/394002.

[4] Jonas Spethmann et al. “Zero-field skyrmionic states and in-field edge-skyrmions induced by boundary tuning”. In: *Communications Physics* 5.1 (Jan. 2022). ISSN: 2399-3650. DOI: 10.1038/s42005-021-00796-w.

[5] Stefan Heinze et al. “Spontaneous atomic-scale magnetic skyrmion lattice in two dimensions”. In: *Nature Physics* 7.9 (July 2011), pp. 713–718. ISSN: 1745-2481. DOI: 10.1038/NPHYS2045.

[6] Anika Schlenhoff et al. “Magnetic Nano-skyrmion Lattice Observed in a Si-Wafer-Based Multilayer System”. In: *ACS Nano* 9.6 (May 2015), pp. 5908–5912. ISSN: 1936-086X. DOI: 10.1021/acsnano.5b01146.

[7] Stuart S. P. Parkin, Masamitsu Hayashi and Luc Thomas. “Magnetic Domain-Wall Racetrack Memory”. In: *Science* 320.5873 (Apr. 2008), pp. 190–194. ISSN: 1095-9203. DOI: 10.1126/science.1145799.

[8] Masamitsu Hayashi et al. “Current-Controlled Magnetic Domain-Wall Nanowire Shift Register”. In: *Science* 320.5873 (Apr. 2008), pp. 209–211. ISSN: 1095-9203. DOI: 10.1126/science.1154587.

[9] Seonghoon Woo et al. “Observation of room-temperature magnetic skyrmions and their current-driven dynamics in ultrathin metallic ferromagnets”. In: *Nature Materials* 15.5 (Feb. 2016), pp. 501–506. ISSN: 1476-4660. DOI: 10.1038/NMAT4593.

[10] A. Hrabec et al. “Current-induced skyrmion generation and dynamics in symmetric bilayers”. In: *Nature Communications* 8.1 (June 2017). ISSN: 2041-1723. DOI: 10.1038/ncomms15765.

[11] Roméo Juge et al. “Current-Driven Skyrmion Dynamics and Drive-Dependent Skyrmion Hall Effect in an Ultrathin Film”. In: *Physical Review Applied* 12.4 (Oct. 2019), p. 044007. ISSN: 2331-7019. DOI: 10.1103/PhysRevApplied.12.044007.

[12] M. Stier et al. “Role of impurity clusters for the current-driven motion of magnetic skyrmions”. In: *Physical Review B* 103.5 (Feb. 2021), p. 054420. ISSN: 2469-9969. DOI: 10.1103/PhysRevB.103.054420.

[13] J. Bardeen. “Tunnelling from a Many-Particle Point of View”. In: *Physical Review Letters* 6.2 (Jan. 1961), pp. 57–59. ISSN: 0031-9007. DOI: 10.1103/PhysRevLett.6.57.

[14] J. Tersoff and D. R. Hamann. “Theory and Application for the Scanning Tunneling Microscope”. In: *Physical Review Letters* 50.25 (June 1983), pp. 1998–2001. ISSN: 0031-9007. DOI: 10.1103/PhysRevLett.50.1998.

[15] R. Wiesendanger. *Scanning probe microscopy and spectroscopy. methods and applications*. Cambridge University Press, 1994, p. 637. ISBN: 0521418100.

[16] M. Julliere. “Tunneling between ferromagnetic films”. In: *Physics Letters A* 54.3 (Sept. 1975), pp. 225–226. ISSN: 0375-9601. DOI: 10.1016/0375-9601(75)90174-7.

[17] J. C. Slonczewski. “Conductance and exchange coupling of two ferromagnets separated by a tunneling barrier”. In: *Physical Review B* 39.10 (Apr. 1989), pp. 6995–7002. ISSN: 0163-1829. DOI: 10.1103/PhysRevB.39.6995.

[18] R. Wiesendanger et al. “Observation of vacuum tunneling of spin-polarized electrons with the scanning tunneling microscope”. In: *Physical Review Letters* 65.2 (July 1990), pp. 247–250. ISSN: 0031-9007. DOI: 10.1103/PhysRevLett.65.247.

[19] Johannes Michael Friedlein. “A radio frequency-spin-polarized-scanning tunneling microscope for spin dynamics experiments”. PhD thesis. Universität Hamburg, 2018.

[20] Jonas Ove Harm. “Entwicklung und Aufbau einer Tieftemperatur-Ultrahochvakuumanlage für spinaufgelöste Mehrfach-Spitzen-Rastertunnermikroskopie mit hoher Zeitauflösung”. PhD thesis. Universität Hamburg, 2019.

[21] Philipp Lindner. "Thermal properties of atomic-scale skyrmions in PdFe nanoislands on Ir(111) investigated by variable-temperature and time-resolved scanning tunneling microscopy and spectroscopy". PhD thesis. Universität Hamburg, 2020.

[22] Yiming Zhang, Julian R. G. Evans and Shoufeng Yang. "Corrected Values for Boiling Points and Enthalpies of Vaporization of Elements in Handbooks". In: *J. Chem. Eng. Data* 56.2 (Jan. 2011), pp. 328–337. ISSN: 1520-5134. DOI: 10.1021/je1011086.

[23] Sven Lennart Tunze. *Präparation und Charakterisierung von ultra-scharfen Spitzen für SP-STM*. Bachelorthesis. 2014.

[24] André Engel. "Präparation und Charakterisierung von Chrom-Vollspitzen für die spin-polarisierte Rastertunnelmikroskopie". Diplomarbeit. Universität Hamburg, 2011.

[25] R. Wiesendanger et al. "Observation of vacuum tunneling of spin-polarized electrons with the scanning tunneling microscope". In: *Physical Review Letters* 65.2 (July 1990), pp. 247–250. ISSN: 0031-9007. DOI: 10.1103/PhysRevLett.65.247.

[26] Christian Hanneken et al. "Electrical detection of magnetic skyrmions by tunnelling non-collinear magnetoresistance". In: *Nature Nanotechnology* 10.12 (Oct. 2015), pp. 1039–1042. ISSN: 1748-3395. DOI: 10.1038/NNANO.2015.218.

[27] C. Gould et al. "Tunneling Anisotropic Magnetoresistance: A Spin-Valve-Like Tunnel Magnetoresistance Using a Single Magnetic Layer". In: *Physical Review Letters* 93.11 (Sept. 2004), p. 117203. ISSN: 1079-7114. DOI: 10.1103/PhysRevLett.93.117203.

[28] Wolfgang Demtröder. *Experimentalphysik 2*. Springer Berlin Heidelberg, 2017. ISBN: 9783662557907. DOI: 10.1007/978-3-662-55790-7.

[29] *EPO-TEK® EJ2189 Technical Data Sheet*. Epoxy Technology INC. 14 Fortune Drive, Billerica, MA.

[30] PI ceramics GmbH. *Piezokeramische Materialien und Bauelemente*. Physik Instrumente GmbH and Co. KG. Lindenstrasse, 07589 Lederhose, 2014. URL: https://www.PI.de, 19.05.23.

[31] G. Binnig and D. P. E. Smith. "Single-tube three-dimensional scanner for scanning tunneling microscopy". In: *Review of Scientific Instruments* 57.8 (Aug. 1986), pp. 1688–1689. ISSN: 1089-7623. DOI: 10.1063/1.1139196.

[32] C. Julian Chen. "Electromechanical deflections of piezoelectric tubes with quartered electrodes". In: *Applied Physics Letters* 60.1 (Jan. 1992), pp. 132–134. ISSN: 1077-3118. DOI: 10.1063/1.107348.

[33] *EPO-TEK® H77 Technical Data Sheet*. Epoxy Technology INC. 14 Fortune Drive, Billerica, MA.

[34] G. Nunes and Dinsie Williams. "Thermal contraction of ultrahigh vacuum materials for scanning probe microscopy from 300 to 4 K". In: *Journal of Vacuum Science* 13.3 (May 1995), pp. 1063–1065. ISSN: 1520-8567. DOI: 10.1116/1.587905.

[35] *Low Loss Microwave Coax, 24 AWG*. 086SC-2401. Molex LLC. Lisle, IL 60532, USA.

[36] M. Locatelli et al. "Easy method to characterize a piezoelectric ceramic tube as a displacer". In: *Review of Scientific Instruments* 59.4 (Apr. 1988), pp. 661–663. ISSN: 0034-6748. DOI: 10.1063/1.1139804.

[37] M. Hannss, W. Naumann and R. Anton. "Performance of a tilt-compensating tube scanner in atomic force microscopy". In: *Scanning* 20.7 (Oct. 1998), pp. 501–507. ISSN: 1932-8745. DOI: 10.1002/sca.1998.4950200703.

[38] Carsten Oldorf. "Aufbau eines Rastersondenmikroskopes für Rastertunnelmikroskopie und tunnelstabilisierte Magnetkraftmikroskopie". Diplomarbeit. Universität Hamburg, 1994.

[39] Yongfeng Wang, Yingchun Ye and Kai Wu. "Simultaneous observation of the triangular and honeycomb structures on highly oriented pyrolytic graphite at room temperature: An STM study". In: *Surface Science* 600.3 (Feb. 2006), pp. 729–734. ISSN: 0039-6028. DOI: 10.1016/j.susc.2005.12.001.

[40] Shuheng Pan. "Piezo-Electric Motor". English. European pat. WO9319494A1. 1993.

[41] *EPO-TEK® H20E Technical Data Sheet*. Epoxy Technology INC. 14 Fortune Drive, Billerica, MA.

[42] Jonas Koch. "Aufbau und Charakterisierung eines Mehrspitzen-Rastertunnelmikroskops für Hochfrequenzmessungen". Masterthesis. University of Hamburg, 2019.

[43] Jean-Pierre Pascault and Roberto J. J. Williams. *Epoxy Polymers: New Materials and Innovations. new materials and innovations*. Wiley, Jan. 2010, p. 367. ISBN: 9783527628704. DOI: 10.1002/9783527628704.

[44] Patrick Ewerhardt. *Aufbau und Optimierung eines Drei-Spitzen-Rastertunnel-Mikroskops*. Bachelorthesis. 2019.

[45] *Temperature probe selection guide*. Lake Shore Cryotronics, Inc. 550 Tressler Dr. Westerville, OH 43082-8888.

[46] Deutsches Kupferinstitut Auskunfts und Beratungsstelle. *Kupfer-Zinn-Knetlegierungen (Zinnbronzen)*. Tech. rep. 7. Am Bonneshof 5, 40474 Düsseldorf: Deutsches Kupferinstitut, 2004.

[47] Deutsches Kupferinstitut Auskunfts und Beratungsstelle. *Materialinformation Cu-OFE*. Tech. rep. Am Bonneshof 5, 40474 Düsseldorf: Deutsches Kupferinstitut, 2005.

[48] Peter Kurzweil, Bernhard Frenzel and Florian Gebhard. *Physik Formelsammlung : Mit Erläuterungen und Beispielen aus der Praxis für Ingenieure und Naturwissenschaftler. Mit Erläuterungen und Beispielen aus der Praxis für Ingenieure und Naturwissenschaftler*. Vol. 4. Springer Vieweg, 2014, p. 446. ISBN: 9783658191894.

[49] Bert Voigtländer et al. "Invited Review Article: Multi-tip scanning tunneling microscopy: Experimental techniques and data analysis". In: *Review of Scientific Instruments* 89.10 (Oct. 2018). ISSN: 1089-7623. DOI: 10.1063/1.5042346.

[50] Tomonobu Nakayama et al. "Development and Application of Multiple-Probe Scanning Probe Microscopes". In: *Advanced Materials* 24.13 (Feb. 2012), pp. 1675–1692. ISSN: 1521-4095. DOI: 10.1002/adma.201200257.

[51] Arthur Leis et al. "Nanoscale tip positioning with a multi-tip scanning tunneling microscope using topography images". In: *Review of Scientific Instruments* 93.1 (Jan. 2022). ISSN: 1089-7623. DOI: 10.1063/5.0073059.

[52] An-Ping Li et al. "Electron Transport at the Nanometer-Scale Spatially Revealed by Four-Probe Scanning Tunneling Microscopy". In: *Advanced Functional Materials* 23.20 (Mar. 2013), pp. 2509–2524. ISSN: 1616-3028. DOI: 10.1002/adfm.201203423.

[53] Vasily Cherepanov et al. "Ultra compact multitip scanning tunneling microscope with a diameter of 50 mm". In: *Review of Scientific Instruments* 83.3 (Mar. 2012). ISSN: 1089-7623. DOI: 10.1063/1.3694990.

[54] Jong-Kwon Lee et al. "Modification of Electrical Properties of Graphene by Substrate-Induced Nanomodulation". In: *Nano Letters* 13.8 (2013), pp. 3494–3500. ISSN: 1530-6992. DOI: 10.1021/nl400827p.

[55] R.F. Egerton, P. Li and M. Malac. "Radiation damage in the TEM and SEM". In: *Micron* 35.6 (Aug. 2004), pp. 399–409. ISSN: 0968-4328. DOI: 10.1016/j.micron.2004.02.003.

[56] *Long Distance Microscope Product Manual*. LaVision GmbH. Anna-Vandenhoeck-Ring 19. D-37081 Göttingen, June 2021.

[57] Albert G. Ingalls. *Amateur telescope making*. Vol. 3. Willmann-Bell, 1996. ISBN: 0943396484.

[58] *Fiber-Coupled LED, 470 nm.* MTN032498-S01, Rev A. Thorlabs, Inc. 43 Sparta Ave-Newton, New Jersey 07860 United States, Nov. 2022.

[59] David Tománek et al. "Theory and observation of highly asymmetric atomic structure in scanning-tunneling-microscopy images of graphite". In: *Physical Review B* 35.14 (May 1987), pp. 7790–7793. ISSN: 0163-1829. DOI: 10.1103/PhysRevB.35.7790.

[60] J. V. Barth et al. "Scanning tunneling microscopy observations on the reconstructed Au(111) surface: Atomic structure, long-range superstructure, rotational domains, and surface defects". In: *Physical Review B* 42.15 (Nov. 1990), pp. 9307–9318. ISSN: 1095-3795. DOI: 10.1103/PhysRevB.42.9307.

[61] *Ultra Sharp NanoProbe.* Nauga Needles LLC. visited on Oct. 25th 2023, 9 am. URL: https://nauganeedles.com/product/nn-usnp/.

[62] *Price list for 99.95% tungsten wire (diameter 0.25mm).* Goodfellow Cambridge Limited - UK. visited on Oct. 25th 2023 9am. URL: https://www.goodfellow.com/p/w-00-wr-000150/tungsten-wire.

[63] *Price list for 99.95% tungsten wire (diameter 0.25mm).* Thermo Fisher Scientific Inc. visited on Oct. 25th 2023 9am. URL: https://www.fishersci.com/us/en/browse/80014045/transition-metals.

[64] *Price list for 99.95% tungsten wire (diameter 0.25mm).* Midwest Tungsten Service. visited on Oct. 25th 2023 9am. URL: https://shop.tungsten.com/pure-tungsten/.

[65] J. P. Ibe et al. "On the electrochemical etching of tips for scanning tunneling microscopy". In: *Journal of Vacuum Science and Technology A* 8.4 (July 1990), pp. 3570–3575. ISSN: 1520-8559. DOI: 10.1116/1.576509.

[66] Wei-Tse Chang et al. "Method of electrochemical etching of tungsten tips with controllable profiles". In: *Review of Scientific Instruments* 83.8 (Aug. 2012). ISSN: 1089-7623. DOI: 10.1063/1.4745394.

[67] Yasser Khan et al. "Two-step controllable electrochemical etching of tungsten scanning probe microscopy tips". In: *Review of Scientific Instruments* 83.6 (June 2012). ISSN: 1089-7623. DOI: 10.1063/1.4730045.

[68] R. Wiesendanger et al. "Recent advances in scanning tunneling microscopy involving magnetic probes and samples". In: *Applied Physics A Solids and Surfaces* 53.5 (Nov. 1991), pp. 349–355. ISSN: 1432-0630. DOI: 10.1007/BF00348147.

[69] A. Schlenhoff et al. “Bulk Cr tips with full spatial magnetic sensitivity for spin-polarized scanning tunneling microscopy”. In: *Applied Physics Letters* 97.8 (Aug. 2010). ISSN: 1077-3118. DOI: 10.1063/1.3474659.

[70] Kirsten von Bergmann et al. “Complex magnetism of the Fe monolayer on Ir(111)”. In: *New Jounal of Physics* 9.10 (Oct. 2007), pp. 396–396. ISSN: 1367-2630. DOI: 10.1088/1367-2630/9/10/396.

[71] Pin-Jui Hsu et al. “Guiding Spin Spirals by Local Uniaxial Strain Relief”. In: *Physical Review Letters* 116.1 (Jan. 2016), p. 017201. ISSN: 1079-7114. DOI: 10.1103/physrevlett.116.017201.

[72] Aurore Finco. “Interplay between non-collinear magnetism and nanoscale structural properties in epitaxial Fe-based ultrathin films”. PhD thesis. Universität Hamburg, 2018.

[73] D.L. Peng et al. “Magnetic properties of Fe clusters adhering to single-wall carbon nanotubes”. In: *Journal of Magnetism and Magnetic Materials* 292 (Apr. 2005), pp. 143–149. ISSN: 0304-8853. DOI: 10.1016/j.jmmm.2004.10.106.

[74] Felix Bischoff et al. “Nanoscale Phase Engineering of Niobium Diselenide”. In: *Chemistry of Materials* 29.23 (Nov. 2017), pp. 9907–9914. ISSN: 1520-5002. DOI: 10.1021/acs.chemmater.7b03061.

[75] *Data retriThe Materials Project for NbSe2 (mp-10228) from database version v2023.11.1.* The Materials Project. visited on Jan. 30th, 19 pm. URL: https://next-gen.materialsproject.org/materials/mp-10228?formula=NbSe2.

[76] Cody Friesen. “Magneto-Seebeck tunneling across a vacuum barrier”. PhD thesis. Universität Hamburg, 2019.

[77] Richard Courant. “Courant, Richard. ”Variational methods for the solution of problems of equilibrium and vibrations”. In: *Bulletin of the American Mathematical Society* (1943), pp. 1–23.

[78] Marcus Wagner. *Lineare und Nichtlineare FEM Eine Einführung Mit Anwendungen in der Umformsimulation Mit LS-DYNA®. Eine Einführung Mit Anwendungen in der Umformsimulation Mit LS-DYNA®*. Springer Fachmedien Wiesbaden GmbH, 2022. ISBN: 9783658365219.

[79] Dorothee Herrmann. “Probenpräparation und Querstromsimulationen für spinaufgelöste Transportmessungen mit einem Mehrspitzen-Rastertunnelmikroskop”. Bachelorthesis. Universität Hamburg, 2021.

[80] Stephen Blundell. *Magnetism in Condensed Matter (Oxford Maser Series in Condensed Matter Physics)*. Oxford University Press, USA, 2001, p. 256. ISBN: 978-0-19-850591-4.

[81] Rudolf Gross. *Festkörperphysik*. De Gruyter, 2014, p. 1006. ISBN: 9783110358698.

[82] Conor J. McCluskey et al. "Ultrahigh Carrier Mobilities in Ferroelectric Domain Wall Corbino Cones at Room Temperature". In: *Advanced Materials* 34.32 (July 2022). ISSN: 1521-4095. DOI: 10.1002/adma.202204298.

[83] Neil W. Ashcroft and David N. Mermin. *Festkörperphysik*. de Gruyter GmbH, Walter, 2012. ISBN: 978-3-486-71301-5.

[84] Cho Yen Ho R. W. Powell and Peter Edward Liley. *Thermal Conductivity of Selected Materials*. Tech. rep. Vol. 8. USA: National Bureau of Standards (NBS), 1966.

[85] L. J. Ericks G. E. Childs and R. L. Powell. *Thermal Conductivity of Solids At Room Temperature and Below*. Tech. rep. USA: NBS, 1973.

[86] J. G. Hust and L. L. Sparks. *Lorenz Ratios of Technically Important Metals and Alloys*. Tech. rep. USA: NBS, 1973.

[87] F. R. Fickett. *Electrical Properties of Materials and Their Measurement at Low Temperatures*. Tech. rep. USA: NBS, 1982.

[88] J. G. Hust and A. B. Lankford. *Thermal conductivity of aluminium, copper, iron, and tungsten for temperatures from 1 K to the melting point*. Tech. rep. USA: NBS, 1984.

[89] Y. S. Touloukian and T. Makita. *Thermophysical Properties of Matter*. Tech. rep. USA: Defense Logistic Agency, 1970.

[90] G. K. White and S. B. Woods. "Thermal and electrical conductivity of rhodium, iridium, and platinum". In: *Canadian Journal of Physics* 35.3 (Mar. 1957), pp. 248–257. ISSN: 1208-6045. DOI: 10.1139/p57-029.

[91] G. K. White and S. B. Woods. "Electrical and thermal resistivity of the transition elements at low temperatures". In: *Philosophical Transactions of the Royal Society of London. Series A, Mathematical and Physical Sciences* 251.995 (Mar. 1959), pp. 273–302. ISSN: 2054-0272. DOI: 10.1098/rsta.1959.0004.

Danksagung / Acknowledgements

Hiermit möchte ich insbesondere danken:

Prof. Dr. Roland Wiesendanger für die Betreuung meiner Promotion, die Übernahme des Erstgutachtens, und für die Gelegenheit seit 2018 in seiner Forschungsgruppe arbeiten, forschen, und lernen zu dürfen.

Prof. Dr. Philip Moll für die Übernahme des Zweitgutachtens.

Dr. Stefan Krause für die kontinuierliche Betreuung seit 2018, für kritische, hilfreiche, und immer freundliche Diskussionen, sowie die angenehme kollegiale Atmosphäre.

Dr. Philipp Lindner für die angenehme und konstruktive Zusammenarbeit im Labor.

Dorothee Herrmann, Raluca Boltje, Dr. Hermann Osterhage, und Patrick Ewerhardt für ihre Unterstützung, ebenso wie alle anderen Mitglieder unserer Forschungsgruppe.

Den Teams der Feinmechanikwerkstatt, der ehemaligen Elektronikwerkstatt, und der Heliumversorgung danke ich für die zuverlässige Zusammenarbeit und ihren unermüdlichen Einsatz.
Ich danke Marian, Bernd und Bosse für die Unterstützung während des Schreibens dieser Arbeit.
Abschließend möchte ich ganz herzlich meiner Verlobten Ann-Katrin, meiner Familie, und meinen Freunden für ihre Unterstützung während meines Studiums, ihre Geduld mit mir, und ihren Glauben in meine Fähigkeiten danken.

Eidesstattliche Versicherung / Declaration on oath

Hiermit versichere ich an Eides statt, die vorliegende Dissertationsschrift selbst verfasst und keine anderen als die angegebenen Hilfsmittel und Quellen benutzt zu haben.

Sofern im Zuge der Erstellung der vorliegenden Dissertationsschrift generative Künstliche Intelligenz (gKI) basierte elektronische Hilfsmittel verwendet wurden, versichere ich, dass meine eigene Leistung im Vordergrund stand und dass eine vollständige Dokumentation aller verwendeten Hilfsmittel gemäß der Guten wissenschaftlichen Praxis vorliegt. Ich trage die Verantwortung für eventuell durch die gKI generierte fehlerhafte oder verzerrte Inhalte, fehlerhafte Referenzen, Verstöße gegen das Datenschutz- und Urheberrecht oder Plagiate.

Hamburg, den 17.04.2024

Unterschrift des Doktoranden